

Characterization of an Electroactive polymer actuator in diaphragm micropump

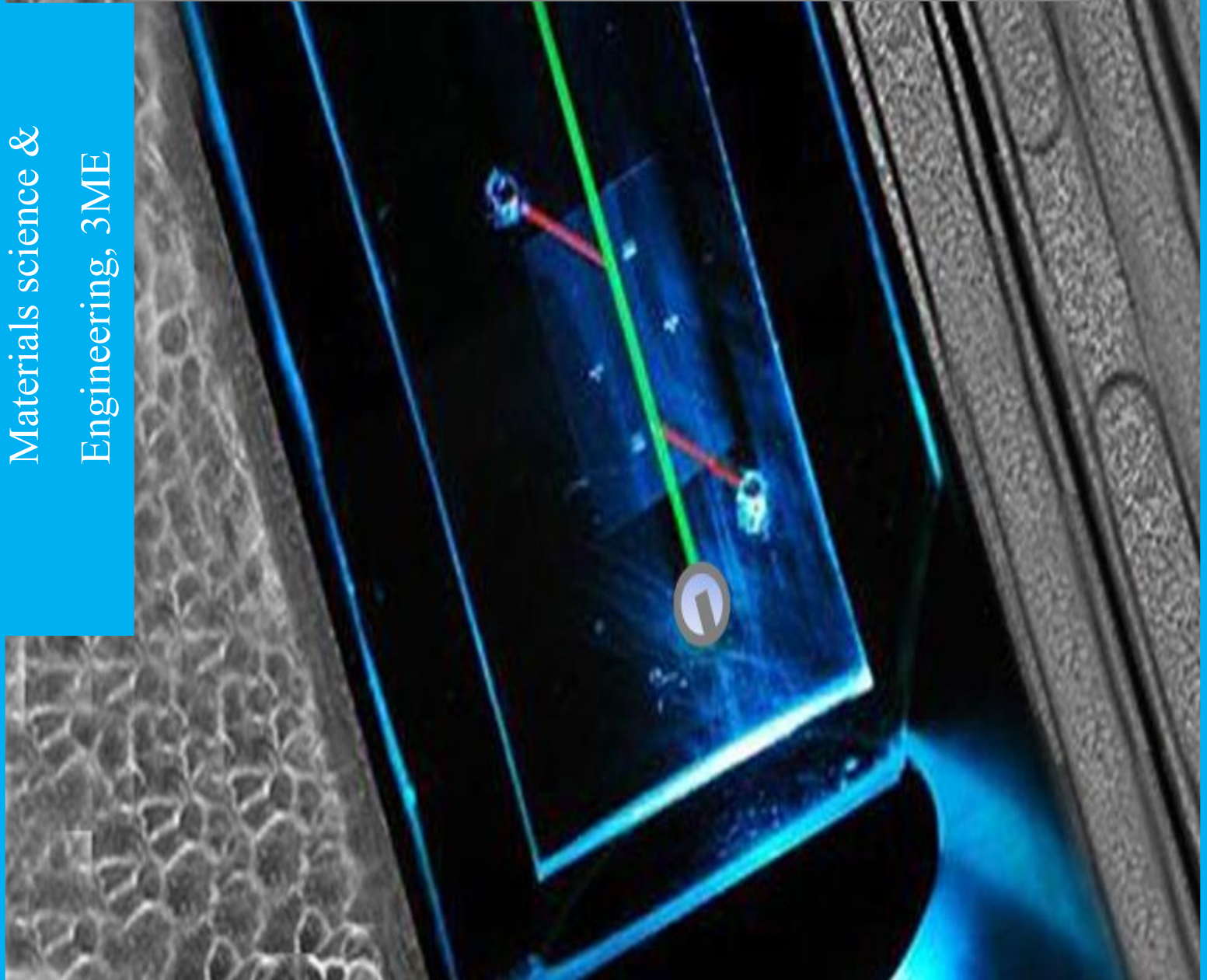
for Organ-on-Chip application

Master thesis

Sudiksh Srivastava

4918460

Materials science &
Engineering, 3ME



Characterization of an Electroactive polymer actuator in diaphragm micropump for OoC application

by

Sudiksh Srivastava

to obtain the degree of Masters of Science
in Materials science and Engineering
at the Delft University of Technology, Netherlands
to be defended publicly on
November 29, 2021 at 12:00 PM.

Student number: 4918460
Project duration : August, 2020 - November, 2021
Daily supervisor : Paul Motreuil-Ragot, PhD, ECTM, TU Delft
Thesis advisor : Dr. Massimo Mastrangeli
Thesis committee : Dr. Massimo Mastrangeli, TU Delft, EWI faculty
Dr. Miguel A. Bessa (co-advisor), TU Delft, 3ME faculty
Dr. Andres Hunt, TU Delft, 3ME faculty

An electronic version of this thesis is available at:
<http://repository.tudelft.nl/>.

*Cover picture: Levitt, A. S. (2008, May 21). Lung-on-a-Chip. TFOT.
<https://thefutureofthings.com/5997-lung-on-a-chip>.*



Abstract

The existing drug development process is economically and scientifically challenging. It fails to efficiently emulate human physiology in-vitro with the current pre-clinical studies which includes in-vitro cell culture models and animal testing. Organ-on-Chip (OoC) technology aims to recreate an in-vivo like micro environment to investigate drug response more effectively. There are ongoing attempts to fabricate OoC technology as a single-platform micro-device to minimize its reliance on external components. In this perspective, the functionality and throughput of this technology can be improved. One such novel approach is addition of an ionic electroactive polymer (iEAP) actuated diaphragm micropump.

The primary aim of this thesis project was to determine the suitable dimensions of a micro cantilever iEAP, specifically Ionic polymer metal composite (IPMC) to generate appropriate flow rate for the projected diaphragm micropump. In addition to that, dynamics of the IPMC cantilever actuator was examined in dry environment. To achieve this the actuator tip - force, tip-displacement and longevity tests were performed. The results at macroscopic scale were tentatively explained with molecular characteristics of the material.

As a result, it was shown that an IPMC cantilever actuator of millimetric size possesses viscoelastic properties and classical mechanical theories cannot be used to validate the experimental results. Secondly, the actuation results for 0.1 and 1 Hz align with the input driving frequency. The IPMC cantilever of length 7 mm generates the maximum tip-force of 0.138 mN and it is suggested to be used as a diaphragm actuator for the upcoming micropump.

Acknowledgement

I would like to express my deepest gratitude to my project supervisors, Dr. Massimo Mastrangeli and Paul Ragot. Their unwavering support, patience and encouragement have helped me immensely as I hurdled through the path of my Masters program. It has been a pleasure to work with them and a rewarding experience. I am grateful to have such understanding supervisors who have assisted me at every step and the completion of this thesis project would not have been possible without them. I have acquired an incredible amount about conducting proper research. I am obliged to my daily supervisor, Paul who was always available to guide and assist me, even if it included printing models for my experimental setup, helping me understand the basics of electrical engineering or with python coding. I wish him best of luck with the continuation of his PhD. I would like to further thank Dr. Miguel Bessa, a great lecturer and my co-advisor, who always available to help. I would like to further thank all the members of the ECTM group who have helped throughout this thesis project.

Finally, I would like to give my deep appreciation and love to my parents and family members. They have been my constant support system, motivated me and helped me in my pursuits. I am also thankful to my friends, both in Delft and different parts of the world.

Thank you everyone who has been a part of this eventful journey.

Contents

Abstract	v
Acknowledgement	vi
List of Figures	ix
List of Tables	xii
1 Introduction	1
2 Literature review & theory	3
2.1 Organ on Chip (OoC)	3
2.2 Micropump Technology	6
2.3 Micropump actuation mechanism	8
2.4 Valveless design and features	12
2.5 Electroactive polymers (EAPs)	18
2.5.1 Nafion characteristics	19
2.6 Ionic polymer metal composite - IPMC	21
3 Research Methodology	27
3.1 Density measurements and approximation	27
3.2 Tip-Force measurements	30
3.3 Displacement measurements	36
4 Results	40
4.1 IPMC Tip-force	40
4.2 IPMC Tip-displacement	56
4.3 IPMC density approximation	63
4.4 IPMC endurance test	64
5 Discussion	68
Conclusion	81
References	83
Appendix - I	91

Appendix - II	100
Appendix - III	103

List of Figures

1	Drug development process. [2]	3
2	Fundamental approach to fabricate OoC device by the group of Dr. Ingber. [4]	5
3	Schematic of a general mechanical micropump. [6]	7
4	Electromagnetic micropump by Yamahata et al. [8]	9
5	Electrostatic pump schematic.[13]	10
6	Piezoelectric micropump schematic. [16]	11
7	Nozzle/diffuser geometrical parameters. [66]	13
8	Cross section schematic of a Tesla valve. [18]	13
9	Pumping operation. [19]	14
10	Schematic of diffuser and nozzle. [19]	15
11	Schematic of conical and flat-walled diffuser geometry. [21] . .	16
12	Stability plot for diffuser geometries. [20]	17
13	Efficiency plot with respect to diffuser angle for various Re. [22]	17
14	(a) Efficiency versus curvature ratio for different θ at Re=100. (b) Efficiency versus diffuser length for different θ at Re=100. [22]	18
15	Nafion polymer structure. [31]	20
16	Flemion polymer structure. [69]	20
17	Schematic of the sulfonate clusters. [32]	21
18	Schematic of back relaxation phenomenon.	22
19	Schematic of back relaxation phenomenon.	23
20	Molecular and macroscopic behaviour of IPMC with Nafion. .	24
21	IPMC sample ($12 \times 12 \text{ cm}^2$) used for density measurement. . .	29
22	Archimedes experiment setup schematic.	29
23	Schematic of Tip-force characterization setup.	31
24	A closer look of the real setup. 1. Load cell surface, 2. Gold electrodes, 3. Fixing plate and 4. IPMC sample (9 mm). . . .	33
25	Illustration of the MATLAB designer UI for voltage application. 34	
26	An example of tip-force plot for 7mm IPMC, $4 V_{pp}$ at 1 Hz. .	34
27	10 second window of fig-26. Peaks and valleys represented as red and black crosses respectively.	35
28	An example of to explain peak tip-force & force span.	35
29	Schematic of tip-displacement measurement.	37
30	The initial tip-displacement experimental setup.	38

31	Example of a displacement data window obtained at 0.1 Hz with 10 mm laser sensor.	39
32	The second laser displacement sensor setup.	39
33	7 mm IPMC output force signal at 3.5 and 4 V_{pp}	40
34	9 mm IPMC output force signal.	42
35	11 mm IPMC output force signal.	42
36	IPMC samples (7, 9 & 11 mm) force span versus applied V_{pp} plots.	44
37	IPMC samples (7, 9 & 11 mm) peak tip-force versus applied V_{pp} plots.	45
38	Peak tip-force versus IPMC length.	46
39	7 mm IPMC force signal at 4V, 0.1 Hz. Left: Full signal. Right: 140 second window illustrating peak tip-force, force span and pulling force.	47
40	7 mm IPMC force signal at different voltages.	48
41	9 mm IPMC force signal at 4 V.	49
42	11 mm IPMC force signal at 4 V.	49
43	IPMC 7 mm force span versus applied V_{pp}	50
44	IPMC 7 mm peak Tip-force v/s V_{pp} plots.	50
45	Example of 7 mm IPMC force signal at 5Hz. Left: Full signal, Right: 150 seconds window.	51
46	7 mm IPMC force signal, 5 Hz at different V_{pp}	52
47	9 mm IPMC force signal at 4 V_{pp}	53
48	11 mm IPMC force signal at 4 V_{pp}	53
49	7 mm IPMC force span versus applied V_{pp}	54
50	IPMC 7 mm peak tip-force vs V_{pp} plot.	54
51	Example of the total tip-displacement calculation.	56
52	7 mm IPMC tip-deflection signal at different peak to peak voltages.	57
53	Side view of the bent 7mm IPMC sample after displacement measurements for 1200 seconds at 4 V_{pp}	58
54	IPMC 7 mm tip-force vs V_{pp} plot.	59
55	IPMC 7 mm tip-deflection signal at 0.1 Hz using optoNCTD 1750.	59
56	IPMC 9 mm tip-deflection signal at 0.1 Hz using optoNCTD 1750.	60
57	IPMC 11 mm tip-deflection signal at 0.1 Hz using optoNCTD 1750.	61

58	IPMC 7 mm tip-deflection at 5 Hz using optoNCTD 1750. . .	62
59	IPMC 9 mm tip-deflection at 5 Hz using optoNCTD 1750. . .	62
60	IPMC 11 mm tip-deflection at 5 Hz using optoNCTD 1750. . .	63
61	IPMC 7 mm endurance test.	65
62	IPMC 9 mm endurance test.	66
63	IPMC 11 mm endurance test.	66
64	IPMC 7 mm endurance test per 60 seconds.	67
65	7 mm IPMC windows between 20 - 30 seconds at 2 and 4 V between	69
66	Depiction of IPMC actuation corresponding to the applied peak to peak voltage (schematic of the GUI)	70
67	Correlation of acquired signal (top) to the input actuation signal schematic (bottom).	73
68	Comparison of 2 and 4 V force signal at 5 Hz for the 7 mm IPMC.	75
69	Setup for resonance frequency experiment.	77
70	Schematic of the first vibrational mode shape.	78
71	FFT analysis at 5 Hz for the 7 mm IPMC, $4V_{pp}$. Left: Full plot, Right: Zoomed in plot.	79
72	COMSOL model geometry.	102
73	Preliminary COMSOL deformation result.	103
74	Tip force and displacement correlation, 7 mm IPMC. Top row: Force signal, Bottom row: Displacement signal.	109
75	Tip force and displacement correlation, 9 mm IPMC. Top row: Force signal, Bottom row: Displacement signal.	110
76	Tip force and displacement correlation, 11 mm IPMC. Top row: Force signal, Bottom row: Displacement signal.	111

List of Tables

1	Brief summary of EAPs.	19
2	Few examples of IPMC dimensions used in the literature. . . .	26
3	Force span for <i>7 mm</i> IPMC at different applied voltages. . . .	41
4	Peak Tip-force for <i>7 mm</i> IPMC at different applied voltages.	41
5	Force span for <i>9 mm</i> IPMC at different applied voltages. . . .	43
6	Peak Tip-force for <i>9 mm</i> IPMC at different applied voltages. .	43
7	Force span for <i>11 mm</i> IPMC at different applied voltages. . .	43
8	Peak Tip-force for <i>11 mm</i> IPMC at different applied voltages.	44
9	Force span of the IPMC samples at 1 Hz.	45
10	Peak Tip-force generated by the 7mm IPMC at 1 Hz.	46
11	Force span results for the 7 mm IPMC at 0.1 Hz driving fre- quency.	49
12	Peak tip-force results for the 7 mm IPMC at 0.1 Hz driving frequency.	51
13	Force span results for the 7 mm IPMC at 5 Hz driving fre- quency.	53
14	Peak tip-force results for the 7 mm IPMC at 5 Hz driving frequency.	55
15	Total Tip-deflection results for the 7 mm IPMC at 1 Hz driving frequency.	58
16	Density values using Archimedes Principle experiment.	63
17	Data variation to reduce deviation using the reset procedure .	71

1 Introduction

Drug development is a long and extremely costly process with a low success rate. It can cost over \$3 billion and approximately 10 years to introduce a new and safe drug into the market.[36] Over the past few decades remarkable progress have been made to understand, manipulate and improve the effect of drugs and vaccines in in-vivo conditions. However, almost 30% of drugs fail during the pre-clinical trials due to toxicity and the other 60% fail because of undesired results. Overcoming this necessitates the rise of an alternative and more efficient technology capable of producing a superior outcome. Organ-on-Chip (OoC) is an emerging technology which attempts to closely mimic the tissue microenvironment in-vitro, so that under given circumstances in-vivo physiology of the tissues and organs can be reproduced in a short amount of time. This includes the drug response. One of the main uses of OoC devices is as drug discovery tool which may have the potential to replace a stage of conventional pre-clinical animal testing. A typical OoC comprises of a microfluidic chamber, living tissues, sensing system with a provision of electrical, optical, thermal or mechanical stimuli. [35]

Micropumps are miniature pumping systems which can be fabricated along microfluidic channels to initiate, control and deliver minute volume of fluid in a microfluidic device. They are a perfect replacement for the conventional and bulky pneumatic or peristaltic pumps. On-platform micropumps in a OoC device can reduce the testing time and cost drastically along with improving the accuracy of the test results and improve portability of this complex system. This active device in millimeter range can make OoC as a single platform technology. The micropumps are the heart of any microfluidic device which require power for moving the fluid. [37][38][39]

Displacement or reciprocating micropumps have been a topic of extensive research in many fields of science. They can be fabricated with wide range of actuation mechanisms depending on specific applications. Ionic electroactive polymers have come out as a promising diaphragm actuator when integrated with an elastic membrane (like PDMS) underneath it. These materials are capable of producing high displacement under low applied voltage and are ideal for biomedical applications due to low degradation rate.[44]

The focus of this thesis project involves material characterization of an electroactive polymer. Results procured from the characterization experiments will be utilized in microfabricating an efficient valveless diaphragm actuated micropump for OoC application. In this report, a brief introduction of Organ-on-Chip, micropump technology and its actuation mechanisms is provided. This is followed by a discussion on electroactive polymer with a focus on Ionic polymer metal composite (IPMC). The dominant part of IPMC, Nafion and its characteristic behaviour at molecular level is studied in-depth. The characteristics discussed will be used in explaining the results at macroscopic level. Thereafter, research methodology describing the experimental setups and processes is presented in Chapter-3. After establishing a concrete understanding, results of the experiments followed by its detailed discussion is presented in Chapter-4 and 5 respectively. The results include tip-force and tip-displacement measurements accompanied by density estimation using Archimedes principle and a longevity test on the IPMC samples for long-term measurement are performed. Lastly, the report is concluded with future work and challenges.

In addition to this content, few appendices can be found at the end of this report. In Appendix-I, Python code used for data analysis and post processing of the results is presented along with that of Fast Fourier transform. Appendix-II includes preliminary COMSOL simulations and the procured experimental results are used as an input for the existing COMSOL model. Additional post processed plots are given in Appendix-III.

2 Literature review & theory

2.1 Organ on Chip (OoC)

Healthcare systems all around the world are faced with a predominant challenge of providing safe and innovative treatments to the human population while trying to reduce the drug prices. A study shows that the main drivers of the drug costs are development time, cost of R&D projects and success rate. [1] Current pandemic is a timely example. Wyss Institute's OoC is used to recognize amodiaquine, an anti-malarial drug as an efficacious inhibitor of severe acute respiratory syndrome coronavirus-2 (SARS-CoV-2) infection. SARS-CoV-2 is the virus that causes contagious disease, COVID-19.[9] These costs differ depending on stages through which the drug pass.[2] A fundamental drug development process is presented in figure-1:

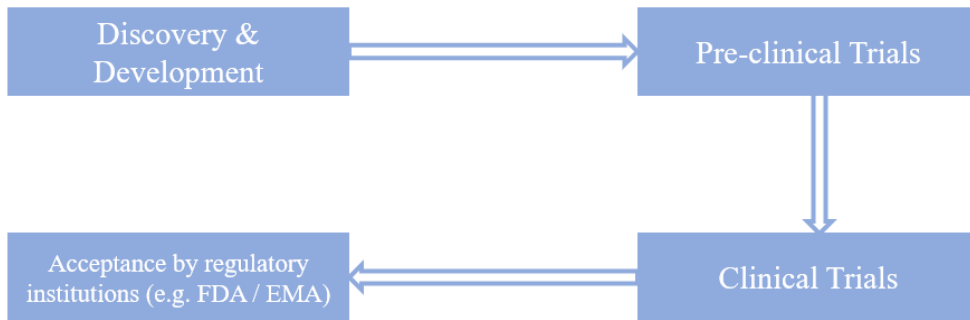


Figure 1: Drug development process. [2]

The whole process is extremely expensive and almost 60-75% of projects that succeed in the clinical trials regularly fail in Phase 2 and 20-30% fail in Phase 3. [11] To overcome this vital issue and improve human lifespan, Organ-on-Chip technology was introduced which has the potential to transform the whole pharmaceutical research and development sector. The field of microfluidics came into light with the introduction of an elastomer called poly(dimethylsiloxane) (PDMS), which is optically transparent (allows real-time monitoring), hydrophobic and non-toxic when cured, which are the ideal material properties in the field of biology. A distinct feature of this material

includes absorption of small hydrophobic molecules which affect the experimental results. [3]

OoC devices are micro engineered to constitute main features of the human tissues and organs along with their interaction using cell cultures. [3] Aim is to recapitulate minimal functional units rather than building a whole living organism. A simple setup includes a single perfused chamber with one kind of cell culture to demonstrate specific tissue functions whereas a complex design can include more than one kind of cultured cells on either side of a porous membrane to recreate the tissue interface. [4]

It was in 2010 when the group of Dr. Donald Ingber invented the first Organ on Chip by replicating the functions of the human lungs on a microfluidic chip.[9][16] Few advantages of microfluidic devices: they are relatively inexpensive, require small quantities of reagent and have short reaction times. [14] Figure - 2 illustrates the basic fabrication process to develop a microfluidic chip. At first the cavities are created in PDMS using photolithography and then micro fluidic channels are fabricated using the same process. Another micro fabrication technique named soft lithography can be used to achieve same results but with wide range of elastomeric materials. A mould (usually made of PDMS) is made using photo or e-beam lithography. This mould can then be used multiple times to develop a microfluidic device. These chips provide a complex mechanical microenvironment for the living cells. When the cells are made to adhere on a flexible membrane, they undergo fluid shear stress and cyclic mechanical deformation which is usually experienced by cells in a living organ during cardiovascular cycle, breathing and peristalsis. [4]

Although this rapidly growing technology has the potential to eliminate compromises attached to human/animal test which hinder the drug development process, there are remarkable engineering challenges associated with it. A brief list of challenges are as following: [5]

1. Determination of the organ size. Since the organs are scaled to micro or milli-meter range in an OoC it can be difficult to determine the scaling approach.
2. It can be difficult to couple two or more organs together and control and maintain the adequate fluid flow and perform drug analysis. It is also challenging to develop same culture medium for different organ types.

3. Factors like morphology, inter-cellular forces and signalling, extra-cellular electrolytes and much more have to be taken into account which can add extreme complexity to these devices in some conditions.

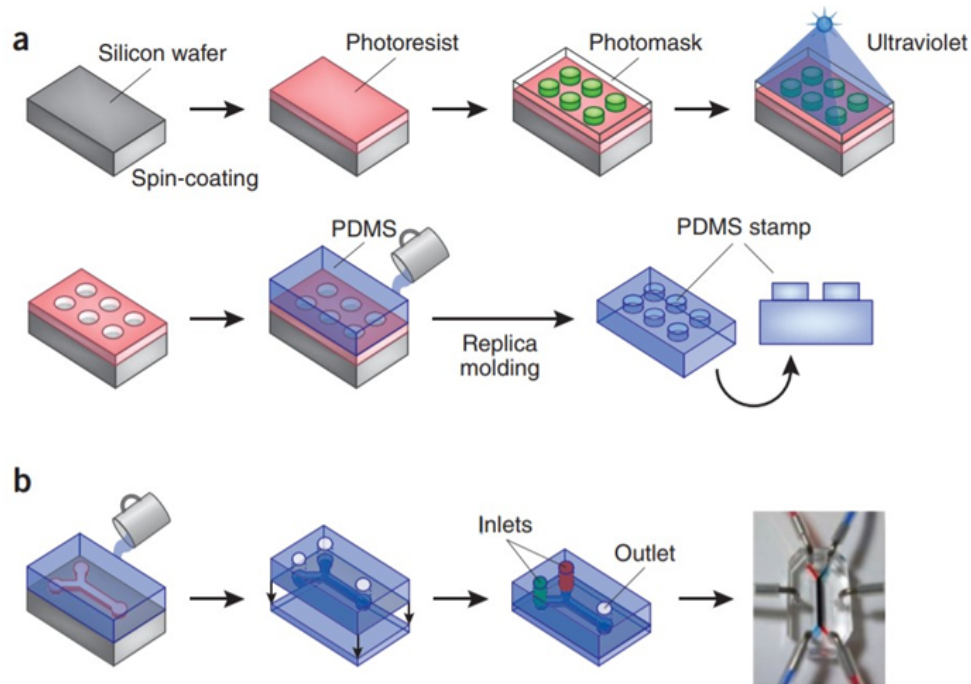


Figure 2: Fundamental approach to fabricate OoC device by the group of Dr. Ingber. [4]

The above mentioned are a few of many challenges which are encountered while fabricating and post processing an OoC device. Nevertheless, new advancements in this field of science promise the development of better and more efficient OoC devices in order to utilize this technology to its full potential. One crucial addition to these micro devices is the introduction of the micropumps which can replace the bulky pneumatic or peristaltic pumps. In the following section, detailed information on micropumps, its types and benefits are presented .

2.2 Micropump Technology

Micropumps are an essential component in the field of science ranging from biology to electronic cooling systems to spacecrafts and much more. They can precisely control the pumping of miniscule fluid volumes for efficient working of these micro devices.

One of the main concerns in the field of microfluidics involving OoC is the pumping mechanism, which is used to force liquid flow in the microfluidic channels through the cell culture. Most researchers are trying to switch from the sizeable external pneumatic or peristaltic pumps to miniature pumps. This will reduce the cost and increase efficiency of these on-platform microchips. They are mass producible, easy to transport in bulk, are more reliable, consume low power and can fit along the micro-channels. A typical micropump consists of a reservoir for fluid supply and the pump actuation forces the liquid to the targeted area where a cell culture is present.

They can be classified in two categories: *Mechanical* and *Non-Mechanical*. The mechanical micropumps require a physical pumping mechanism while the non-mechanical pumps convert the non-mechanical form of energy into kinetic energy for the fluid flow in microchannels. [6] The following give examples for both categories. [6]

Mechanical	Non-Mechanical
Electrostatic (Vibrating diaphragm)	Magneto hydrodynamic
Piezoelectric (Vibrating diaphragm, Peristaltic, Flexural plate waves)	Electro hydrodynamic
Thermo-pneumatic (Vibrating diaphragm, Peristaltic)	Electroosmotic (AC, DC)
Shape memory alloys (Vibrating diaphragm)	Electrowetting
Bimetallic	Bubble type
Ionic conductive polymer films	Electrochemical
Electromagnetic (Vibrating diaphragm)	

The most common type of mechanical micropumps are the diaphragm pumps. They work on the following principle: *"repeated displacement of the diaphragm membrane creates a pressure difference inducing fluid flow"*. [40] Since there is no external pump attached to the system, the flow of fluid is achieved by the oscillatory motion of the membrane. The pressure difference (ΔP) as a function of stroke volume (ΔV), which is created inside the pump chamber. The compression ratio (ϵ) can be defined as: [6]

$$\epsilon = \Delta V/V_o \quad (1)$$

Where, V_o = Initial or dead volume

The mechanical pumps which obey this equation of compression ratio are mentioned before. A typical mechanical-displacement micropump consists of a flexible diaphragm (actuator), pumping chamber, fluid inlet and outlet (as shown in Fig - 3). When the actuating diaphragm expands, fluid enters the pump chamber due to difference in pressure via inlet valve. As the actuator compresses, pressure inside the pump chamber increases pushing the fluid out through the outlet valve. The micropumps include valves which influences the flow rate and direction. They can be categorized as: Active and Passive. Addition of valves in microfluidic devices can easily convert an irregular fluid flow into a directional flow. [6]

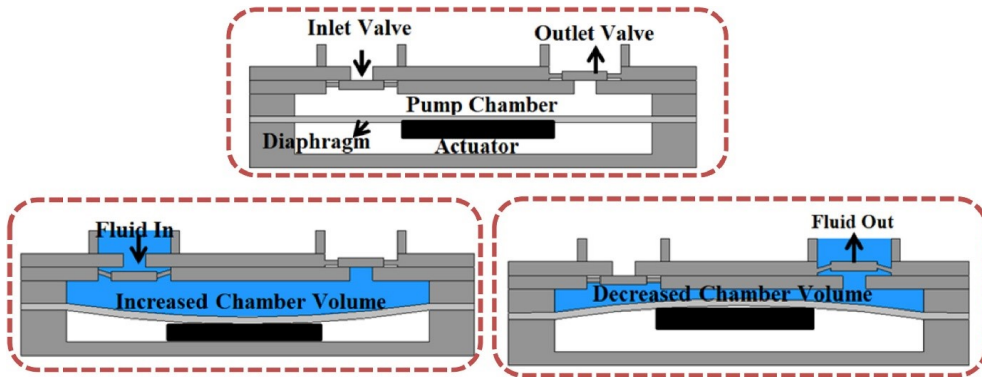


Figure 3: Schematic of a general mechanical micropump. [6]

An active valve requires an actuator to control the opening and shutting of valve during its operation. While a passive valve operates based on the pressure difference created by sinusoidal displacement of the diaphragm. This kind of micropump might seem like an ideal candidate for OoC applications.

However, due to an increase in number of moving parts it is not a feasible option. In such microsystems, these moving parts are fragile and could possibly lead an error due to mechanical failure, high pressure loss, low driving frequency, sensitivity to solid particles, leakage or many other reasons. Also, aggregation of cells close to moving valves eventually leads to clogging during

their circulatory motion through the micro-channels.

To overcome these issues Stemme et al [7] presented the first valveless micropump, which had fixed valves or diffuser/nozzle elements. A valveless micropump does not require unnecessary moving parts and instead relies on the nozzles/diffusers elements to achieve flow rectification in and out of the pumping chamber. Since the introduction of micropumps, the primary focus of most researchers have been on improving their performance and efficiency in order to obtain high flow rates and have a better pressure control over the fluid flow. An important complication with a valveless micropump is the back flow or reverse pressure. This happens when the diaphragm membrane expands to force fluid into the pumping chamber and some volume of fluid flows in the reverse direction.

2.3 Micropump actuation mechanism

In this section different micropump actuation mechanisms will be discussed along with an example for each.

Electromagnetic (EM) actuation

An electromagnetic micropump requires oscillatory motion of a magnetically active membrane/diaphragm to initiate fluid flow in the microfluidic system. The membrane contains a magnetic powder which is actuated using an external electromagnet and is generally placed underneath the pumping chamber. This kind of actuation mechanism is capable of producing high membrane displacement. A valveless design was selected for this system. The diffuser entrance of length 2.3 mm is 100 μm wide with rounded corners, while the outlet is 500 μm wide with sharp corners. The thickness of the nozzle/diffuser elements is 250 μm . The microfabricated EM micropump chamber is 0.5 mm deep and has a diameter of 7 mm. For example, Yamahata et al [8] were able to obtain a membrane displacement of 200 μm and a flow rate of 400 $\mu\text{L}/\text{min}$. EM actuation mechanism can deliver impressive results. However, the electromagnetic field generated can potentially deteriorate molecules in

the cells, cause imbalance in ionic equilibrium and lead to several other chemical effects. [9] Other than that, it requires use of an external magnetic field which restricts the pump size. [10]

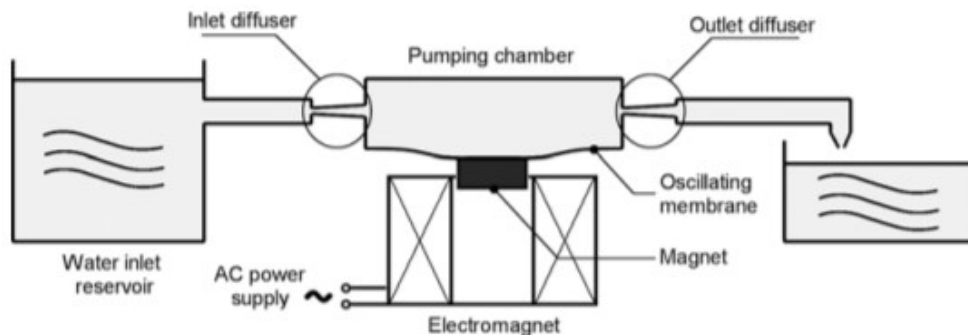


Figure 4: Electromagnetic micropump by Yamahata et al. [8]

Thermopneumatic actuation

The working principle of this mechanism is as follows: An electric heater resistor is placed over the pumping membrane and electrical voltage is applied to it. This causes a rise in temperature inside the cavity, increasing the pressure which in turn deflects the membrane downwards. This leads to an increase in pressure inside the fluid chamber. The inlet valves open due to pressure difference leading to fluid flow inside the pump chamber until pressure in the chamber equals the outside pressure. When the heater is turned off, the air inside the cavity cools down causing a pressure drop which in turn deflects the membrane upwards. Again, due to difference in pressure, the outlet valve opens resulting in a fluid flow. This type of mechanism requires use of heaters which can potentially disturb the cell environment, also the use of high temperature and high-power consumption are the drawbacks of this phenomenon. [11][12]

Electrostatic actuation

This mechanism works on the concept as depicted in Fig. - 5 (a). The electrodes are deposited and when a voltage is applied, it deflects the membrane causing fluid to flow into the chamber due to pressure difference. When the voltage is turned off, reverse process occurs. However, it is complex to micro fabricate the isolated air gap between the diaphragm and top layer of the chamber. Nevertheless, this enables use of conductive and non-conductive

fluids as there is no influence of applied voltage on the fluid. Machauf et al [13] developed a conceptual design (fig. 5 [b]) to overcome the limitations of complex micro fabrication of general electrostatic micropumps. Since, voltage is directly applied to the fluid in this concept, it is not feasible for several OoC applications. [13]

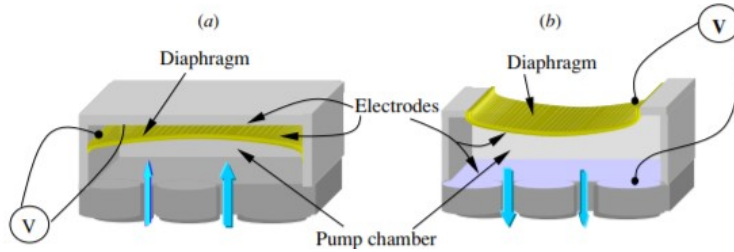


Figure 5: Electrostatic pump schematic.[13]

Piezoelectric actuation

Discovery of piezoelectric effect in 1880 by Curie brothers [14] gave birth to a new class of materials called Piezoelectric materials. They have the ability to generate an electrical charge when mechanical stress is applied on the material. Owing to this phenomenon, researchers in the field of microfluidics shifted their focus on piezoelectric actuators. When fabricated in the form of a thin diaphragm they pose few advantages like low energy consumption, small size, high reliability, precise output and no electromagnetic interference; which makes them quite ideal for micropump applications. [15]

Kan Junwu et al [16] designed and tested a piezoelectric cantilever valve micropump (Fig.- 6) for drug delivery application in 2005. When a voltage is applied the piezoelectric actuator operates in bending vibrational mode. This pressurizes liquid movement in and out of the pumping chamber which propels the check valves to open or close. The check valves provide good control over fluid flow and high flow rate can be obtained along with low back flow. However, the drawback involves low driving frequency which leads to high pulsating flow. [16]

The natural frequency of the actuator should be lower than that of the cantilever valves to attain both low and high frequencies. The author uses

precision impedance analyser to measure the natural frequency of the actuator (PZT) in water and air medium. It was observed that in water the natural frequency achieved was 3.17 Hz whereas in air it was 5.92 Hz, confirming that the liquid has a great influence on the actuator efficiency. Hence, the cantilever valves should be designed in accordance to the medium. The micropump with a cantilever valve length of 2.5 mm had a flow rate and backpressure of 3.5 ml/min and 27 kPa respectively and with a length of 4.5 mm the obtained results are 3.0 ml/min and 9 kPa respectively. [16] Although piezoelectric materials are a popular choice as a diaphragm actuator, requirement of high operating voltage and low stroke volume are major disadvantages for many applications.

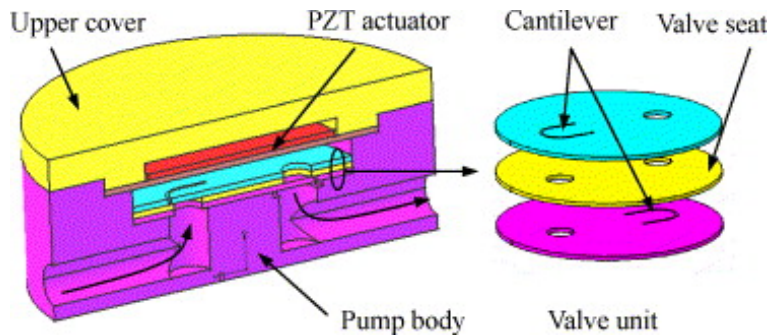


Figure 6: Piezoelectric micropump schematic. [16]

Ionic polymer metal composite (IPMC) actuation

IPMC has gained considerable attention as a micropump actuator due to its large bending displacement at low applied voltages.

Nam et al presented an unconventional multi-actuator IPMC membrane in order to remove the edge constraints. [77] A similar multi-cantilever actuator was developed by [78] for drug delivery applications. [79] designed and predicted the flow rate of an IPMC actuator for a valveless micropump at low Re of 50.

Nguyen et al developed a flap-valve IPMC diaphragm micropump. PDMS is used as a flexible support for the IPMC diaphragm to prevent displacement constraints on the diaphragm. A multilayered IPMC is fabricated for

this purpose and flap valves are made using PDMS. The dimensions of the fabricated micropump is $20 \text{ mm} \times 20 \text{ mm} \times 5 \text{ mm}$. Water is used as the working fluid to investigate the micropump efficiency. The applied voltage and frequency range is 1-3 V and 1-11 Hz respectively. The actuation results represented that the diaphragm displacement decreases with increase in frequency as the mobile ions in the nafion membrane requires time to migrate. At higher frequencies ions unable to migrate properly. Highest diaphragm displacement was obtained at 1 Hz driving frequency for all applied voltages. [76]

2.4 Valveless design and features

The valves are components that regulates and govern the flow in a micropump. They control the fluid flow by opening, closing or by hindering the fluid flow movement. Further, a micropump can be categorized based on the kind of valve design integrated in it. The two categories are: with valve or valveless micropumps.

The micropump which will be used for this project includes a valveless design. The advantage of a valveless micropump is that they do not require any moving parts. This avoids mechanical errors, increase their reliability and lifetime and simplify the fabrication of sub-millimetre devices. [17] There is also a possibility that moving valves can cause damage to sensitive fluids and congestion of cells.

A valveless micropump consists of nozzle/diffuser elements, which are also referred as static valves can change the fluid dynamics. A nozzle can be identified as an element with gradual decrease in the fluid channel cross-section. Whereas, a diffuser is characterized gradual increase in the fluid channel cross-section. Figure - 9 illustrates this difference. In the supply mode, more fluid flow is achieved in the pump chamber via inlet (diffuser) compared the outlet (nozzle). While in the pump mode, more fluid flows through the outlet (diffuser) than through the inlet (nozzle). [8] In order to achieve high flow

efficiency in micro diffusers two valve characteristic features have to be investigated: the overall efficiency and pressure coefficient of individual diffuser. The nozzle/diffuser geometrical parameters (given in figure - 7) are length (L), width (W), angle (2θ), aspect ratio, inlet curvature and fluid density, viscosity and velocity. The fluid properties cannot be altered due to application specification, the only variable parameter is diffuser geometry. [17] The two most common types of static valves include: Diffuser/Nozzle and Tesla valves.

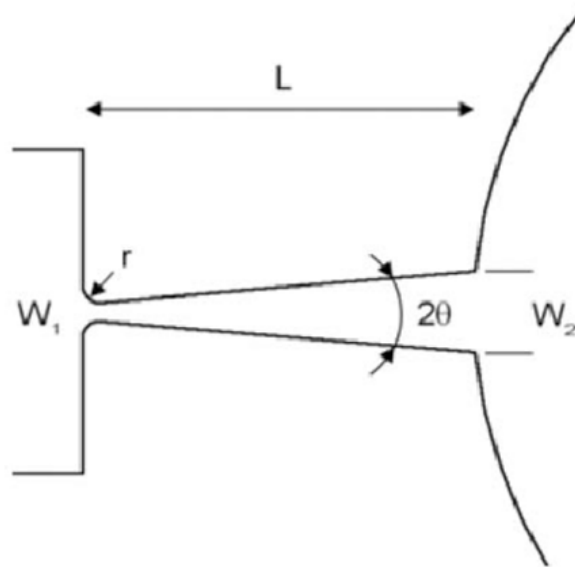


Figure 7: Nozzle/diffuser geometrical parameters. [66]

The Tesla valve (seen in Fig - 8) was invented by Nikola Tesla. It allows a free flow of fluid in one direction without any obstruction other than the surface friction while blocking the flow in opposite direction. [18]

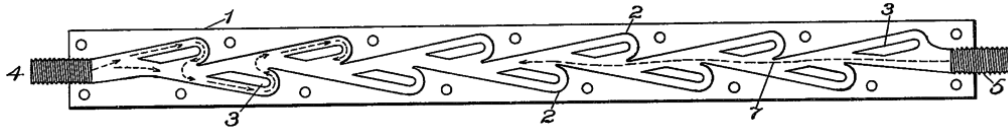


Figure 8: Cross section schematic of a Tesla valve. [18]

Erik Stemme et al [19] in 1993 designed and tested the first valveless diaphragm micropump with two fixed diffusers (expanding duct) / nozzle (converging duct) elements at the inlet and outlet of the pumping chamber. The chamber diameter was 19 mm and could achieve a maximum flow rate of 16 ml/min.

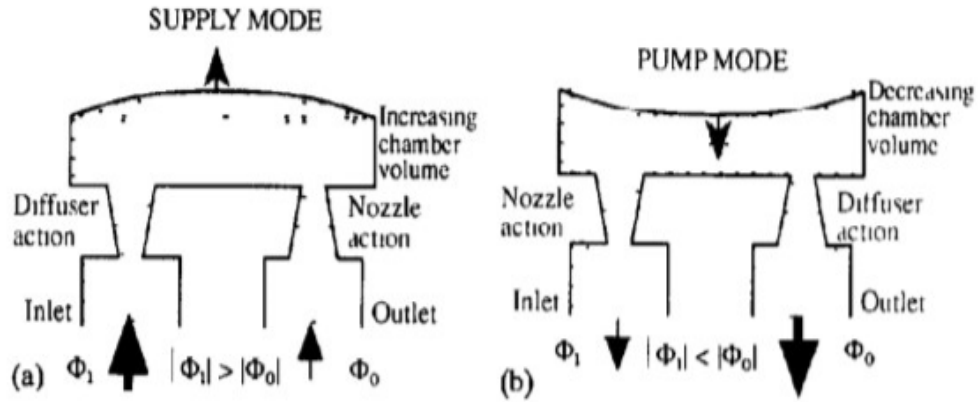


Figure 9: Pumping operation. [19]

Figure - 9 illustrates the pumping principle of a valveless micropump. In the supply mode (fig.- 9a) the the pump chamber volume increases and the inlet acts as a diffuser meaning, large volume of fluid is transported through the inlet than the outlet. Whereas, in the pump mode (fig.- 9b) the pump chamber volume decreases and the outlet acts as a diffuser pumping more volume than the inlet. [19] However, the fact that some amount of fluid flow occurs in both directions cannot be ignored. This is the back flow issue.

As seen in figure - 10, the volume flowing through the diffuser and nozzle can be calculated by the following equation: [19]

$$\phi_d = A_d \cdot \nu_d \quad \text{and} \quad \phi_n = A_n \cdot \nu_n$$

Where, ϕ_x – Volume flow through diffuser / nozzle ($x = d, n$)
 A_x – Cross sectional area of the narrowest part ($x = d, n$)
 ν_x – Fluid velocity in the narrowest part ($x = d, n$)

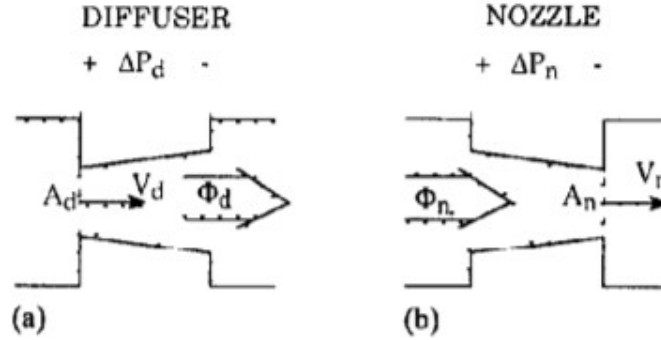


Figure 10: Schematic of diffuser and nozzle. [19]

The final expression of total volume pumped during one pump cycle is given by the following equation: [19]

$$\nu_o = 2\nu_x \left[\frac{\eta_n \cdot d^{1/2} - 1}{\eta_n \cdot d^{1/2} + 1} \right]$$

Where, $\eta_n d = \xi_n / \xi_d$ (ξ – pressure loss coefficient)
 ν_x – Volume variation amplitude

It can be observed from the above expression that $\eta_n d$ should be greater than 1 in order to have a pumping action, higher the value of $\eta_n d$, higher the stroke efficiency. There are mainly two types of diffuser geometries: flat walled and conical (Fig. - 11). A flat walled diffuser has a rectangular cross-section to which flat walls are parallel to each other, whereas a conical one has a cross section which is circular in shape. [19]

Reynolds number (Re) is used to determine the fluid flow pattern as laminar or turbulent. Re tends to decrease as the fluid channel dimensions and flow velocity are scaled down. At low Re, the viscous flow dominates and the fluid flow is Laminar. It is of great importance in microfluidic devices. For this project the aim is to work in laminar regime at high Re.

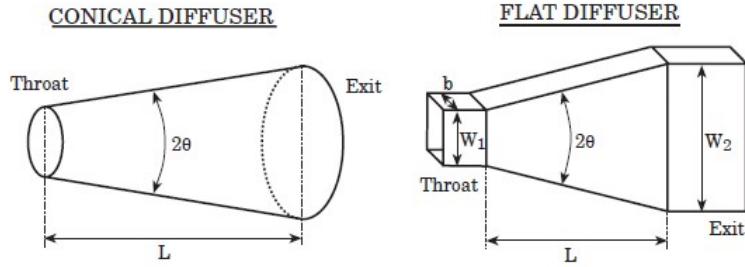


Figure 11: Schematic of conical and flat-walled diffuser geometry. [21]

The flow passing through the diffuser can be determined based on the stability map (Fig. 12). The flow obtained is categorized in four forms:

- No stall region: There is no separation at the diffuser walls and flow is steady viscous.
- Transitory steady stall: The flow is extremely unstable in this region and maximum pressure loss occur.
- Bistable steady stall: A steady stall flow can flip-flop from one diffuser wall to another.
- Jet flow: The flow does not cling to the diffuser walls and pass at a constant rate.

A study on the streamline flow of diffusers show that for a flow in the positive direction there is a flow separation between the main flow stream and the sidewalls. When the diffuser angle (2θ) increases, the flow separation increases giving rise to recirculating zones in the positive flow direction. However, there is no flow separation and recirculating zones are observed in the nozzle direction with the increase in diffuser angle. [19]

Nafea et al [22] investigates the geometrical factors and tuning to obtain the most efficient parameters of the diffuser/nozzle elements for a valveless micropump in COMSOL. The study was performed at Reynolds number (Re) ranging from 10 to 100 and results suggested that a curvature ratio of 0.4 and diffuser angle (2θ) of 10° gives the highest efficiency (Fig. - 13) observing pressure coefficients simultaneously. [31]

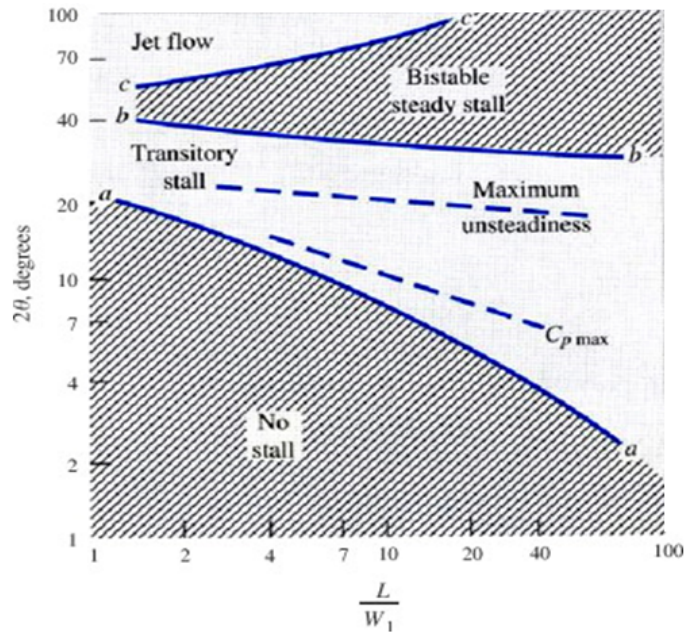


Figure 12: Stability plot for diffuser geometries. [20]

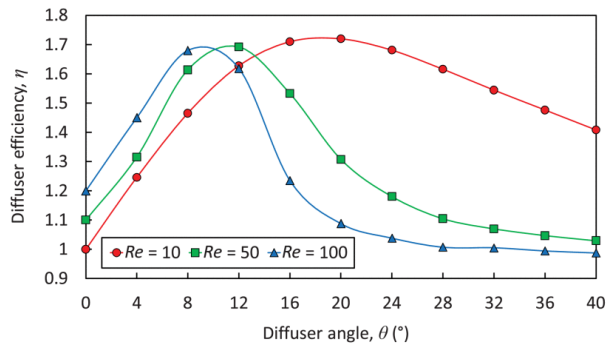


Figure 13: Efficiency plot with respect to diffuser angle for various Re . [22]

Figure - 14 illustrates the change in diffuser/nozzle efficiency with respect to the curvature ratio and diffuser length at a fixed Re of 100. Moreover, at low diffuser angles indicates a low flow separation and high-pressure recovery in positive flow direction, and vice versa in the nozzle direction (negative flow direction).

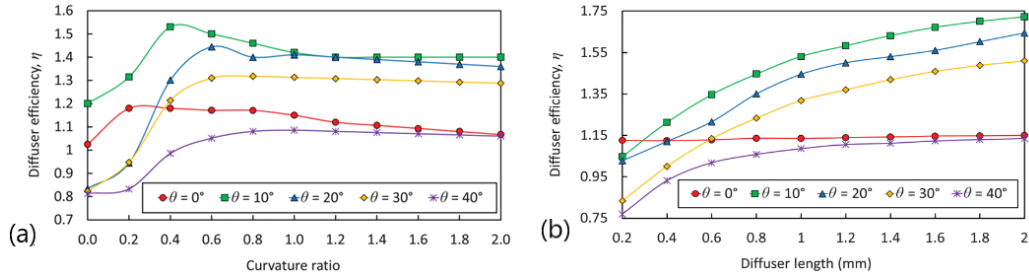


Figure 14: (a) Efficiency versus curvature ratio for different θ at $Re=100$. (b) Efficiency versus diffuser length for different θ at $Re=100$. [22]

2.5 Electroactive polymers (EAPs)

Electroactive polymers (EAPs) have come out as a remarkable material for biomedical applications because of their non-toxicity, low degradation rate, flexible and good functional properties. The researchers are attracted to this material due to their good electro-mechanical properties, ease of fabrication, light weight and superior mechanical and chemical stability. The actuation in such polymers can be achieved by polarization, molecular shape and phase change, and mass/ion transportation. They can be classified depending upon their activation mechanism as: [23]

- Ionic electroactive polymers (IPMC, etc)
- Electric electroactive polymers (Dielectric EAP, ferroelectric polymers. etc).

The phenomenon of migration of ions in an ionic EAPs (iEAP) is activated by the force generated from the electric field at low voltages. While the Electric EAPs have large electromechanical coupling efficiency and require high voltage. The actuation in dielectric EAPs is due to electrostatic forces. [23] Principally, an ionic electroactive polymer can swell, shrink or bend in a controlled manner in response to an applied electric field. They can directly transform electrical energy into mechanical energy by the ion transport mechanism and have several potential applications in the field of science

and technology. A few examples include artificial muscles, soft robotics, drug delivery, actuators for micropumps, and many more. [24]

Table 1: Brief summary of EAPs.

EAP Type	Advantages	Disadvantages
Electric	<ul style="list-style-type: none"> • Can operate in air, water or vacuum (Ferroelectric specifically) • Long operation period. 	<ul style="list-style-type: none"> • Activation requires high input voltage • Operation is temperature limited
Ionic	<ul style="list-style-type: none"> • Induce quick bending displacement • Require low voltage 	<ul style="list-style-type: none"> • Can maintain wetness • Do not hold strain under DC voltage

The extraordinary conversion of electrical energy into mechanical displacement is observed due to the ion migration mechanism. This leads to the surface expansion at one end and shrinkage at the other. [24] The iEAP based micropumps are the recent technological challenge as they require long term usage (> 6 months) without degradation or failure and reducing its size (to micro or milli meters) induces further complexity. [23]

While the iEAPs have several benefits and applications as an emerging smart material, the aim of this project is to employ an iEAP as the diaphragm actuator material in a micropump for OoC applications.

2.5.1 Nafion characteristics

Nafion is an electroactive polymer first produced by DuPont Company. It has a per-tetrafluoroethylene (PTFE) backbone structure with short per-fluoroethylene side chains. The hydrophilic anionic sulfonate (SO_3^-) groups are attached to the ends of the side chains as seen in figure-15. [41]

Nafion and Flemion are termed as ion exchange polymers which are specifically designed to exchange ions selectively of a single charge (anion/cation) with their own existing ions. The major difference between Nafion and Flemion (fig-16) polymer structure is the fixed anionic end group, sulfonate groups in case of Nafion and carboxylate in Flemion. The iEAP which will be of focus is Nafion and Nafion-117 used for this project is 180 μm thick. The negative ions (anions) are fixed in place due to their high bonding strength with the carbon chains in the polymer. When hydrated with an ionic solvent, the positive ions (cations) such as calcium, lithium or sodium ions enter the polymer and can move around freely. [27] The backbone polymer chain is

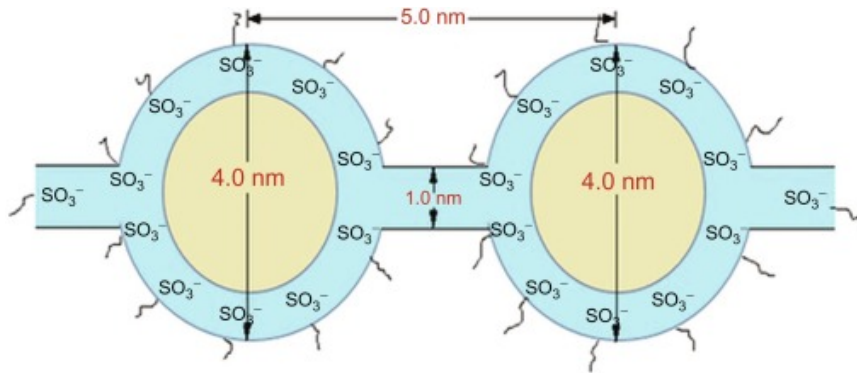


Figure 17: Schematic of the sulfonate clusters. [32]

2.6 Ionic polymer metal composite - IPMC

Over the last few decades, miniature pumps or micropumps have gained importance in many fields of science and are still under development. The main feature of a micropump is the actuation mechanism which determines its fundamental characteristics like flow rate, efficacy, design, cost and many more. In this thesis project, Ionic polymer metal composite (IPMC) is used as the micropump diaphragm actuator material.

Ionic polymer metal composite or IPMC is a lightweight, flexible, biocompatible electroactive material that can operate in wet, humid and dry environment (best in former two). It is capable of producing large bending displacements upon the application of low voltages and can deform thousands of numbers of times without attaining any mechanical failure. Typically IPMC consists of an electroactive polymer (Nafion or Flemion, discussed previously) sandwiched between thin layers of a highly conductive noble metal like platinum, silver or gold. It is a class of synthetic composite materials which under applied voltage can behave similar to a human muscle movement. [26] IPMC possess an interesting property that it is capable of absorbing large amounts of polar solvents, up to 20% of its volume (i.e. water). [28]

The working principle of an IPMC membrane is depicted in fig - 18. In the actuation mode when a voltage difference is applied, the mobile positive ions in the ionic polymer migrate towards the cathode along with the bonded wa-

ter molecules. This results in the clusters near the cathode to be cation rich. The free water molecules present inside the material also migrate towards cathode due to electro-osmotic drag. Electro-osmotic drag is the movement of neutral solvents associated with the movement of ions when electric field is applied. The migration process expands Nafion locally at the cathode and contracts it at the anode. This leads to mechanical bending of IPMC. [68] This process results in a charge imbalance inside the membrane along with a local charge imbalance which produce a change in the osmotic pressure and the electrostatic forces inside the cluster. However, the overall charge neutrality is maintained. The macromolecules of Nafion polymeric network are crosslinked non-uniformly, which also leads to uneven distribution of the ionic charges within the polymer framework. [33] The osmotic diffusion of the ions, solvent and counterions in and out of Nafion are closely related to the swelling and contraction of the polymer matrix. However, water based IPMCs extraordinarily dehydrates when driving voltage over 1.23 V is applied. This is because of electrolysis phenomenon. Electrolysis is a process to decompose water into oxygen and hydrogen using electricity. [67] Natural evaporation of solvent is another factor associated with the dehydration of IPMC.

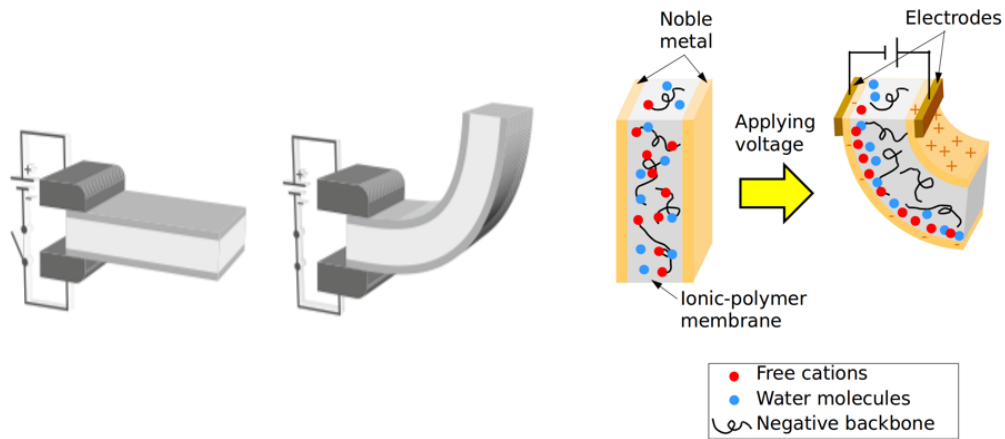


Figure 18: Schematic of back relaxation phenomenon.

Similarly, in the sensing mode, when mechanical deformation is applied on the IPMC surface, ion migration due to stress gradient produces a volt-

age drop, which can be sensed as the output signal. [30][82]. As stated by *Shahinpoor et al* [28], when a low voltage is applied (2 V or higher) to an IPMC film it bends towards the anode; higher the voltage applied, more the displacement is observed. The bending performance of the film is heavily dependent on the available water content and cation molecular size inside the polymer membrane.

Figure-20 briefly describes the molecular behavior of Nafion which leads to bending deformation of IPMC.

Back relaxation (figure-19) of electroactive polymers is another important phenomenon which occurs during the deformation of this material. It has been reported that during the actuation process, IPMC with Nafion will quickly bend towards the anode followed by a slow back relaxation towards the cathode if the voltage is held constant for a certain duration of time. This limits the use of this material at low actuation frequencies. *Maurizio et al* [42] has reported that this phenomenon is dependent on the type of electroactive polymer used, polymer thickness and the water content present inside the material. In addition to that, the type and size of the counter ion also affects this process. However, no back relaxation is observed in case of Flemion. The IPMC produced using Flemion will quickly bend towards the anode upon applied voltage followed by slow bending in the same direction and vice-versa when polarity of the voltage changes. [67]

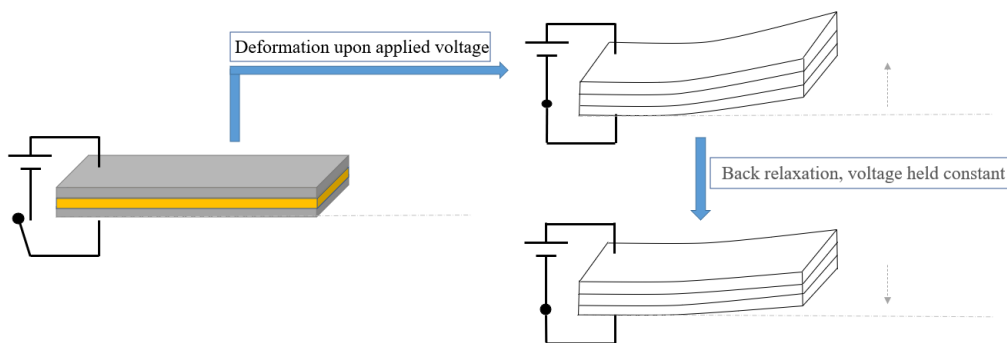


Figure 19: Schematic of back relaxation phenomenon.

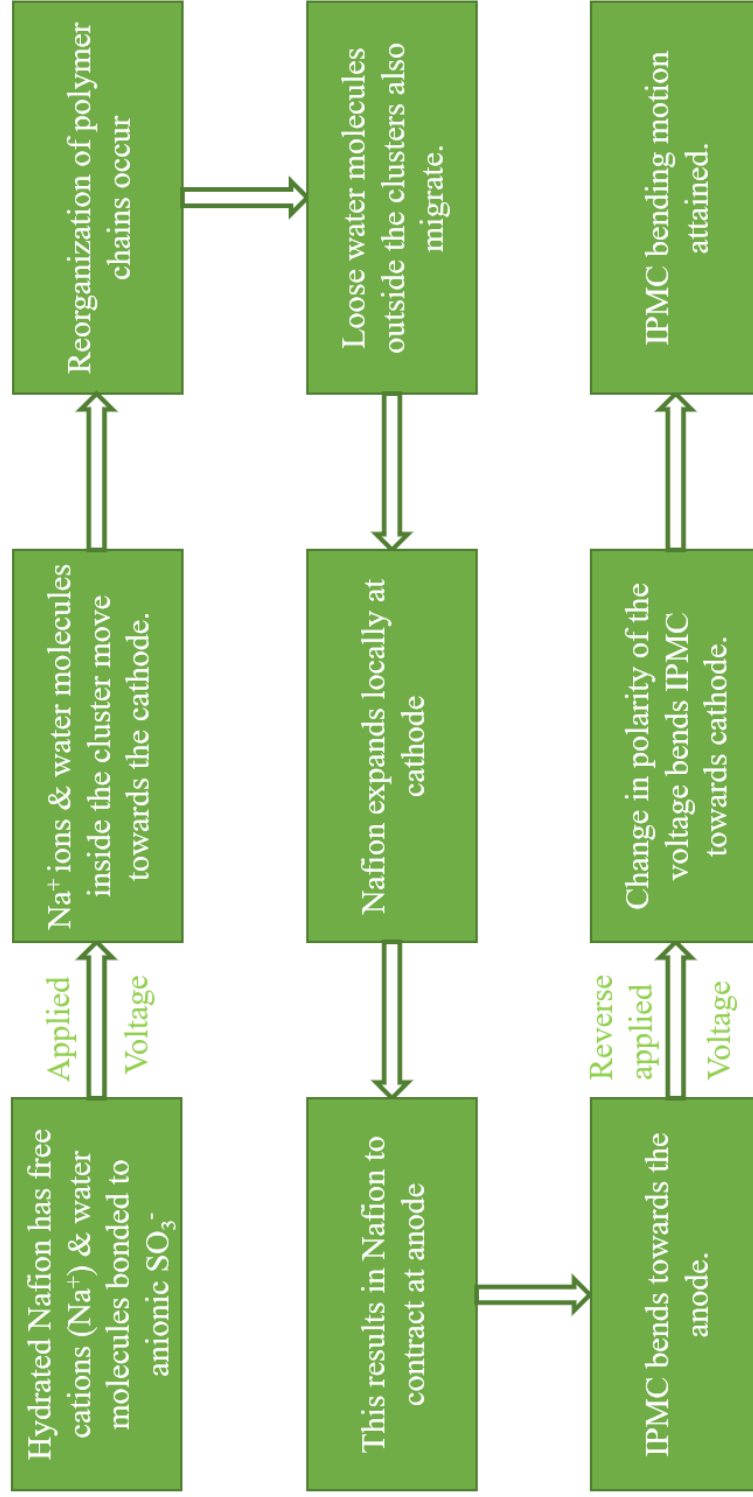


Figure 20: Molecular and macroscopic behaviour of IPMC with Nafion.

Large ions tend to reduce the range of back relaxation. A reasonable accepted explanation for this process is linked to diffusion of solvent molecules inside the material. [43] When voltage is applied, the cations quickly migrate towards the cathode. If the voltage is held constant, the free water molecules start to diffuse back into the polymer matrix until equilibrium is attained. At macroscopic scale the material will bend itself in the other direction, towards its original position. This leads to the phenomenon of back-relaxation. Figure - 19 depicts the back relaxation process.

IPMC is used as the diaphragm actuator for an upcoming micropump in this thesis project. For IPMC or any other material to be used as a diaphragm actuator, the main attribute that it should possess is the production of a high generative force. Higher the force exerted by the actuator, higher the stroke volume. The researchers have proposed that increasing the thickness of the nafion membrane by the casting method can lead to an increase in the generative force upon actuation. [70] However, it is not a feasible option since the nafion produced by DuPont has a maximum thickness of approximately 180 μm and the casting process require additional manufacturing steps, including use of solution based nafion.

When the IPMC is actuated, on a molecular level, there occurs a structural reconfiguration of the polymer chains. It is well known that the polymer chains are arranged in a spaghetti like structure. When an experiment is stopped abruptly, the polymer chains attains a different chain configuration. Hydration of the membrane post experiments relaxes the already strained polymer chains, regain ion concentration, induce ion mobility and form molecular aggregates.

As described in the next chapters, the cantilever shape IPMC used for this thesis project is smaller in length than used in any published research until now. The following table provides a brief overview of the IPMC dimensions used in literature as an actuator:

Table 2: Few examples of IPMC dimensions used in the literature.

S.No.	Ref. No.	Length (mm)	Width (mm)	Thickness (mm)	Voltage (V_{pp})	Frequency (Hz)
1	[23]	28	4	0.2	Sinewave, 2.5 V	1 – 8
2	[24]	30	4	0.4 – 1.2	Sinewave, 2 – 5 V	0.5
3	[37]	20	5	0.6	AC voltage, 1 – 3 V	1
4	[26]	50	7.5	0.3	-	-
5	[27]	30	5	0.3	-	-
6	[28]	10	2	0.2	Squarewave, 1.5 V	-
7	[35]	10	5	0.2	Squarewave, 2.5 V	5
8	[30]	20	5	0.4	Squarewave, 2 – 4 V	0 – 1.5
9	[34]	20	4	0.2	Sinusoid, 2	0.1 – 35
10	[35]	15	5	2	Stepvoltage; 2, 4, 6	0.5

Owing to these molecular phenomena, different bending characteristics can be explained at a macroscopic level.

3 Research Methodology

A crucial characteristic of an efficient diaphragm actuated micropump is the amount of pressure or force that the diaphragm actuator can generate during its actuation cycle for an optimum flow rate. Since the actuating diaphragm is the only moving part which is capable of developing pressure difference inside the micropump for the fluid flow. The force it can generate is directly proportional to the efficiency of the micropump. Many researchers have performed the force and displacement measurements on IPMC but none of them were carried out on small lengths of 7 and 9 mm, width of 2 mm, as we require for our microfluidic device. A 11 mm IPMC was also used for the measurements.

The tip-force and tip-displacement characterization experiments were performed on IPMC material of lengths: 7, 9 and 11 mm; width: 2 mm and thickness: 200 μm . The acquired IPMCs were clamped between the gold electrodes which makes the active actuating lengths to be 5, 7 and 9 mm respectively. The density measurements were also performed using the Archimedes principle along with a theoretical analysis.

The parameters obtained from the experiments and approximations were used as an input for finite-element simulations to predict the behavior of an IPMC-based diaphragm micropump. This will be discussed in Chapter-5 in detail.

3.1 Density measurements and approximation

Density is a vital material property and it can be applied to estimate various other material properties like the volume of irregular material specimens, stiffness coefficient and many more. It is quite simple to measure the density of classical solid materials like polymers, metals and ceramics. The density approximation of the IPMC is quite important because the density value especially depends on the manufacturing process. Also, quick dehydration

phenomenon can lead to change in the density value of an existing specimen. For an optimum mechanical output the IPMC membrane should be in a wet or humid environment.

In 1998, *Shahinpoor et al* [40] reported that the density of IPMC can range between 1 – 2.5 g/cc depending on the manufacturing process. *Lee et al* [41] also assumed the density of their IPMC samples to be 2500 kg/m³. Since the range is quite high, having a density value for the in-house manufactured IPMC could help with the estimation of other material parameters. It can further be used as an input in COMSOL simulations to study the material behavior. Based on this, two measurement methods were shortlisted: He-Pycnometer (also called gas-pycnometer) and Archimedes principle experiment.

The gas-pycnometer is a device which can measure the density of regular or irregular shaped and porous or nonporous solids. It is an ideal non-destructive measurement technique to accurately test the true density of a sample. This apparatus measures the volume of gas displaced by the sample to determine the sample density. [71] Since the IPMC sample which was used for this purpose (figure-21) was an irregular shaped specimen, and being a porous material this technique seems feasible. However, upon trial it was observed that the IPMC sample is too lightweight and small in size. A perfectly shaped IPMC sample was not used for these measurements because of its limited availability. The fabrication process is extremely time consuming and requires use of some dangerous chemicals and specific lab training.

Archimedes principle experiment was finalized and performed on the same sample. The working principle is stated as, "*The volume of the water dispersed by the immersed sample is equal to the volume of the sample.*" Then the density of the sample can be determined using the volumetric density equation. The schematic diagram of the test setup is given in figure-22:



Figure 21: IPMC sample ($12 \times 12 \text{ cm}^2$) used for density measurement.

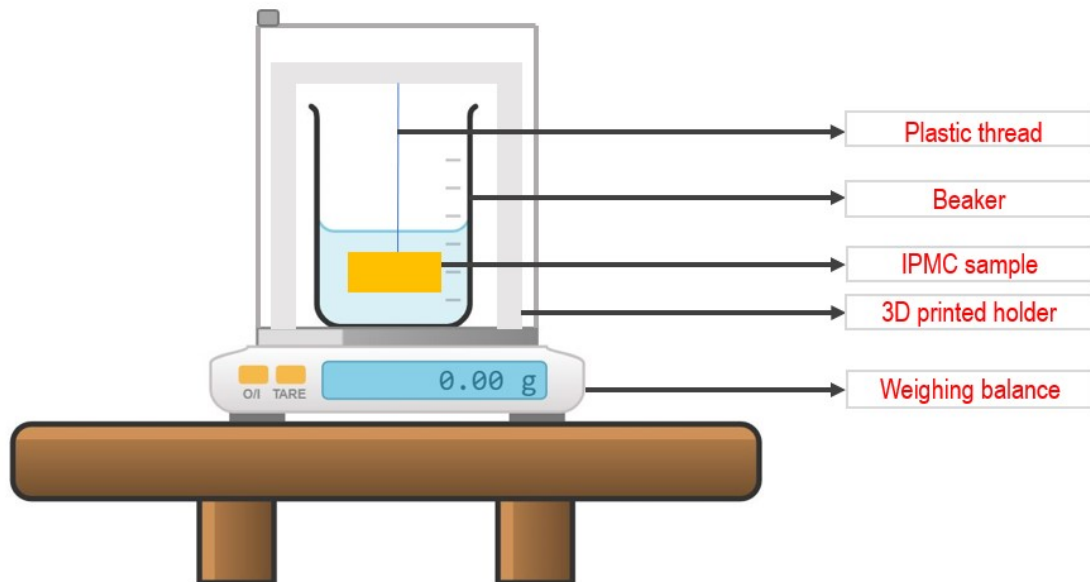


Figure 22: Archimedes experiment setup schematic.

As seen in figure-20, a holder was 3D printed to fit inside the weighing balance and the IPMC sample was immersed in water using a wire tied to the holder. The sample weight was first measured in air, then the change in

weight was measured when immersed in water. The analytical balance from ALLScales with a maximum capacity of 220 mg was used for this experiment. The sample weight in air was measured to be 0.3057 grams. The equation used to calculate the density of the sample using Archimedes experiments is as follows :

$$\rho_s = \frac{W_a}{W_L} \times \rho_w$$

where, W_a - Sample weight in air,
 W_L - Sample weight in liquid (water) and
 ρ_w - Density of water (0.997 g/cc)

3.2 Tip-Force measurements

IPMC acquired for the tip-force measurements are 7, 9 and 11 mm long; 2 mm wide and 0.2 mm thick ($2 \times 10 \mu m$ - Platinum + $180 \mu m$ Nafion-117). They are cut into cantilever shaped specimens using the laser cutting technology in order to have a well defined shape and stored in PBS solution at room temperature. A load cell is used to measure the force generated by the IPMC tip when it hits the sensor surface upon the input of a square voltage. A load cell is a force transducer which is capable of converting forces like tension, compression, torsion or pressure into electrical signals, which can be further analyzed. [72] The load cell used for this measurement is a Futek 10 g (LSB200) S-Beam load cell sensor which was calibrated to sense a maximum force of 11 mN (milli-Newton) and was procured from the 3ME measurement shop, TU Delft. The load cell makes use of the Labview software to readout the acquired tip-force signal in real-time. The data is saved as a *.txt* file. There always exists an offset error in the data received from the load cell which fluctuates with every experiment and should to be taken into account. A detailed explanation on the fluctuating offset error can be found in [73]. This offset value is subtracted from the resultant force values in order to interpret the results accurately. The data file free of offset error

is then imported and analyzed in Python.

All the experiments were performed at room temperature and humidity. Each experiment lasted approximately 110-120 seconds and the IPMC was dipped in the PBS solution post each measurement for approximately 10 minutes. The main reason for dipping the IPMC into the PBS solution is to re-hydrate the material and let the electro-active polymer regain the ionic concentration. Phosphate-buffered saline (PBS) solution is a water based salt solution used as the ion exchange solution for our IPMC samples. The experimental parameters are constant for all the experiments that will be discussed in this report.

The measurements were performed at different peak to peak voltages (V_{pp}) from a minimum of 2 V to a maximum of 4 V with an increment of 0.5 V (i.e., 2, 2.5, 3, 3.5 4 Volts) and at different frequencies of 0.1, 1 and 5 Hz. The input actuation peak to peak voltage signal is a square wave (figure-25) which is centered around 2.5 V and the code was written in the MATLAB designer app.

Schematic diagram of the tip-force experiment setup is given below:

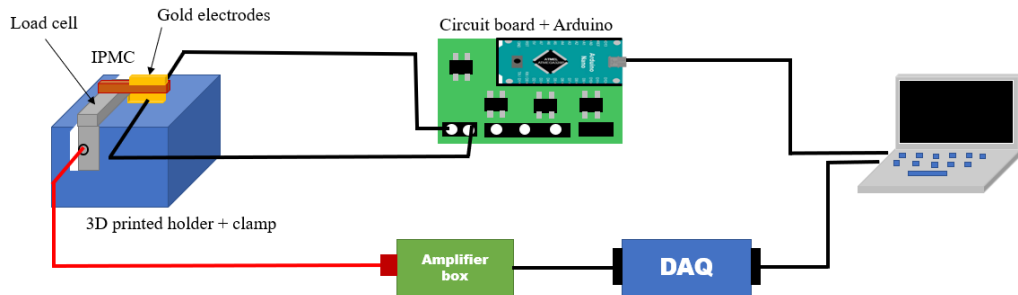


Figure 23: Schematic of Tip-force characterization setup.

And figure-24 gives a closer look of the real setup. It was modelled in Solidworks and 3D printed in order to perform the tip-force measurement. It can be seen that the load cell was fixed in a cavity for stability as it is extremely sensitive to vibrations. For that reason, the setup was placed at the edge of the table to minimize vibrations from the laptop and other factors that could potentially affect the measurement results. A bar of 1 g gold was

flattened using a commercial rolling mill. Then, the flattened piece of gold was cut into 2 mm wide rectangular pieces and soldered to electrical wires to make the gold electrodes. The clamped region for all the IPMCs is 2 mm wide and long, making the active actuating part to be 5, 7 and 9 mm long.

The gold electrodes are connected to a circuit board. Arduino Nano micro controller pinned is onto the circuit board, which is connected to the laptop. The gold electrodes were taped to the setup, the wet IPMC was taken out from the PBS solution, clamped between the gold electrodes and the plate was screwed on top for fixing the electrodes and the IPMC sample in place. The plates is tightly screwed together to the setup holder in order to avoid any manual error. When the setup is ready, the LabView software is run followed by selection of the square waveform at a desired voltage and frequency (as seen in MATLAB UI). When the voltage signal is generated the IPMC produces a bending motion. The LabView and MATLAB programs are paused after completion of the experiment, IPMC is removed from the clamp and dipped back into the PBS solution. Figure-24 also depicts stain and damage caused because of electrolysis. It can be seen as black blemish around the IPMC sample.

The data acquired from the load cell is saved directly as a *.txt* file which is then post processed in Python and the code used can be found in Appendix-1. An example of a processed data is given in figure-26 (the red crosses indicate the peaks using the `find_peaks` function in python).

It can be observed in figure-26 that the first 5 - 10 seconds of the output force signal is unstable. This correlates to the time difference between which the LabView software was turned on and the actuation voltage was applied, during the beginning of the experiment. Hence this data is ignored. Some unwanted peaks exists at the lower part of the force signal plot (a clear representation in figure-27). To obtain only the values of interests from such a big data set, a 10 second window of the acquired force signal was formed. The window is then incremented by 10 seconds and the result was calculated while sweeping throughout the data. This was done for all the recorded force data. Figure-27 and 28 give examples of two 10 second windows.

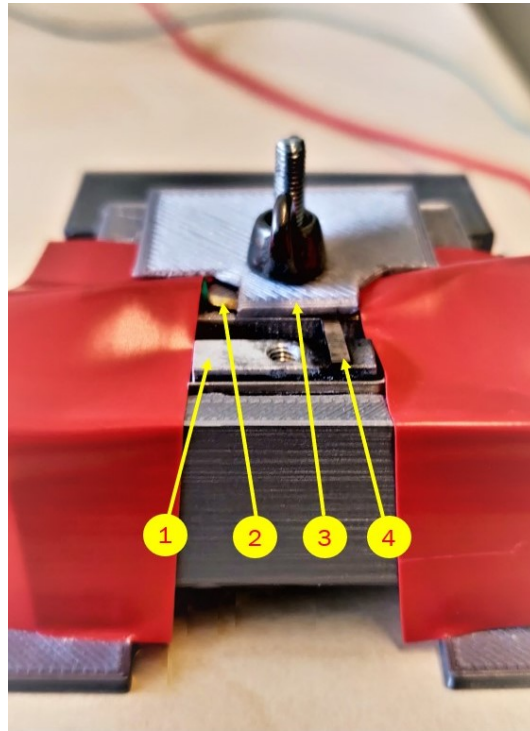


Figure 24: A closer look of the real setup. 1. Load cell surface, 2. Gold electrodes, 3. Fixing plate and 4. IPMC sample (9 mm).

In figure-27, some small peaks are observed (circled) which have a span of approximately 0.001 - 0.003 mN. This can be a result of a very short relaxation period which can be observed at 1 Hz. Hence while calculating the absolute force span and peak tip-force mean, such peaks are disregarded.

Figure-27 and 28 also represents a good actuation behavior of the IPMC sample since number of peaks in the output tip-force signal correlate with the input square wave voltage frequency (for 1 Hz driving frequency, 10 peaks should be observed in 10 seconds).

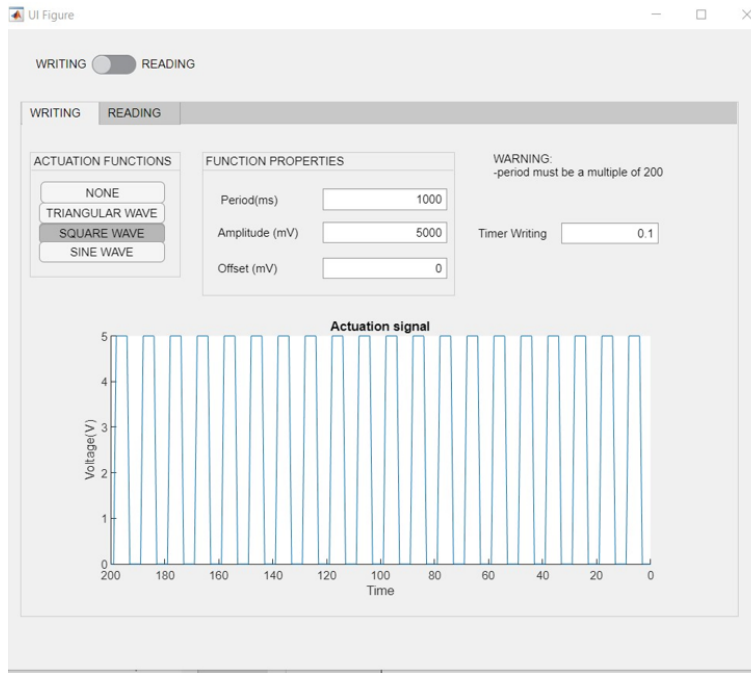


Figure 25: Illustration of the MATLAB designer UI for voltage application.

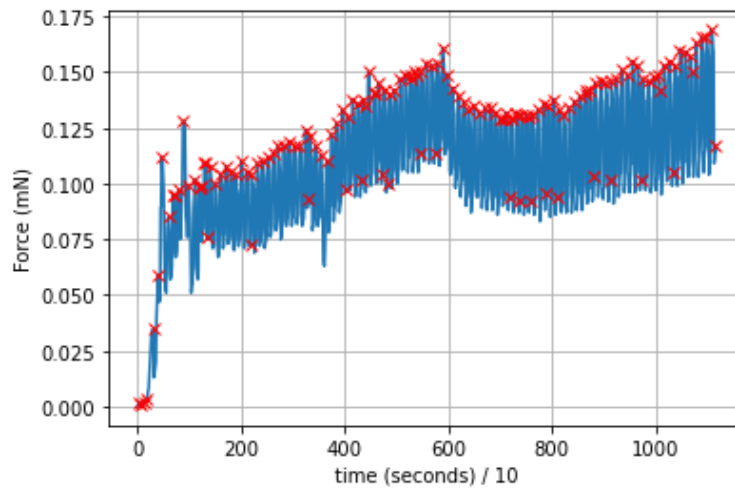


Figure 26: An example of tip-force plot for 7mm IPMC, $4 V_{pp}$ at 1 Hz.

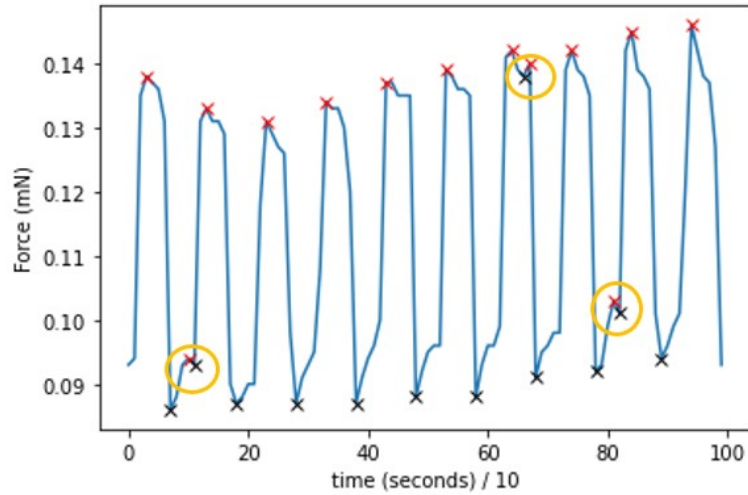


Figure 27: 10 second window of fig-26. Peaks and valleys represented as red and black crosses respectively.

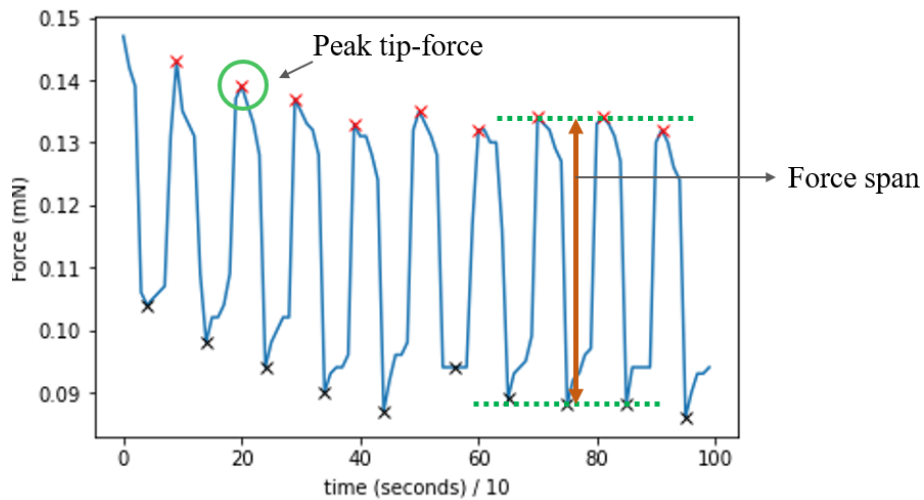


Figure 28: An example of to explain peak tip-force & force span.

In this report, peak tip-force refers to the maximum force that the IPMC sample tip can apply on the load cell during its deformation towards the sensor. It can also be considered as the highest pushing force. Whereas, force span refers to the force applied by the whole active actuating part of the

IPMC sample on the load cell during one actuation cycle. Another distinguished force that can be interpreted from the resultant signal is the pulling force. It is the force which the IPMC sample exerts on the sensor while deforming away from the sensor surface. It occurs in the presence of a water interface between the sample and the sensor surface (IPMC when taken out of PBS solution is wet. Then the experiments are performed in air.) This force is sensed as a negative force by the load cell. It is crucial to differentiate between these forces as only the most significant results should be used to assess the efficiency of the projected micropump.

At a frequency of 1 Hz, 10 experiments were recorded for the IPMC of lengths 7, 9 and 11 mm at every peak to peak voltage. This was done to ensure that the results can be reproducible within the error range if all the experimental and environmental conditions are constant. Also, results obtained for the experiments performed in this project have a high deviation due to complexity associated with IPMC material, like different volumes of water intake, dehydration due to natural evaporation and electrolysis, accumulation of electrons on Pt surface causing the capacitance effect and mechanical and molecular hysteresis. Other factors affecting the experimental results could be unwanted noise or vibrations, dissimilar output than the applied input peak to peak voltage and loss of data due to low bandwidth of the acquisition system (i.e. the laptop used). Each data set has approximately 110,000 to 120,000 data points which corresponds to the amount of recorded data time in milli-seconds. Absolute mean of the force span and the peak tip-force with standard deviation for each experiment is calculated. Furthermore, the mean of means and their standard deviation are also represented. The results are illustrated and discussed in Chapter-4.

3.3 Displacement measurements

IPMC specimens used for the tip-displacement measurements are identical to that used in the tip-force experiment. Schematic of the displacement measurement setup is given in figure - 29.

A setup for this measurement (figure-30) was 3D printed and includes

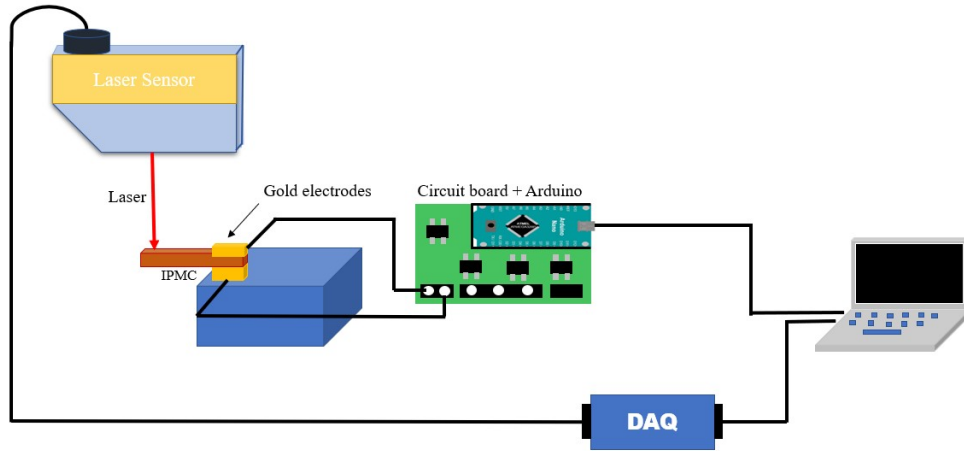


Figure 29: Schematic of tip-displacement measurement.

two holders. A sensor casing, which is used to hold the displacement sensor above the IPMC clamp. This casing is screwed to a holder such that laser from the sensor hits the IPMC sample tip. It also provides additional support and stability to the displacement sensor.

The IPMC clamping system is the same as used in the previous experiment but without the load cell. It is removed from the cavity in order to provide free bending motion to the IPMC sample in transverse direction. The displacement sensor was positioned such that the laser strikes the IPMC sample surface just few micrometers before the tip end. This is done to make sure that the laser spot is restricted to the actuator tip surface and is not off limits during the experiment.

The displacement sensor used for this experiment is a Micro-epsilon optoNCTD 1700, which has a minimum and maximum sensing range of 20 and 30 mm respectively. It has a resolution of 0.01 mm and sensing frequency of 500 actuations per second. The spot diameter of the laser is approximately 1.80 mm.

The experimental conditions and actuation parameters were the same as discussed in the previous section. Tip-displacement experiments were performed at 4V on the IPMC sample of length 7 mm at different frequencies of

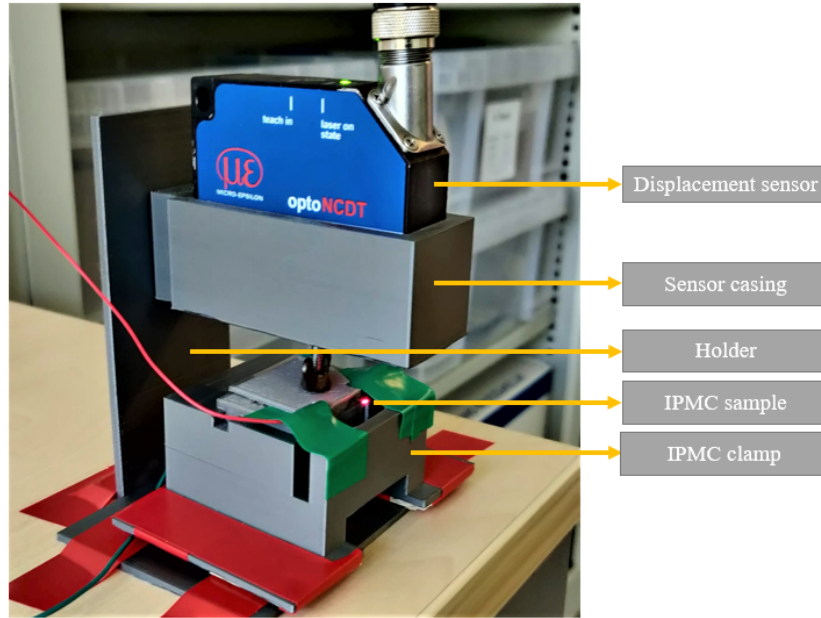


Figure 30: The initial tip-displacement experimental setup.

0.1, 1 and 5 Hz. Method used to determine the total displacement for this measurement is similar to the one used for force span calculation.

Figure-31 presents an example of displacement signal at 0.1 Hz. It depicts the formation of step like features. This does not correlate to the force signals acquired at this frequency, which has well structures (refer to figure-37, section 4.1, chapter-4). It was determined that this signal behaviour is due to low resolution of the sensor. Hence a higher resolution laser sensor was procured. The new sensor is a Micro-epsilon optoNCTD 1750 laser sensor. It has a resolution of $2 \mu\text{m}$, minimum and maximum sensing range of 24 and 26 mm respectively, and the laser spot diameter of $80 \mu\text{m}$. A different setup was 3D printed for the new displacement sensor, given in figure-32. The signal acquired for this measurement is post processed in a similar manner as discussed before and the python code is available in Appendix-1. Also, the results discussed in the next chapter for this measurement are performed using the new displacement sensor.

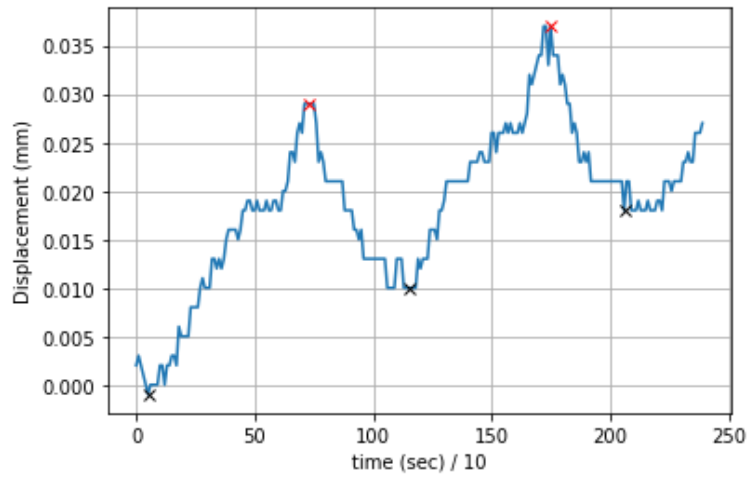


Figure 31: Example of a displacement data window obtained at 0.1 Hz with 10 mm laser sensor.

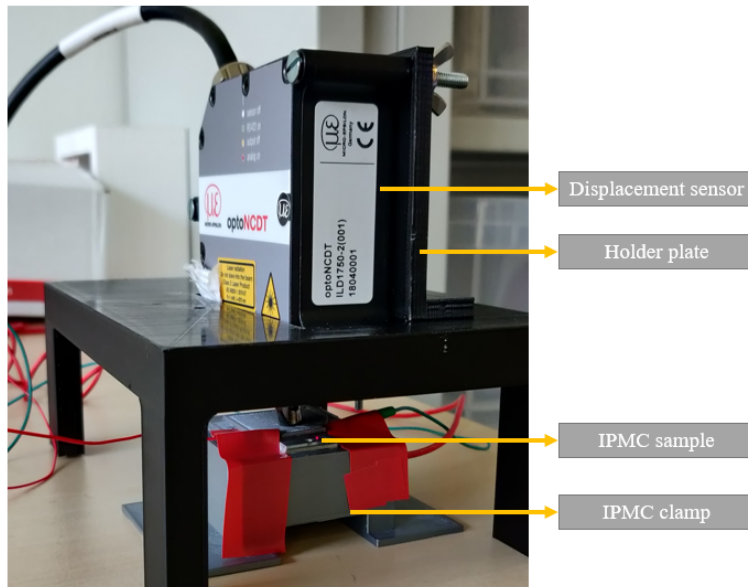


Figure 32: The second laser displacement sensor setup.

4 Results

4.1 IPMC Tip-force

Force results obtained for the IPMC samples of lengths 7, 9 and 11 mm at different frequencies are presented in this section. The signal detection and evaluation process along with the experimental parameters have been discussed in the previous chapter. The wet IPMC samples are actuated in air for all the measurements. This section is categorized based on the input driving frequency. Force signal data is represented only for relevant peak to peak voltages, the remaining plots can be found in appendix -3.

- **1 Hz**

Peak tip-force and force span results for 1 Hz actuation frequency are given below. Figure - 33, 34 and 35 presents the resultant force signal of the IPMC samples. A total of 10 experiments per voltage were performed. Force span and peak tip-force obtained for each sample are given in table - 3, 5 and 7 and table - 4, 6 and 8 respectively. Reader is advised to check figure - 28 for a better representation of the peak tip-force and force span.

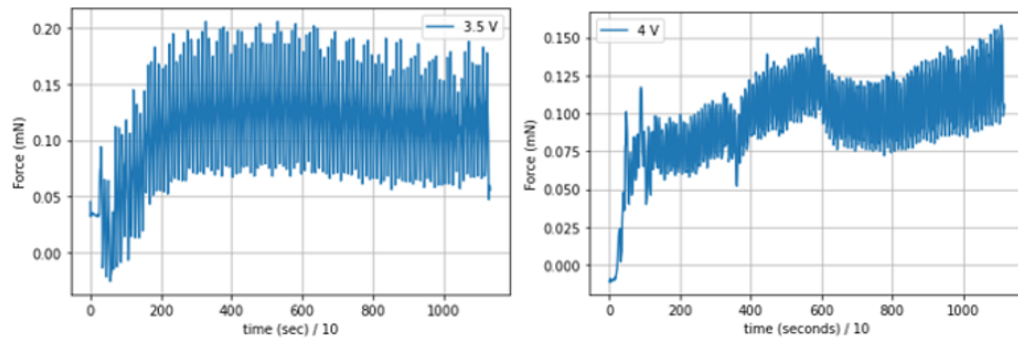


Figure 33: 7 mm IPMC output force signal at 3.5 and 4 V_{pp} .

Figure - 33 represents the force for the 7 mm IPMC sample. The signal for 3.5 V actuates steadily around 0.12 mN. Whereas, the signal for 4 V includes

slight shifts, specifically around 35 seconds and at 60 seconds. The first shift in signal is because of unwanted vibrations since the signal return back to its steady state. However, the second shift occurs as the water interface is disappears due to electrolysis. Since the applied voltage is high, electrolysis occurs after a short duration of time. The signal shift in figure - 34 is due to the same reason a the force span increases after the shift.

Highest peak tip-force and force span for this sample is obtained at 3.5 V_{pp} . The same is represented in table - 3 and 4.

Table 3: Force span for 7 mm IPMC at different applied voltages.

Length (mm)	S.No.	Voltage (V_{pp})	Mean Force (mN)	Standard deviation
7	1.	2	0.0093	0.0049
	2.	2.5	0.0301	0.0123
	3.	3	0.0558	0.0250
	4.	3.5	0.0786	0.0361
	5.	4	0.0678	0.0496

Table 4: Peak Tip-force for 7 mm IPMC at different applied voltages.

Length (mm)	S.No.	Voltage (V_{pp})	Mean Force (mN)	Standard deviation
7	1.	2	0.0295	0.0192
	2.	2.5	0.1036	0.0534
	3.	3	0.1370	0.0710
	4.	3.5	0.1380	0.0740
	5.	4	0.0890	0.0527

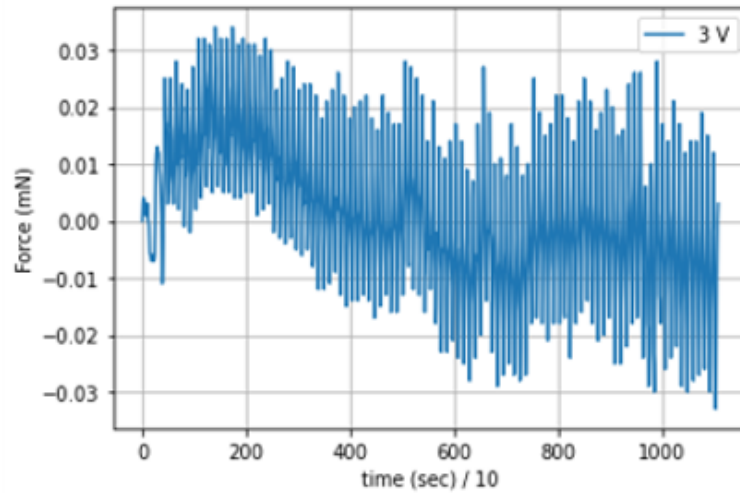


Figure 34: 9 mm IPMC output force signal.

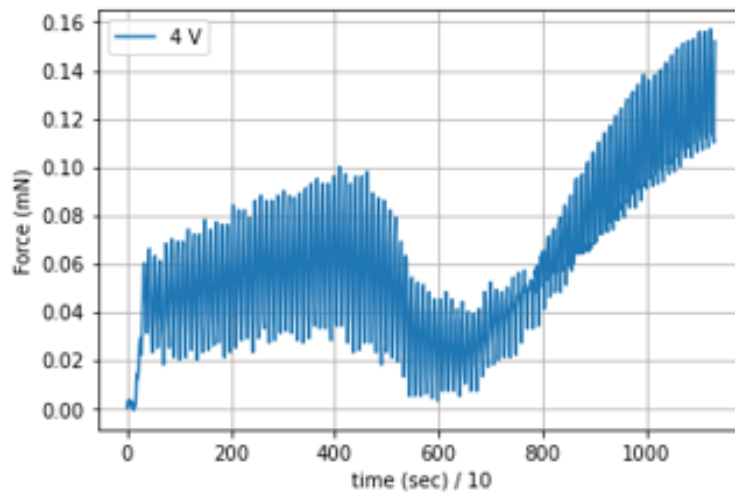


Figure 35: 11 mm IPMC output force signal.

Signal are presented in figure - 35 shows a different characteristic. It should be considered that the volume of water present on the surface will be higher due to larger surface area. The signal shift after 40 seconds is due

to inevitable electrolysis process. But the signal obtained for the first 40 seconds can include the presence of capillary forces.

Table 5: Force span for *9 mm* IPMC at different applied voltages.

Length (mm)	S.No.	Voltage (V)	Mean Force (mN)	Standard deviation
9	1.	2	0.0087	0.0035
	2.	2.5	0.0152	0.0031
	3.	3	0.0259	0.0056
	4.	3.5	0.0254	0.0043
	5.	4	0.0234	0.0083

Table 6: Peak Tip-force for *9 mm* IPMC at different applied voltages.

Length (mm)	S.No.	Voltage (V_{pp})	Mean Force (mN)	Standard deviation
9	1.	2	0.0368	0.0308
	2.	2.5	0.0255	0.0107
	3.	3	0.0553	0.0381
	4.	3.5	0.0456	0.0137
	5.	4	0.0434	0.0172

Table 7: Force span for *11 mm* IPMC at different applied voltages.

Length (mm)	S.No.	Voltage (V_{pp})	Mean Force (mN)	Standard deviation
11	1.	2	0.0075	0.0017
	2.	2.5	0.0120	0.0039
	3.	3	0.0227	0.0125
	4.	3.5	0.0275	0.0171
	5.	4	0.0384	0.0059

Figure-36 illustrates the force span generated by the IPMC samples at 1 Hz input driving frequency for different applied peak to peak voltages. The force values indicated are mean of means with standard deviation represented as error bars. Similarly, figure - 37 depicts the highest tip-force that

Table 8: Peak Tip-force for 11 mm IPMC at different applied voltages.

Length (mm)	S.No.	Voltage (V_{pp})	Mean Force (mN)	Standard deviation
11	1.	2	0.0168	0.0057
	2.	2.5	0.0266	0.0196
	3.	3	0.0476	0.0318
	4.	3.5	0.0277	0.0260
	5.	4	0.0318	0.0172

the IPMC samples can produce at this frequency. The latter is of high importance. It is the maximum tip force (or pushing force) which the samples can generate in transverse direction.

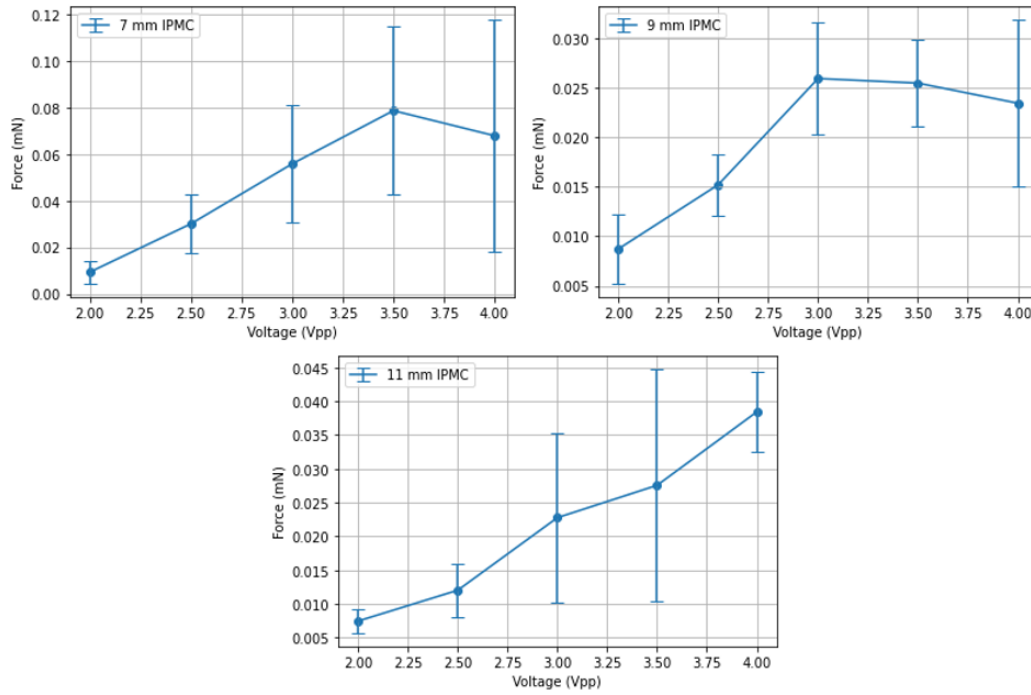


Figure 36: IPMC samples (7, 9 & 11 mm) force span versus applied V_{pp} plots.

Table 9: Force span of the IPMC samples at 1 Hz.

S.No.	Length (mm)	Maximum force (mN)
1.	7	0.078 at 3.5 V
2.	9	0.023 at 3 V
3.	11	0.038 at 4 V

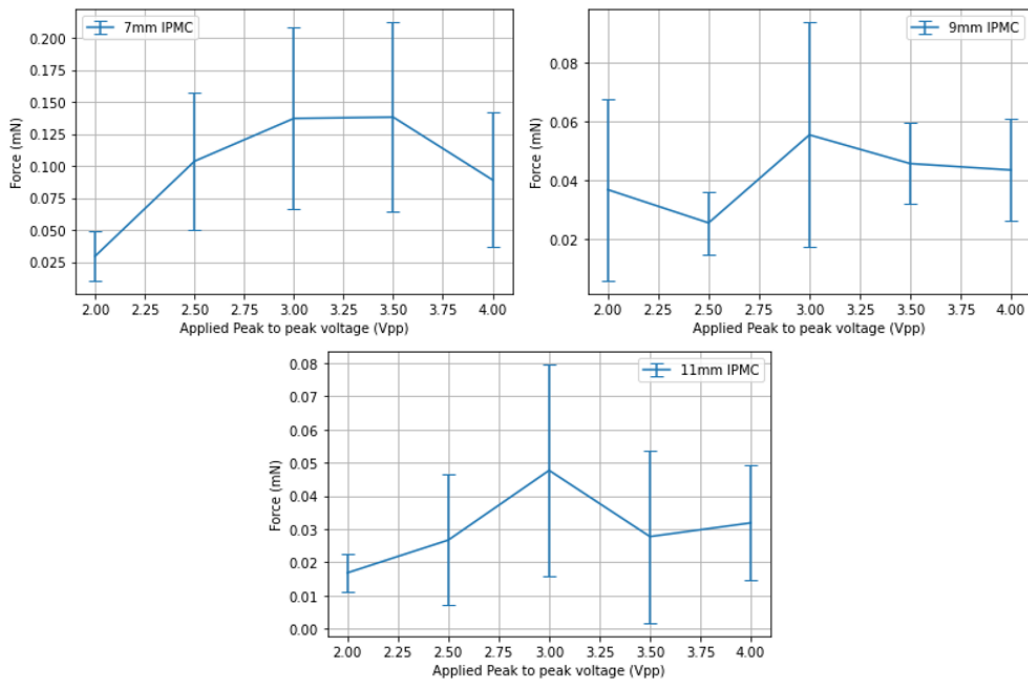


Figure 37: IPMC samples (7, 9 & 11 mm) peak tip-force versus applied V_{pp} plots.

Table 10: Peak Tip-force generated by the 7mm IPMC at 1 Hz.

S.No.	Length (mm)	Maximum force (mN)
1.	7	0.1380 at 3.5 V
2.	9	0.0553 at 3 V
3.	11	0.0476 at 3 V

7 mm IPMC generates the greatest peak tip-force of 0.138 mN and rest of the actuation experiments are focused on this IPMC sample. It is followed by the 9 mm IPMC and the 11 mm IPMC samples which produce 0.055 and 0.047 mN respectively. Table - 9 and 10 summarises the results depicted by figure-36 and 37 respectively.

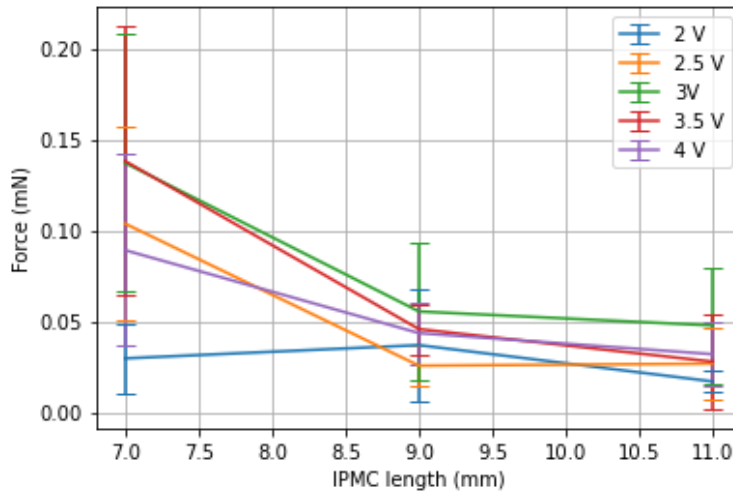


Figure 38: Peak tip-force versus IPMC length.

Figure - 38 depicts proportionality between the IPMC sample length and the peak tip-force applied by it. It can be observed that as the length increases, the peak force decreases.

• **0.1 Hz**

The results obtained for 0.1 Hz input driving frequency is presented in this part of the section. A distinction between the peak tip-force, force span and the pulling force is mentioned in chapter-3. A similar case is observed in the output force signal at this frequency as illustrated in figure - 39.

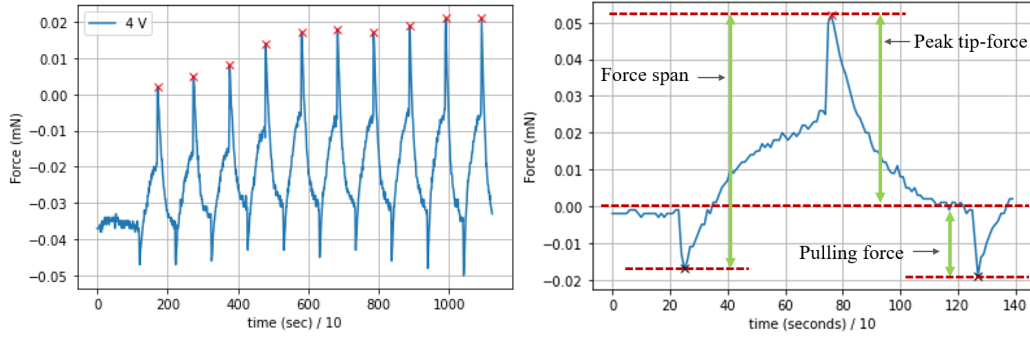


Figure 39: 7 mm IPMC force signal at 4V, 0.1 Hz. Left: Full signal. Right: 140 second window illustrating peak tip-force, force span and pulling force.

Forces acting on the load cell are more evident in the signal acquired at this driving frequency than others used in this project. This is because of broad pulse width at low frequencies. Examples of the force output signal obtained at every peak to peak voltage is shown in figure - 40. A total of three experiments per voltage were performed at this frequency. In addition to that, a few experiments were performed on the 9 and 11 mm samples to check the actuation signal. Figure - 41 and 42 represents their force signal.

It can be observed that the resultant signal characteristics (like the relaxation followed by sharp peak) are less apparent for the 9 and 11 mm samples than in the 7 mm IPMC. This is because a smaller sample has less surface area in contact with the sensor surface. It should be noted that the sample is wet when clamped in the setup and a liquid interface is formed between the IPMC and the load cell, as discussed before. The amount of solvent on the IPMC surface when extracted from the PBS solution cannot be controlled. Greater the sample surface area, more the solvent volume on its exterior. When a voltage at 0.1 Hz is applied, the IPMC bends quickly followed by the back relaxation process. Large volumes of solvent makes it difficult for

the 9 and 11 mm samples to deform when compared to the 7 mm one at the same voltage. Hence, they show a shorter sharp peak and a longer longer relaxation phenomenon.

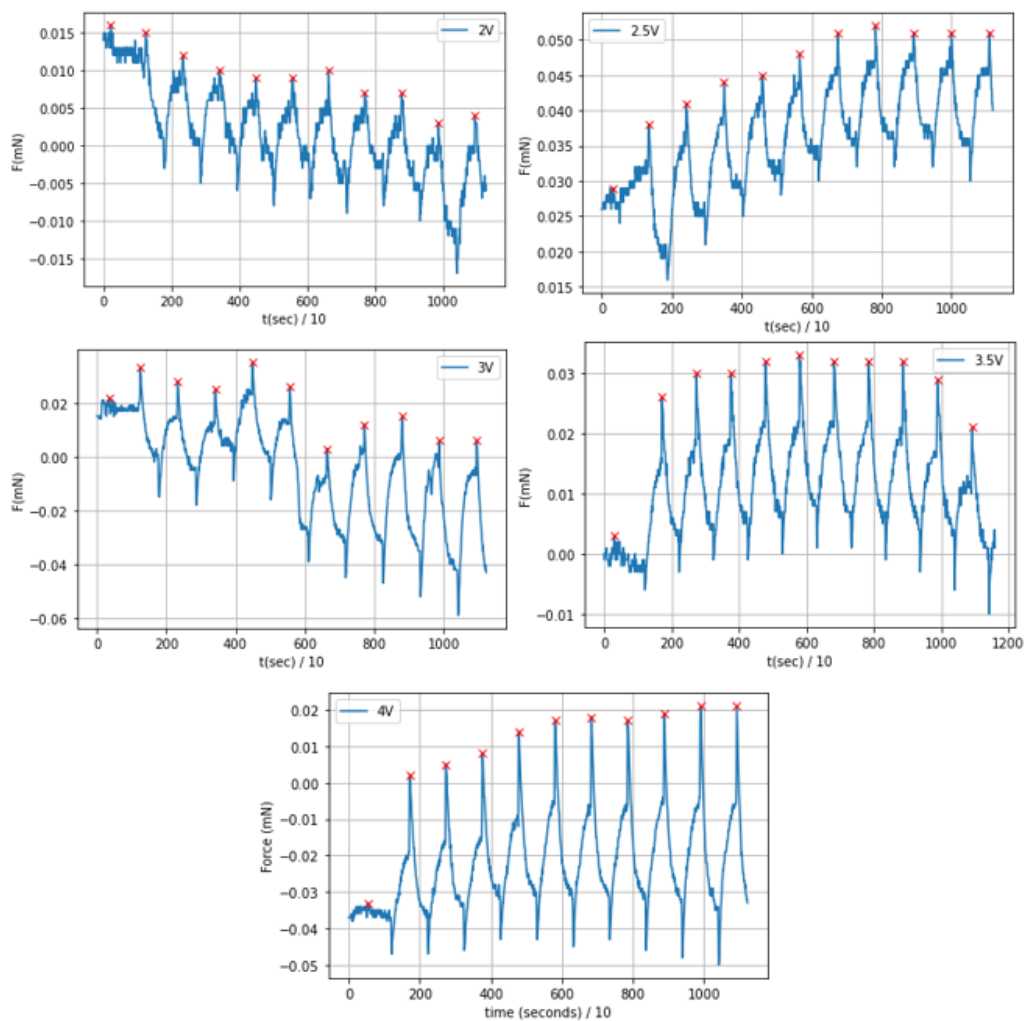


Figure 40: 7 mm IPMC force signal at different voltages.

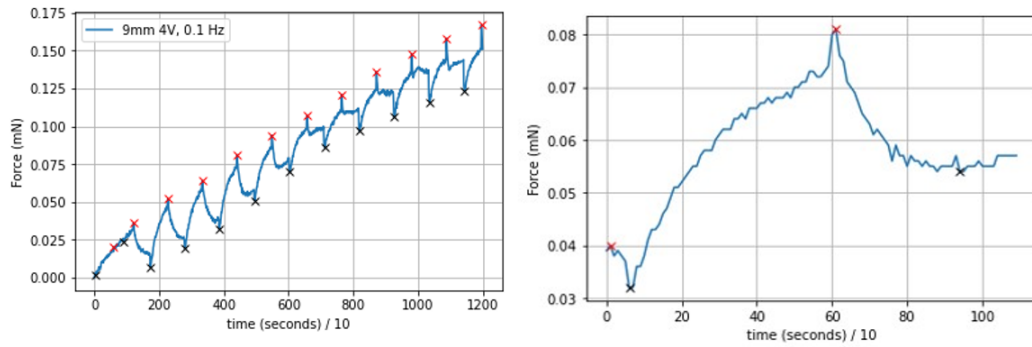


Figure 41: 9 mm IPMC force signal at 4 V.

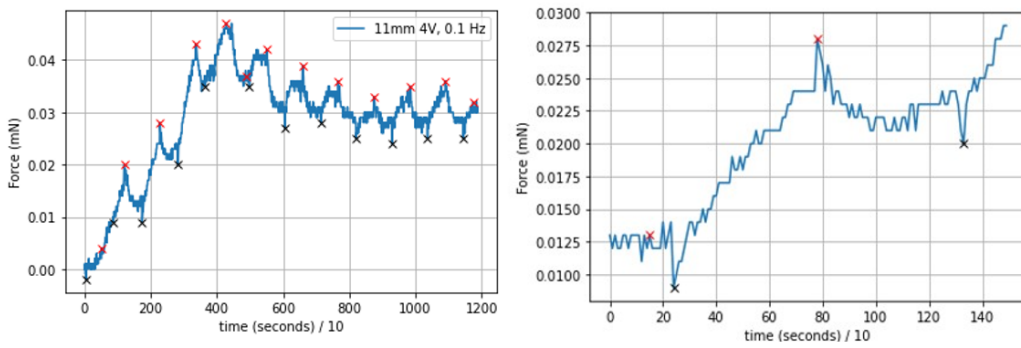


Figure 42: 11 mm IPMC force signal at 4 V.

Table 11: Force span results for the 7 mm IPMC at 0.1 Hz driving frequency.

Length (mm)	S.No.	Voltage (V)	Mean Force (mN)	Standard deviation
7	1.	2	0.0117	0.0043
	2.	2.5	0.0159	0.0044
	3.	3	0.0287	0.0186
	4.	3.5	0.0454	0.0130
	5.	4	0.0617	0.0117

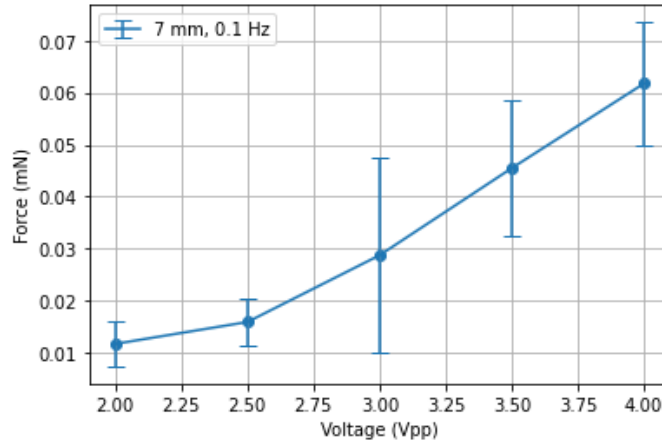


Figure 43: IPMC 7 mm force span versus applied V_{pp} .

The magnitude of force span increases linearly with applied peak to peak voltage because the mobile cations inside the iEAP can migrate further with increasing voltage. Also, the force span comprises of the peak tip-force and the pushing force. However, magnitude of the peak tip-force is the highest force in positive axis.

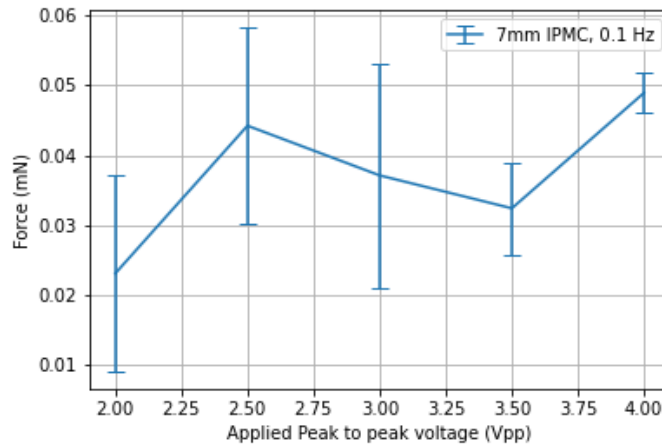


Figure 44: IPMC 7 mm peak Tip-force v/s V_{pp} plots.

Table 12: Peak tip-force results for the 7 mm IPMC at 0.1 Hz driving frequency.

Length (mm)	S.No.	Voltage (V)	Mean Force (mN)	Standard deviation
7	1.	2	0.0231	0.014
	2.	2.5	0.0442	0.014
	3.	3	0.0371	0.016
	4.	3.5	0.0324	0.0066
	5.	4	0.0489	0.0028

Force span plot for the 7 mm IPMC is presented in figure - 43. A maximum force span of 0.062 mN is generated at 4 V_{pp} (also shown in table-11). Similarly, the highest peak tip-force of 0.0489 mN is obtained at the same voltage (figure - 44 and table - 12).

• 5 Hz

The results for force generated at 5 Hz driving frequency is presented in this part of the section.

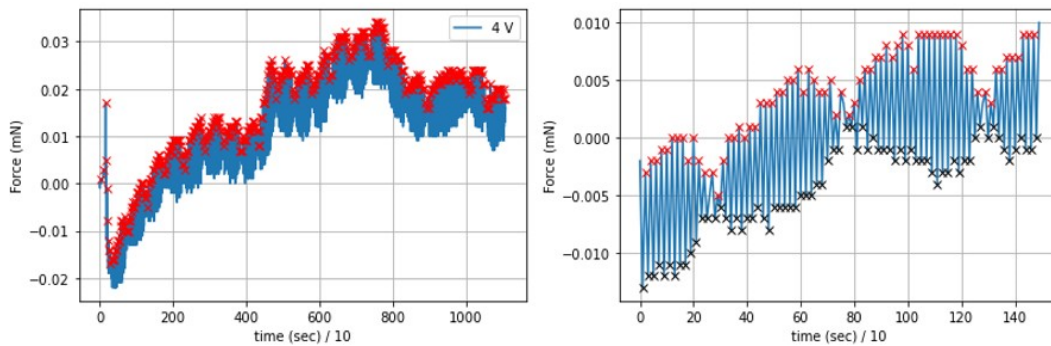


Figure 45: Example of 7 mm IPMC force signal at 5Hz. Left: Full signal, Right: 150 seconds window.

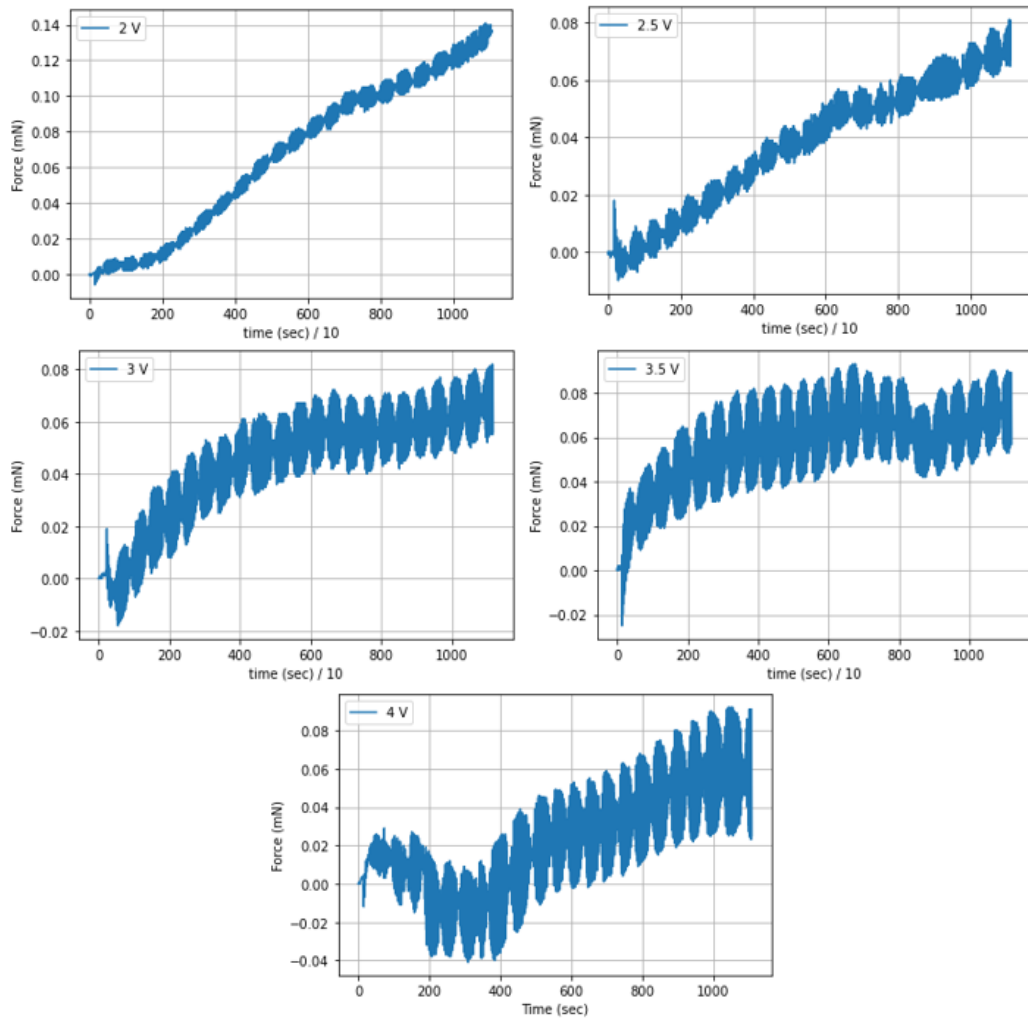


Figure 46: 7 mm IPMC force signal, 5 Hz at different V_{pp} .

A similar procedure as mentioned previously is used to determine the resultant peak tip-force and force span at this frequency. Peak tip-force corresponds to the red markers (signal peaks) with its magnitude on the force axis. Whereas, force span is the absolute difference of the signal peaks and valleys (denoted by red and black markers respectively). This is depicted in figure - 45. A few experiments were performed on the 9 and 11 mm sample to check the output signal characteristics, given in figure - 47 and 48.

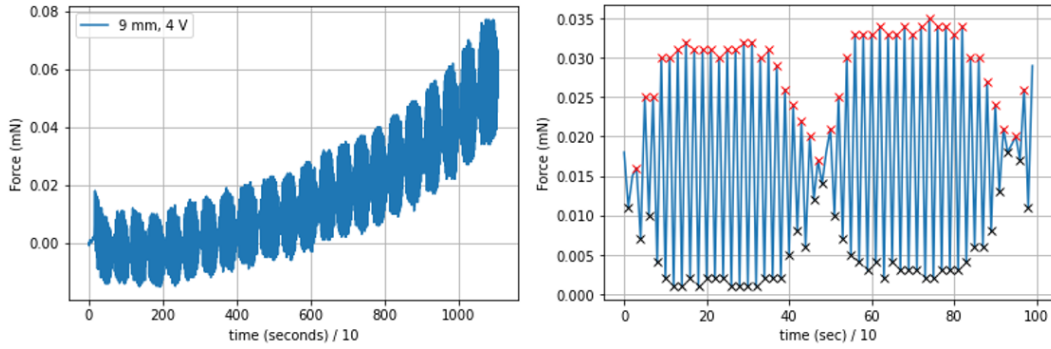


Figure 47: 9 mm IPMC force signal at $4 V_{pp}$.

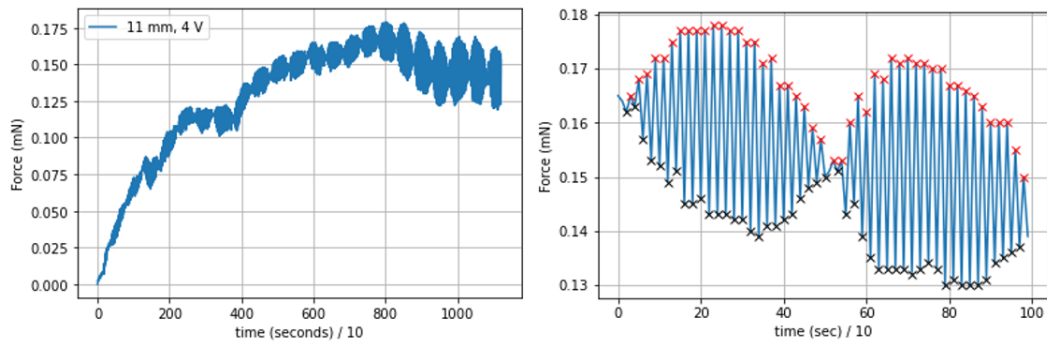


Figure 48: 11 mm IPMC force signal at $4 V_{pp}$.

Table 13: Force span results for the 7 mm IPMC at 5 Hz driving frequency.

Length (mm)	S.No.	Voltage (V)	Mean Force (mN)	Standard deviation
7	1.	2	0.0074	0.0010
	2.	2.5	0.0093	0.0022
	3.	3	0.0295	0.0066
	4.	3.5	0.0304	0.0044
	5.	4	0.0233	0.0158

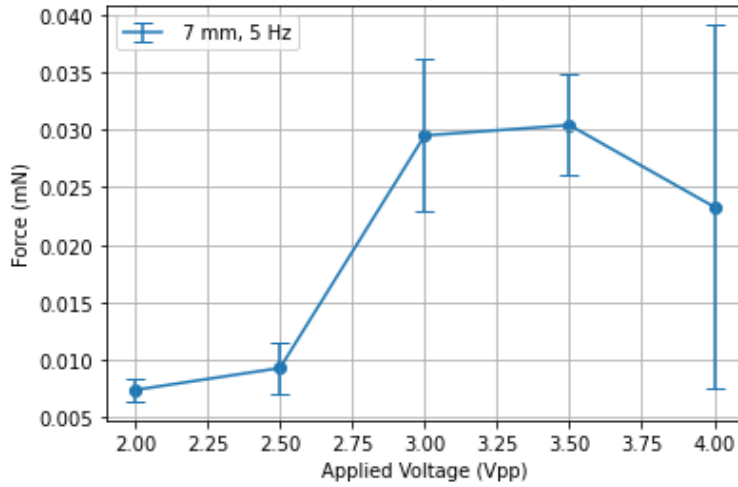


Figure 49: 7 mm IPMC force span versus applied V_{pp} .

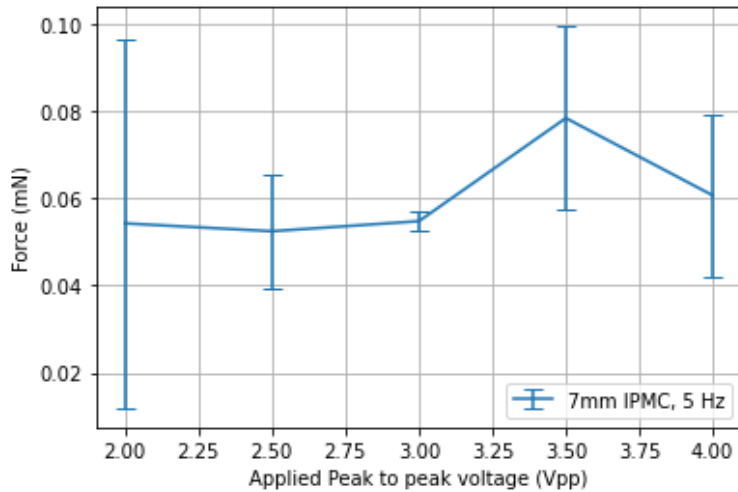


Figure 50: IPMC 7 mm peak tip-force vs V_{pp} plot.

The post processed force signal at this driving frequency represents an unexpected behaviour of the cantilever IPMC samples. Beat envelopes are formed and the time period of an envelope vary between 4 - 5.5 seconds.

A detailed analysis of these results is provided in the upcoming chapter. In this case, the highest peak tip-force of 0.078 mN and force span of 0.03

mN is generated by the 7 mm IPMC sample.

In figure - 46, the force span of at 2 and 2.5 V_{pp} is quite low. This is because due to high frequency the mobile cations do not get enough time to migrate effectively inside the electroactive polymer. In addition to that, low applied voltage is another factor.

Table 14: Peak tip-force results for the 7 mm IPMC at 5 Hz driving frequency.

Length (mm)	S.No.	Voltage (V)	Mean Force (mN)	Standard deviation
7	1.	2	0.0542	0.0423
	2.	2.5	0.0524	0.0131
	3.	3	0.0547	0.0023
	4.	3.5	0.0783	0.021
	5.	4	0.0606	0.0185

While the 9 mm sample result (figure - 49) show a high force span of the beat envelopes at 4 V_{pp} , at the same time it is really low for the 11 mm sample (figure - 50). But as the experiment proceeds, magnitude of the force span increases, specifically after 60 seconds. This can be regarded to subtle dehydration due to natural evaporation and electrolysis of solvent. IPMC cantilever gradually detaches from the sensor surface and force eventually increases.

It can be established from the results discussed in this section that the peak tip-force and force span magnitude of IPMC is strongly dependent on the input actuation frequency, applied peak to peak voltage and cantilever sample length. These parameters can affect the material at macro and microscopic level.

4.2 IPMC Tip-displacement

Tip-deflection (or displacement) measurements were performed on the same IPMC samples used for the force measurements. Total tip-displacement magnitude is the absolute difference of the signal peak (in red marks) and the signal valley (in black). This section is categorized based on the driving frequency.

• 1 Hz

Total tip-displacement recorded and analyzed for the 1 Hz driving frequency is presented in this section. Figure - 51 illustrates the determination method used to obtain results for this measurement. It can also be noticed that the signal peaks are more sharp edged compared to that in the force measurements. This is because of the absence of contact surface under the IPMC samples.

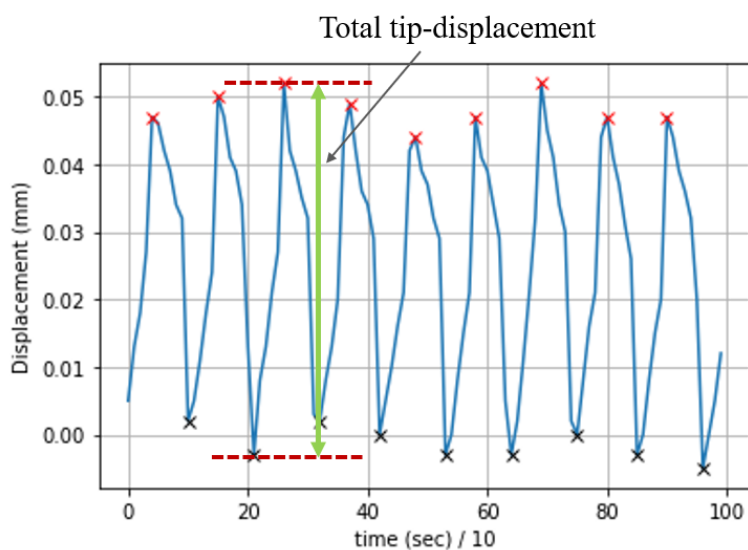


Figure 51: Example of the total tip-displacement calculation.

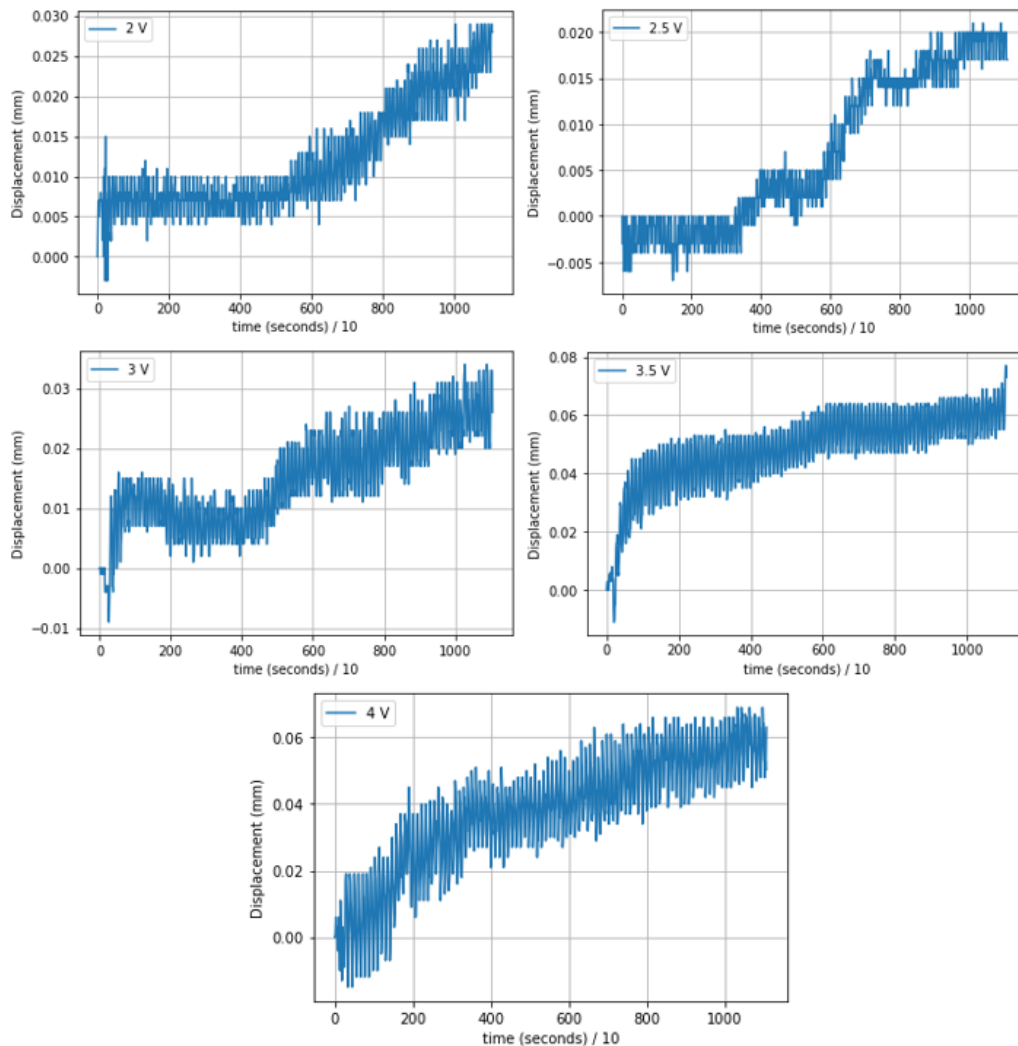


Figure 52: 7 mm IPMC tip-deflection signal at different peak to peak voltages.

A persistent characteristic which can be noticed in all the tip-deflection results in figure - 52 is the shift displacement signal. This corresponds to change in the IPMC tip position over time. As the experiment progresses, the IPMC starts to dehydrate and bend downwards. Figure - 53 illustrates this feature. When the experiment is stopped and the IPMC is removed from its clamp, the bending geometry persists until it is hydrated again. This is

because IPMC tends to bend naturally upon dehydration as the polymer chains start to curl. When hydrated again, it regains its cantilever geometry. It is suggested to keep IPMC hydrated at all times for its efficient use. The amount of solvent present inside the material majorly determines properties like the output tip force and displacement.

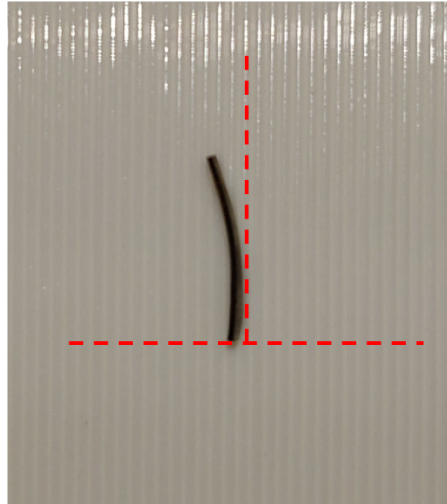


Figure 53: Side view of the bent 7mm IPMC sample after displacement measurements for 1200 seconds at $4 V_{pp}$.

The total tip-displacement results for the 7 mm sample is given in table - 15. This sample attains a highest displacement of 0.035 mm at $4 V_{pp}$.

Table 15: Total Tip-deflection results for the 7 mm IPMC at 1 Hz driving frequency.

Length (mm)	S.No.	Voltage (V)	Mean displacement (mm)	Standard deviation
7	1.	2	0.0046	0.00065
	2.	2.5	0.005	0.0013
	3.	3	0.0076	0.0016
	4.	3.5	0.0173	0.0071
	5.	4	0.0349	0.015

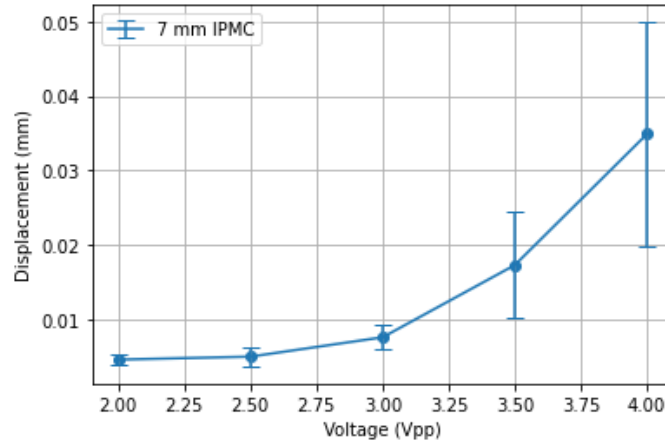


Figure 54: IPMC 7 mm tip-force vs V_{pp} plot.

As seen from figure - 54, the displacement is directly proportional to the voltage applied. Hence, higher the input voltage, larger the tip deflection.

• **0.1 Hz**

The 7 mm IPMC was tested for the tip-deflection experiments at 0.1 Hz. A total of 5 experiments were performed for this part at 4 V_{pp} . A mean tip-displacement of 0.2904 mm with a standard deviation of 0.019 was obtained. Plot for the same is given in figure-55.

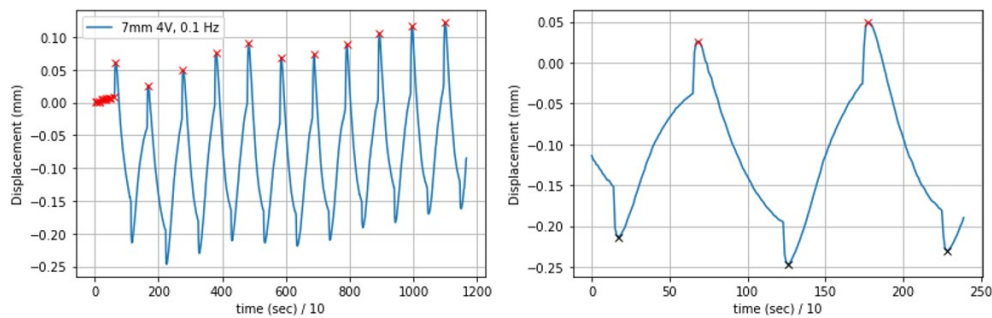


Figure 55: IPMC 7 mm tip-deflection signal at 0.1 Hz using optoNCTD 1750.

It can be observed from figure - 55, 56 and 57 that the samples undergoes a smooth back relaxation process. As the displacement goes below zero (on

the x-axis), it is bending towards the displacement sensor (upward direction) and when the displacement value is over zero, it is deforming downwards (away from the sensor). Ideally, the IPMC sample when clamped should be horizontally straight and upon applied voltage it should produce an actuating signal centered around zero. In reality, it bends due to presence of water on its surface. This explains the displacement signal obtained in fig - 56 and 57. In case of figure - 55, the IPMC is bend when clamped in the setup. The displacement signal is centered approximately around -0.075. This shows that the volume of water present on its surface has no effect on its initial position since the active actuating part is only 5 mm.

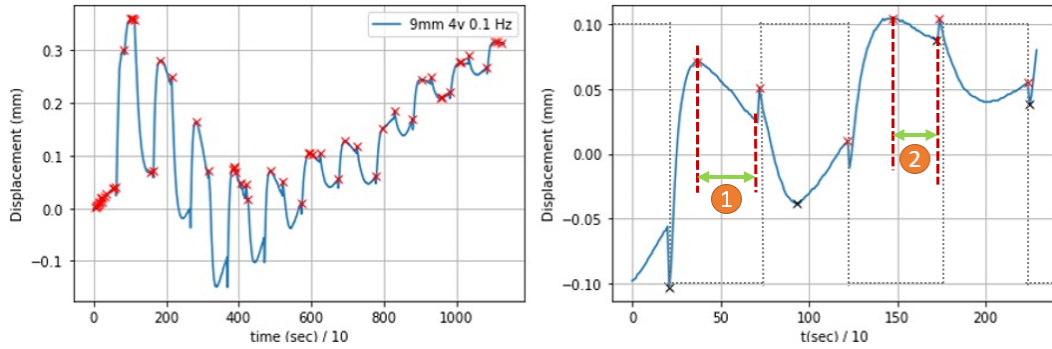


Figure 56: IPMC 9 mm tip-deflection signal at 0.1 Hz using optoNCTD 1750.

In figure - 56 it is seen that upon applied voltage the IPMC undergoes a quick bending deformation towards the anode followed by another bending response (naming it as secondary bending for convenience) (compared to fig - 56 and 58) at the starting point of the pulse width. This is due to large volumes of water present on its surface which bends the material because of its weight. Due to this reason the conventional back relaxation curve in the signal is missing. Then, some smooth relaxation can also be observed between a certain time period (indicated as 1 and 2). This occurs because the free water molecules are in the process of migrating inside the polymer layer to attain the equilibrium state causing relaxation in the opposite direction.

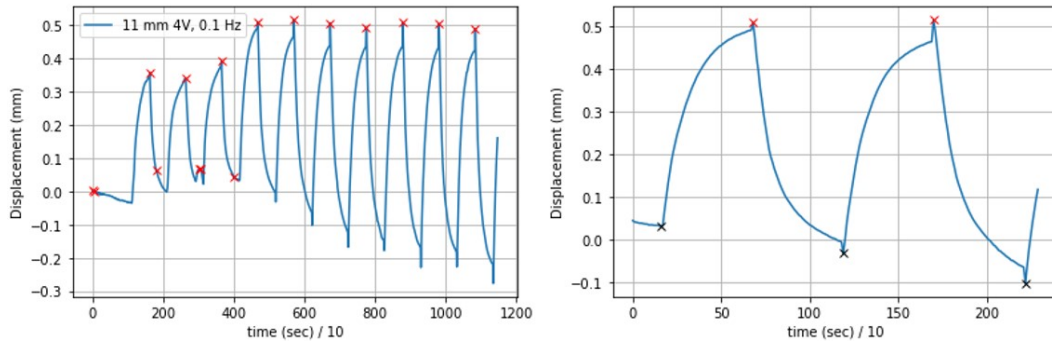


Figure 57: IPMC 11 mm tip-deflection signal at 0.1 Hz using optoNCTD 1750.

In case of figure - 57, the 11 mm IPMC sample undergoes a smooth back relaxation process. However, the sharp peaks which occurs when polarity of the input square wave changes is missing in the displacement signal. It is because this sample tip bends more compared the 7 and 9 mm IPMC during the back relaxation process. This bending shifts the laser spot at the IPMC tip edge leading to loss of displacement signal at the edge of pulse width.

The characteristic signal at 0.1 Hz driving frequency for this measurement is different than that of force measurements as there is no surface present under the IPMC samples to restrict their bending deformation.

• 5 Hz

Lastly, the tip-displacement measurements were performed at 5 Hz frequency for all the IPMC specimens at $4 V_{pp}$. Results of the experiments are given below:

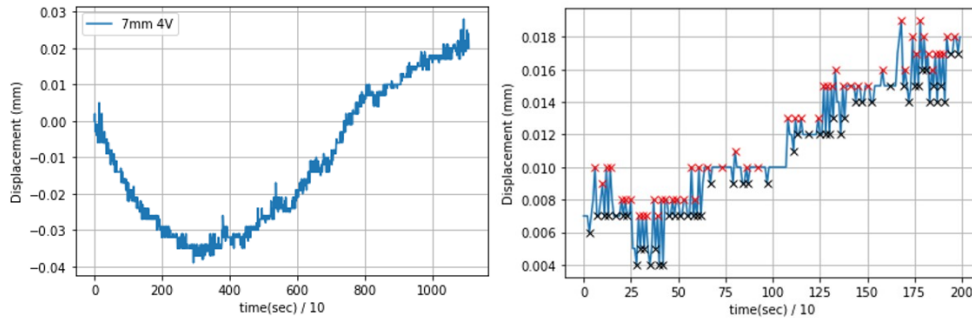


Figure 58: IPMC 7 mm tip-deflection at 5 Hz using optoNCTD 1750.

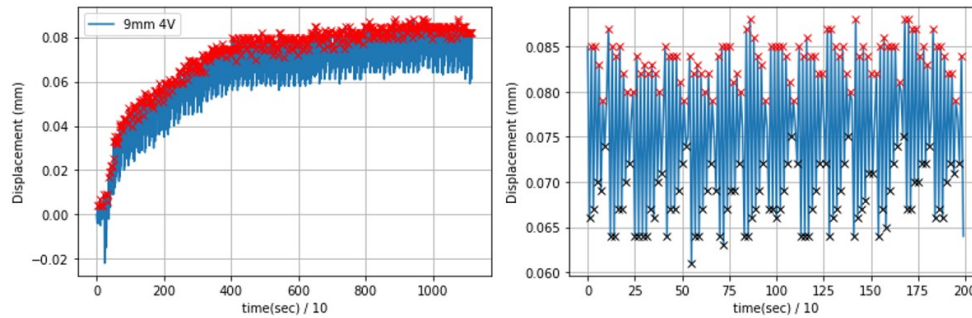


Figure 59: IPMC 9 mm tip-deflection at 5 Hz using optoNCTD 1750.

It can be observed that the signal in figure - 58 and 60 is affected due to low resolution of the displacement sensor as the tip-displacement decreases with increase in frequency. For the 9 mm sample (figure - 59), beat envelopes are obtained. This is similar to the load cell results which were acquired at this input driving frequency. It is discussed in the upcoming chapter in detail.

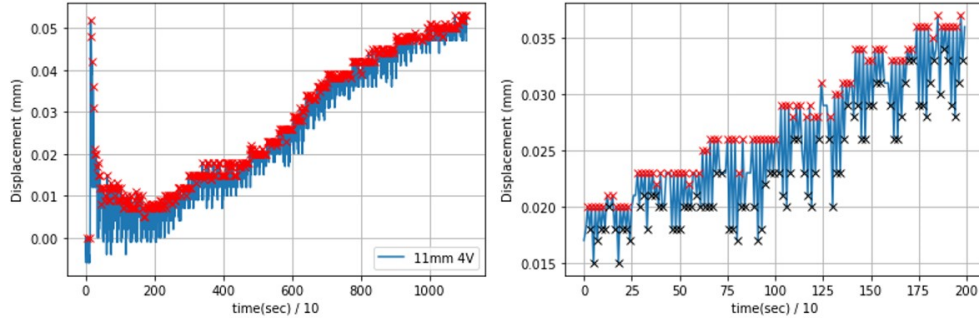


Figure 60: IPMC 11 mm tip-deflection at 5 Hz using optoNCTD 1750.

4.3 IPMC density approximation

As discussed in section - 3.1, density of the mentioned IPMC sample was measured using Archimedes principle and the equation used for the calculation. Table below gives an overview of the relevant results obtained using Archimedes experiment.

Table 16: Density values using Archimedes Principle experiment.

S.No.	Density (g/cc)
1.	14.15
2.	9.86
3.	13.59
4.	19.91
5.	26.81
6.	32.01

It can be seen from table - 16 that the density values are higher than the density range reported in [40]. During the experiment there were few other density values obtained which were very high and are excluded. This broad

difference in the IPMC density values is related to very quick natural dehydration process. The most challenging part of the experiment is measuring the IPMC sample weight in air, which lead to many inconsistent results for the consecutive experiments.

A theoretical process for the composite density approximation was also taken into account. Steps to calculate the density are as follows:

- Find the density of individual elements in the composite.
- Calculate their relative contribution to the material.
- Then multiply the density of each element to their contribution in the material and sum all the values.

The density of Nafion 117 is 1.58 g/cc and that of platinum is 21.45 g/cc. The nafion used is 180 μm and two platinum layers are 10 μm each. Hence using these values, the density of the in-house manufactured IPMC was approximated to be *5.5 g/cc*.

4.4 IPMC endurance test

IPMC is known to have a good actuation capability. An experiment to verify the longevity of the IPMC actuation at 4 volt peak to peak using the laser displacement sensor was performed. A similar setup was used as for the tip-deflection experiments. The IPMC was actuated at 1 Hz until it cannot undergo further bending deformation. Results are given below:

The crucial observation for this experiment is that the IPMC did not stop actuating even after 6000 seconds, in the case of 9 and 11 mm samples. For the 7 mm sample it can be observed that after 3000 seconds there is formation of flat steps which can be related to extremely small deflection that cannot be detected by the sensor or no actuation at all. However, due to time constraints the experiment has to be terminated.

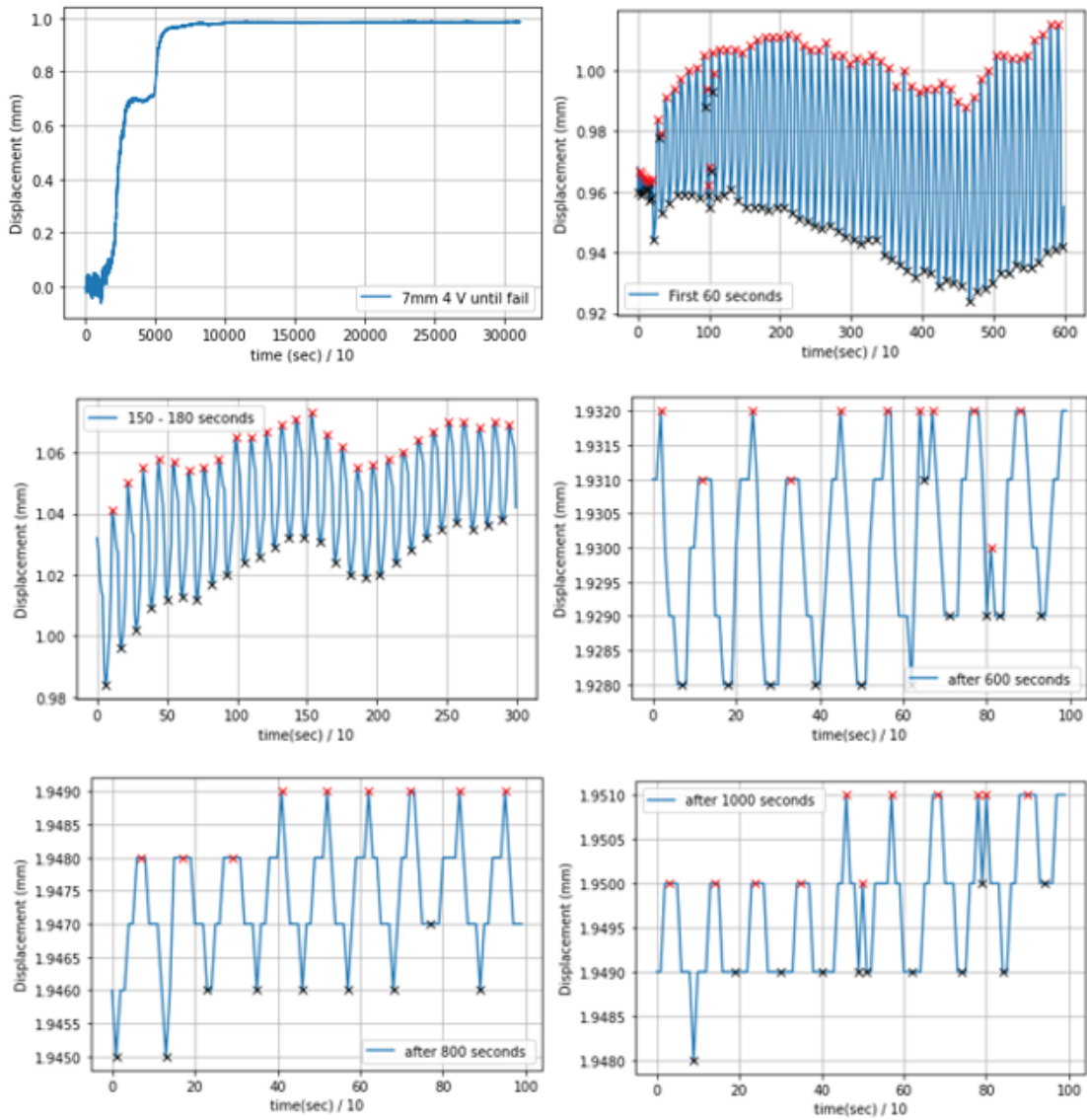


Figure 61: IPMC 7 mm endurance test.

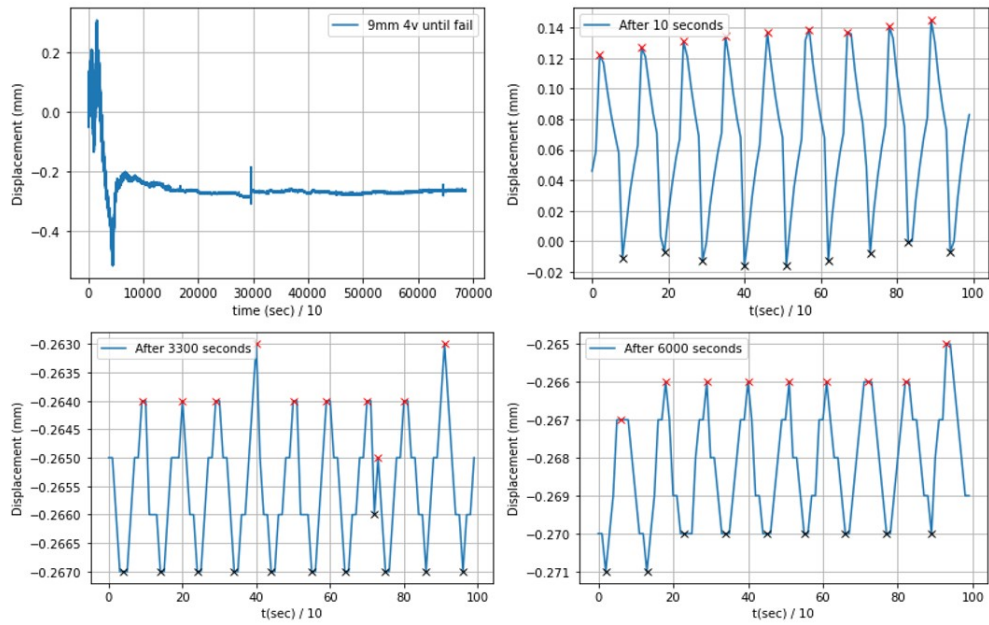


Figure 62: IPMC 9 mm endurance test.

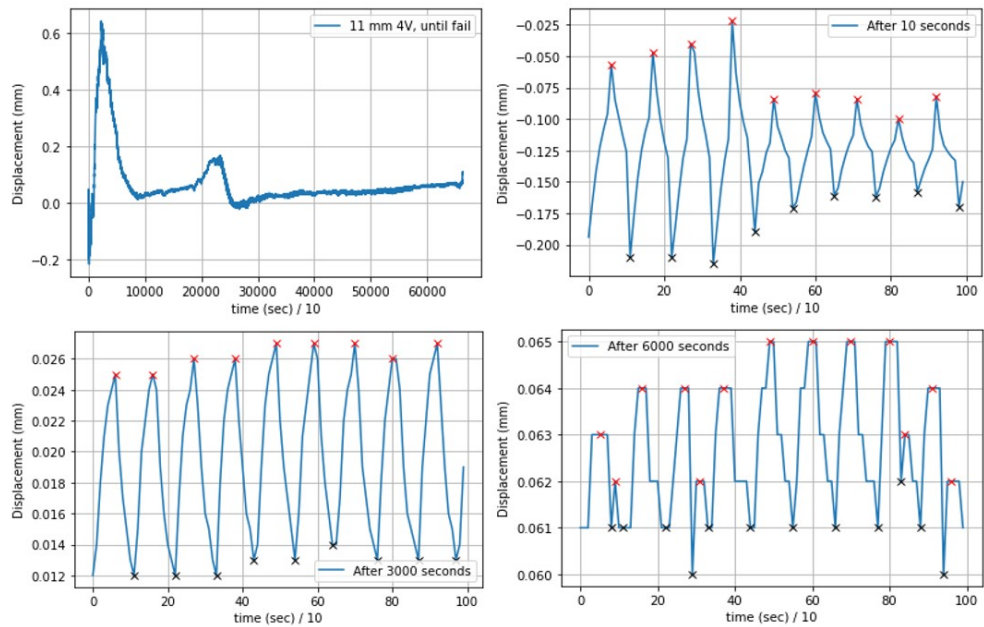


Figure 63: IPMC 11 mm endurance test.

- The displacement of the 7 mm sample decreased from ~ 0.04 mm at 10 seconds to less than 0.002 mm after 3000 seconds.
- In case of the 9 mm sample, reduction is from ~ 0.12 mm at 10 seconds to approximately 0.004 mm after 6000 seconds.
- Finally, for the 11 mm sample the displacement decreased from ~ 0.22 mm in the first 10 seconds to ~ 0.0045 mm after 6000 seconds.

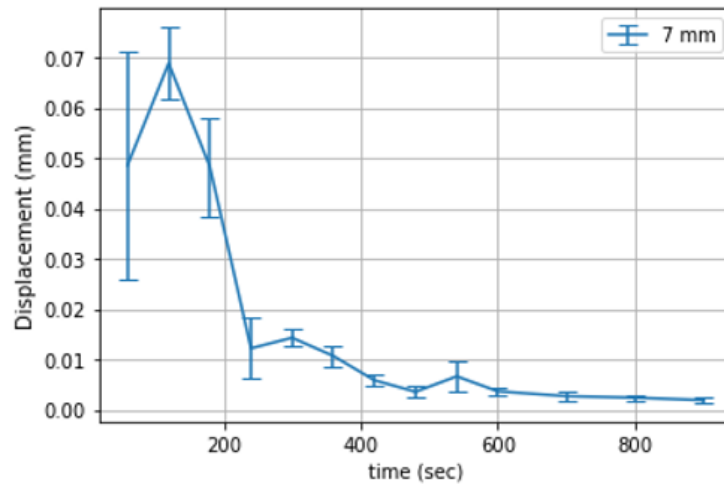


Figure 64: IPMC 7 mm endurance test per 60 seconds.

Figure - 64 presents the change in displacement for the endurance test per 60 seconds until 600 seconds, then per 100 seconds until 900 seconds. The mean value of the displacement is represented on the x-axis. The reduction in displacement after 120 seconds (peak) is due to loss of hydration level inside the sample. After 600 seconds the result is close to minimum resolution of the sensor, which is $2 \mu m$.

5 Discussion

• *Tip - Force experiments*

Tip-force generated by the IPMC samples of length 7, 9 and 11 mm was assessed using a load cell as mentioned in the previous chapter. The experimental setup was 3D printed and load cell was fixed in the specified location. Dimensions of the setup were calculated carefully such that after clamping the cantilever IPMC sample (2 mm between the gold electrodes), its tip hits the sensor surface properly to obtain reliable results. The force versus time and force versus applied voltage plots for different lengths were presented.

1. *At 1 Hertz*

Figure - 33, 34 and 35 show that the IPMC actuation signal to calculate the tip force directly corresponds to the input driving frequency of the square waveform i.e., 9 - 10 peaks are obtained in a 10 second signal window. In addition to that, numerous small peaks of force span 0.001 to 0.003 mN were also observed within the signal at low voltages (typically 2 and 2.5 V_{pp}). These peaks can be seen in the middle and/or lower section of the plot, figure-65. Occurrence of these peaks can be regarded to low sensor resolution and noise in the signal. The figure - 65 portrays the actuation behaviour at 2 and 4 V_{pp} for this comparison.

Small relaxations at 1 Hz driving frequency are more dominant for small applied voltages than at a higher voltage. This phenomenon is directly related to mobility of the cations bonded to solvent molecules inside the material. As per the actuation mechanism of the IPMC, material swells at the cathode due to cation migration upon an applied voltage. This leads to development of the local mechanical strains on the composite material and bending occurs. [50] More the number of cations migrate inside the material, stronger the actuation and sharper the signal. Strong actuation is directly related to intensity of the applied voltage. Relaxation is observed for both, low and high voltages during the stable pulse region (as shown by colored

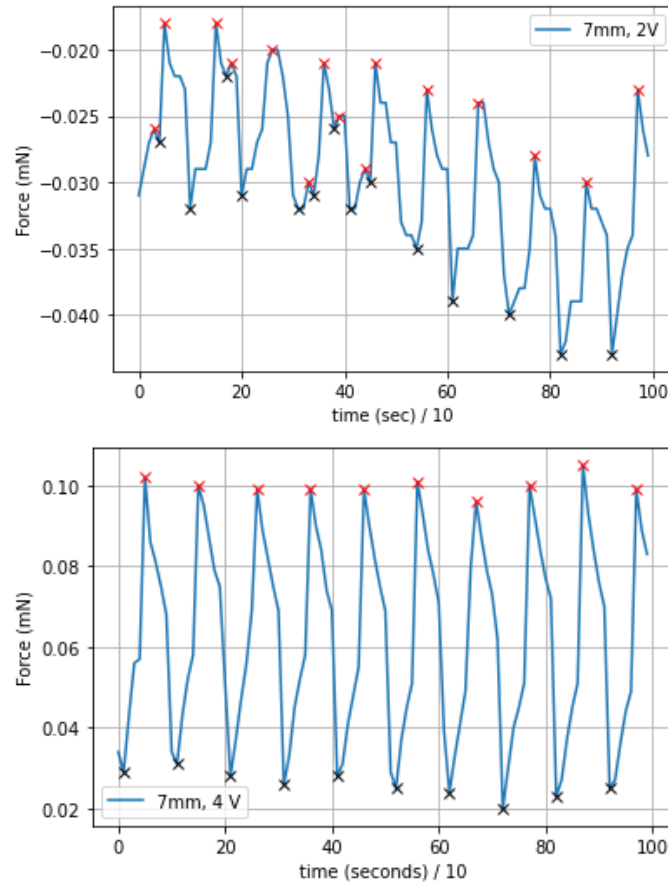


Figure 65: 7 mm IPMC windows between 20 - 30 seconds at 2 and 4 V between

arrows in figure - 66). The pulse width depends on the input frequency, so a short relaxation period is result of a high frequency. Hence the relaxation of the IPMC depends on the driving frequency of the applied voltage.

The peak tip-force and force span results represented in figure - 36 and 37 are the mean of means calculated for all the experiments performed at each voltage. It was observed that the mean force values obtained for the measurements have high standard deviation.

This change in value from one experiment to the other can be explained

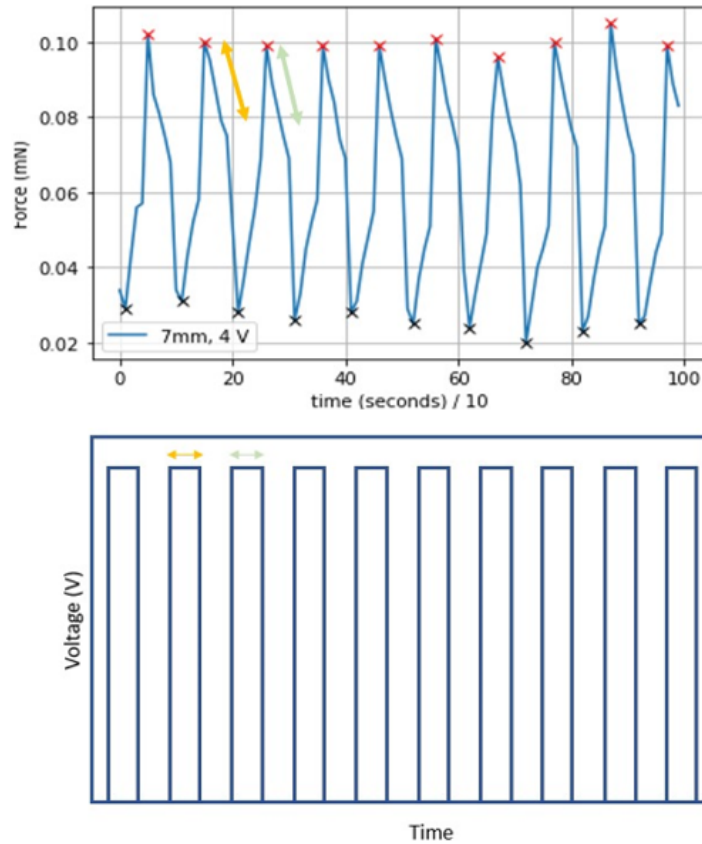


Figure 66: Depiction of IPMC actuation corresponding to the applied peak to peak voltage (schematic of the GUI)

by two phenomenon:

1. Capacitance behaviour
2. Trapped ions within the sulfonate clusters due to dehydration

The electronics used for actuating IPMC includes a Arduino nano. It is unable to produce negative voltage due to which the MATLAB GUI is centered around 2.5 V. This results in accumulation of electrons onto the electrode surface. Platinum layers of 10 μm each are deposited on both sides of the IPMC during its manufacturing process. This is done via electroless deposition technique. There is presence of large number of platinum nano particles with high roughness after the deposition process, which can trap

the electrons. Hence, the pre-accumulated charge provide a different result for the successive experiment. To counter this issue a set of experiments were performed by introducing a few reset steps. It was experimentally proven for different voltages that including these reset steps can reduce the standard deviation for an experiment by a factor of 10.

The experimental steps with the reset are as follows:

- Clamp the IPMC between gold electrodes and actuate for the desired measurement.
- Ground the electrode wires after the experiment is terminated. This is done to discharge the electrons accumulated on the electrode. This resolves the capacitance effect.
- Dip the IPMC back into the ion exchange solution for ~ 10 minutes for the material to regain its ionic concentration.
- Post clamping the IPMC between the electrodes for the next experiment, ground the electrode wires again and then perform the desired experiment.

Table - 17 show the decrease in deviation for the 7 mm sample actuated at 3.5 and 4 V_{pp} , 1 Hz.

Table 17: Data variation to reduce deviation using the reset procedure

Voltage (V_{pp})	Experiment No.	Without Reset		With Reset	
		Mean	Standard deviation	Mean	Standard deviation
4	1.	0.099	0.071	0.053	0.014
	2.	0.166	0.068	0.047	0.007
	3.	0.106	0.044	0.041	0.006
	4.	0.078	0.038	0.040	0.003
	5.	0.050	0.016	0.044	0.004
	6.	0.043	0.011	0.041	0.007
3.5	1.	0.121	0.037	0.067	0.005
	2.	0.057	0.015	0.095	0.009
	3.	0.071	0.029	0.088	0.015
	4.	0.085	0.016	0.106	0.008
	5.	0.113	0.014	0.074	0.006

Experimental procedure including the reset steps were able to reduce the deviation within one experiment and between consecutive experiments at 4 V_{pp} successfully. However, deviation between the consecutive experiments at 3.5 V_{pp} is still quite high. To explain this, phenomenon of trapped migrating ions has to be considered along with the reset process.

As mentioned in section-2.6, sulfonate clusters are connected together via nanometer thick pathways that provides a passage to the cations and water molecules inside the material. The cluster size is directly proportional to the hydration levels inside the material. As the experiment proceeds, IPMC starts to dehydrate due to electrolysis and natural evaporation. When the experiment is terminated, the IPMC sample surface is dry. Evidence of electrolysis marks can be seen in figure - 24. IPMC is not completely dry internally as the actuation endurance test suggests that the 7 mm sample can actuate at least for 800 seconds in dry environment.

The migrating ions are trapped during their movement at different locations inside the polymer network cluster. When the same sample is used for the next measurement after a short period of time (like 10 min in this case), the trapped ions start moving from their initially confined position. This leads to a big change in the resultant values between two measurements. Hence a higher deviation.

Actuation force generated is related to the IPMC thickness, length and the voltage applied. A long IPMC will generate higher displacement but a lower tip-force. However in case of a shorter IPMC, it will produce high tip-force and a lower displacement. This was experimentally determined in this project. Figure - 36 represents that. *kim et all* [37] presented that the tip force generated (also called the blocking force) is directly proportional to the width and square of the actuator thickness, and inversely proportional to the actuator length. It is given the by following formula: [83]

$$F = C_1 \times \frac{w.t^2}{L} [gf]$$

where, C_1 - Constant; w, t, L are the width, thickness and length respectively.

2. At 0.1 Hertz

Figure - 40, 41 and 42 show the force signal response of the IPMC samples at 0.1 Hz driving frequency. The relaxation process at 1 Hz was discussed previously and was seen to be extremely small. However, that is not the case at lower frequencies. The actuation plots obtained at 0.1 Hz depict that the relaxation time increases as the driving frequency decreases. A similar characteristic signal is obtained for all the IPMC samples.

In figure - 67, an input square wave signal is compared with the acquired post processed signal. The stable pulse period (1 to 2) corresponds to a slow back relaxation of the cantilever sample. The mobile ions along with water molecules which have migrated towards the cathode move back to their equilibrium position inside the polymer to neutralize the ion concentration imbalance. As the pulse width reaches the point of trailing edge (point 2).

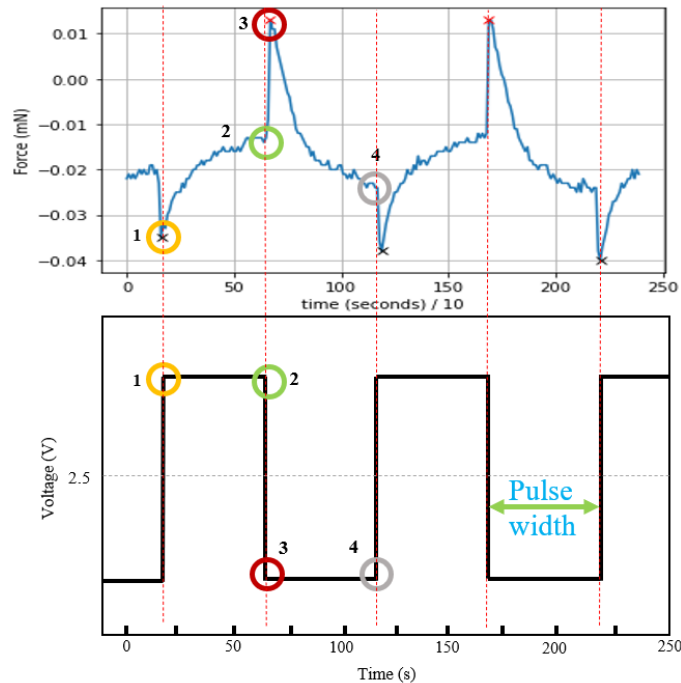


Figure 67: Correlation of acquired signal (top) to the input actuation signal schematic (bottom).

IPMC instantaneously deforms hitting the sensor surface. This results in a very sharp peak (top figure: 2 to 3). Following this, the mobile ions are proceeding back inside the polymer membrane (back relaxation), point of fall in the pulse is reached which accelerates the mobile ions towards the anode. When the next stable pulse region is attained (3 to 4) the phenomenon of back relaxation is achieved again by the IPMC sample. This is observed from point 3 to 4. Similarly, the ions and water molecules move back to neutralize the ion imbalance created by their migration. There are two components to this deformation process; a quick bending accompanied by a slow back relaxation. It can also be seen that the relaxation time is approximately 5 seconds each which corresponds to the input driving frequency.

The back relaxation of Nafion is a very complex and less understood process. It highly depends on the backbone polymer along with the ion type and its content present inside the material.

Porfiri et al [42] have mentioned in their research that the bending response is dependent on the mobile cations. The small cations like Li^+ , Na^+ or K^+ induce a quick response to applied voltage and a slow back relaxation, whereas larger cations induce a quick back relaxation. The mobile cations present in the IPMC specimens are Na^+ ions since the ionic solvent is sodium rich. Hence, this specifically explains the post processed force signal behaviour at 0.1 Hz driving frequency.

3. *At 5 Hertz*

Figure - 46, 47 and 48 represents force signal of the IPMC specimens at 5 Hz driving frequency. The relaxation and actuation behavior at 1 and 0.1 Hz has been discussed at micro and macroscopic scale. The force signal obtained at 5 Hz is quite different from the other two. Post processed signal depicts very sharp peaks formed in segments of specific time frame. The results obtained are quite unexpected.

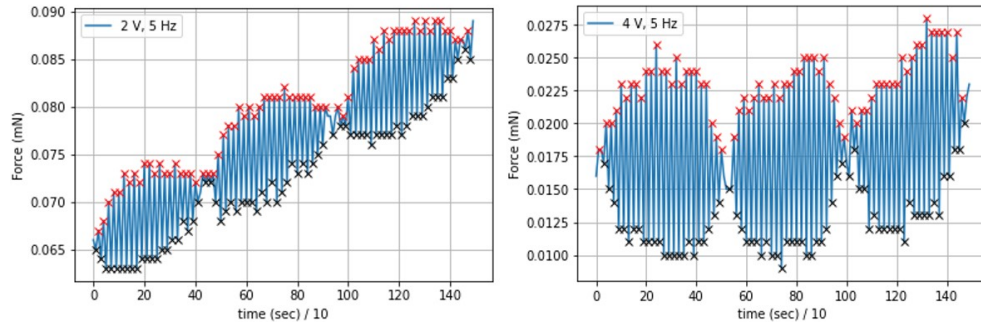


Figure 68: Comparison of 2 and 4 V force signal at 5 Hz for the 7 mm IPMC.

Figure - 68 depicts a comparison of the signal acquired at 2 and 4 V_{pp} . The data window depicted is of 15 seconds each. Three segments of approximately 5 seconds each are obtained in the window. These segments are similar to a beating frequency envelope. Beat envelope is visualized when waves of two similar or very close frequencies interfere at the same point in space and show periodic increase and decrease in signal.[54] This phenomenon was observed for all the measurements at this frequency (different peak to peak voltages at different IPMC lengths measured). The input driving frequency is 5 Hz (it was revealed by the FFT that the input driving frequency is actually 4.9 Hz. This is discussed later.) and the other unknown frequency should be somewhere close to this range. The beating frequency equation is stated below: [54]

$$f_b = |f_2 - f_1|$$

where, f_b - Beating frequency (0.2 Hz), f_1 - first frequency (Driving frequency = 4.9 Hz) and f_2 - second frequency

Using the above mentioned equation it can be estimated that the second frequency is in the range of 4.7 - 5.1 Hz. It is important to understand the origin of this second unknown frequency.

Possible causes are:

- Free mobile ions which are migrating inside the material upon the application of applied voltage. However, the resonance frequency of mobile

ions is expected to be extremely high and cannot cause formation of beat envelope.

- Liquid bridge resonance. IPMC when removed from PBS solution to clamp between the electrodes. This leads to formation of a water interface layer between the sensor surface and the IPMC sample. But it should be considered that sample dehydrates during the actuation process due to which the water interface disappears and post experiment, the IPMC sample surface is dry. Occurrence of electrolysis is inevitable when a voltage higher than 1.23 Volts is applied to the wet IPMC. [55][56] The minimum actuation voltage for the experiments is 2 Volts.

Tip-force and tip-displacement measurements were performed simultaneously. The results obtained show a correlation between the number of peaks and its shape at 1 Hz. Also, peaks obtained for both measurements match the input driving frequency (As it had already been discussed). The results are given in Appendix - III. The displacement signal at 5 Hz cannot be relied upon due to low resolution of the sensor.

- Vibration of sulfonate clusters inside the Nafion polymer. Nafion has a long polymer backbone to which the ion clusters are attached via per-fluoroethylene side chains. When mobile ions migrate at a high frequency of 5 Hz, they can cause the vibration of the clusters inside the polymer.
- Another cause could be natural frequency of the cantilever IPMC. It might be that natural frequency of the cantilever is attained when the IPMC is actuated at 5 Hz driving frequency.
- Lastly, an important parameter that should be taken into account is sampling rate of the sensors (load cell and displacement sensor).

In order to record the impulse response in time domain of the cantilever sample an experimental setup was constructed. The setup is shown in figure - 69. IPMC sample was clamped and laser displacement sensor was held such that the laser hits the tip of the IPMC. The fundamental motive is to vibrate the sample by different means in order observe the cantilever resonance frequency.

Methods tried are as follows:

- First, IPMC sample was clamped and a drop of PBS was made to free fall on its tip using a pipette . The sample bends upon contact of the drop and no oscillating signal is acquired.
- Second, a high force shock was induced at the tip of the sample. This results in a sharp peak but no other effect was observed. This is because IPMC is a really soft material.
- Third, a high pulse of 5 volt peak to peak at 1 and 5 Hz was applied to the IPMC sample. The result shows a spike due of input voltage followed by no further oscillation.

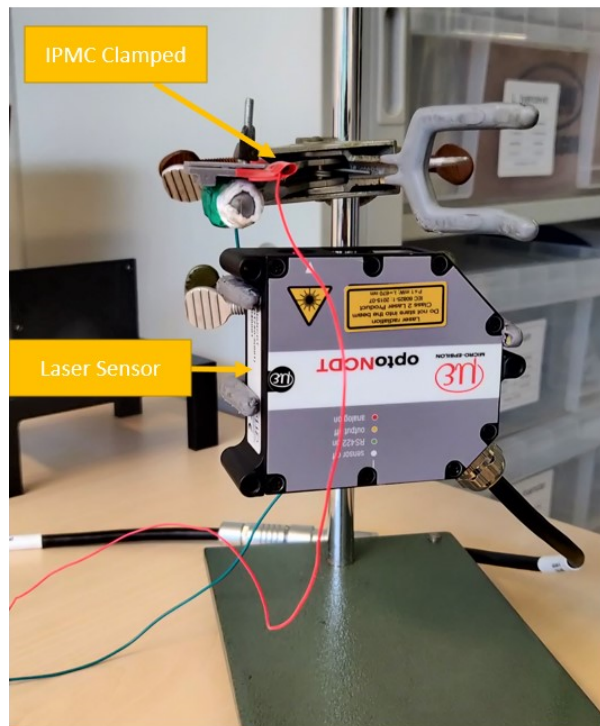


Figure 69: Setup for resonance frequency experiment.

A simple concept of beam theory was investigated briefly since no concrete conclusion can be derived from the experiments performed. Figure - 64 depicts vibration mode of the beam similar to that of our IPMC actuator. This is the first vibrational mode.

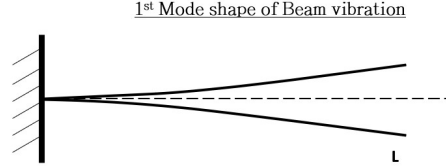


Figure 70: Schematic of the first vibrational mode shape.

Natural frequency of this mode of vibration can be derived using the equation given below [57]. The reader is suggested to consult the book for further explanation and derivation of the equation. The equation for natural frequency of a cantilever beam bending in transverse direction is as follows:

$$\omega_n = (\beta_n L)^2 \sqrt{\frac{EI}{\rho A L^4}}$$

where, ω_n - Natural frequency in radians,
L - Beam length (Active beam length) = 0.005 m ,
E - Young's modulus = 6.5×10^8 Pa ,
I - Moment of Inertia = $\frac{bh^3}{12}$ for cantilever shape = 1.33×10^{-15} ,
 ρ - Density = 5500 kg/m^3
A - Area = $1 \times 10^{-5} \text{ m}^2$
 $\beta_n L = 1.8751$ (for the first mode)

Using the above equation, natural frequency obtained is 556.63 rad/s or 88.59 Hz . This estimated value is very high to produce a beat envelope when the IPMC sample is actuated at 5 Hz frequency.

Then, Fast Fourier Transform (FFT) analysis was done on the acquired post processed force signal. FFT analysis is an algorithm that converts signal from the time or space domain into the frequency domain or vice-versa. [58]

The FFT algorithm used in this analysis is a part of the *scipy.signal* package in python.[59-63] The python code can be found in Appendix - II

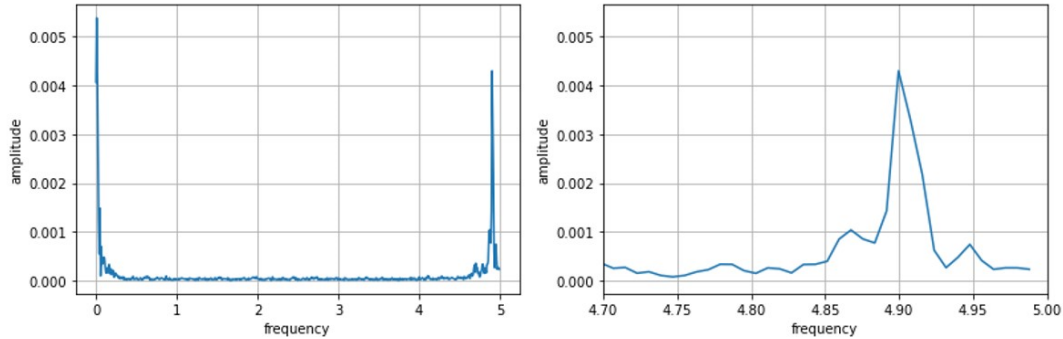


Figure 71: FFT analysis at 5 Hz for the 7 mm IPMC, $4V_{pp}$. Left: Full plot, Right: Zoomed in plot.

Figure - 71 shows fourier analysis of the 7 mm IPMC sample actuated at 4 V, 5 Hz. As seen, there are two peaks visible in the given plot. One is at zero frequency, which is because of a DC component present in the data and it can be ignored. The second peak is at 4.9 Hz. This peak belongs to the input driving frequency since Arduino board does not apply exactly 5 Hz frequency but very close to it. However, the peak of interest is not visible in the fourier analysis performed.

Another drawback of the resultant analysis is that no signal beyond 5 Hz is represented in the FFT plot. The code was then verified by analyzing data at 1 and 0.1 Hz frequency. The peaks at driving frequency were obtained as expected along with some very small peaks which could be a result of noise. But one constant feature which was observed in all the FFT analysis was that no signal is obtained beyond 5 Hz frequency. Upon further investigation it was found that this behavior is a result of under-sampling.

The sampling rate of load cell and displacement sensor for the acquired data is 10 Hz. In theory the sampling rate should be 1000 Hz for the displacement sensor and is dependent on bandwidth of the system connected to these sensors. Hence, actuation at 5 Hz frequency was not a ideal choice. According to Nyquist sampling theorem, the highest frequency spectrum of a FFT analysis is half the sampling rate. [64] This led to formation of beat

envelope since the higher frequencies were folded into the resultant spectrum.

To obtain higher frequencies in the FFT spectra, the sampling rate should be greater than 5 Hz. The laptop or system to which the sensors are connected should have a higher bandwidth. If that is not possible, then two sensors (i.e. two similar load cells or displacement sensors) with different output frequencies should be used in order to obtain a high sampling rate.

- *Tip - deflection experiments*

Data acquired for 1 and 0.1 Hz displacement measurement is similar to that obtained for tip-force experiments which has been discussed before. The explanation for all the plot behaviour remains the same and is valid for all the lengths. However, for the 5 Hz frequency the results vary.

In case of the 7 mm IPMC sample, there exists step like features which are a result of low resolution of the sensor and the total deflection span is approximately 0.002 mm.

For 9 mm IPMC, there is formation of envelope as discussed before. Each envelope contain approximately 5 peaks and the time duration of one envelope is approximately 1 second. This corresponds to the actuation driving frequency. The number of peaks in an envelope acquired from the force sensor consists of approximately 24 peaks and the time duration is 5.5 seconds. This change in behavior was checked using the before mentioned resonance experiments and FFT analysis, the result appeared to be the same. The cause was identified under-sampling and is discussed before.

The experimental results for 0.1 and 1 Hz input frequency align with theory explained in the literature regarding the tip-force and tip deflection measurements. It is given below.

The mechanical characteristics of IPMC depend heavily on the actuation frequency. Tip displacement obtained during the experiment performed in this thesis project show that the 7 mm IPMC has a displacement of 0.29 mm

at 0.1 Hz and 0.035 mm at 1 Hz. It has been reported in literature that the displacement decreases as the actuation frequency increases. Explanation for this behavior is related to the elastic modulus which IPMC attains during different frequencies. At lower frequencies (> 1 Hz) the effective elastic modulus is small, whereas at higher frequencies (< 5 Hz) the effective elastic modulus increases which decreases the maximum displacement. [83]

Future work

Tip-force and deflection experiments have been performed for three lengths of IPMC at different peak to peak voltages and frequencies. The IPMC samples were actuated in air for this project. The next step is to integrate the IPMC samples in PDMS layer.

The results from this thesis project can further be used in the future COMSOL simulations which will include a water medium under the PDMS layer in a pump chamber. Addition of water and pump chamber will lead to change in the force and displacement results. After estimating the results in COMSOL, experiments for the same should be performed.

Following the integration of IPMC in PDMS, an investigation should be performed to find the optimum PDMS thickness with low elastic modulus, which is sturdy enough for a long actuation lifetime. The positioning of the IPMC cantilever is also vital as it results in different displacement values. This should be combined with PDMS thickness study. The tip-force results from this report can be used in the model to obtain an efficient flow rate for the in-progress microfabricated micropump. If required, a new method to determine IPMC density can be explored.

Finally, it is vital to calculate the natural frequency of the IPMC sample. This is because IPMC will generate the highest tip-force at its natural frequency than at any other driving frequency. Further research on sulfonate cluster vibration and the influence of liquid bridge should be considered as they might be crucial for IPMC actuation in dry conditions.

Conclusion

In conclusion, this study involved investigation and experimentation of 7, 9 and 11 mm long, 2 mm wide and 0.2 mm thick IPMC samples to determine their tip-force and tip-displacement. The experimental results obtained were described at macro and microscopic scale. IPMC at small scale was found to possess viscoelastic properties and classical mechanical theories should not be used to validate the experimental results.

The data acquired and post processed at 1 and 0.1 Hz perfectly aligns with the input actuation frequency. A valid explanation of the back relaxation phenomenon attained by IPMC at these frequencies was provided at microscopic scale. There exists formation of beat envelope when the IPMC was actuated at 5 Hz. It was further concluded that the beat effect was caused due to under-sampling. Hence the reported force measurements at 5 Hz driving frequency cannot be trusted. It was concluded that peak tip-force increases as the IPMC length decreases. The 7 mm IPMC produced a highest peak tip-force of 0.138 mN at $3.5 V_{pp}$. Also, the 7 mm sample has a maximum displacement of 0.29 mm at 0.1 Hz.

To test the endurance of IPMC, the samples were actuated until fail at a specific voltage and frequency. It was concluded that IPMC possesses remarkable mechanical deformation capabilities. The 7 mm sample starts to fail after 1000 seconds of continuous actuation, whereas the 9 and 11 mm samples endure actuation even after 6000 seconds. Some techniques for density approximation were investigated. A simple experiment was performed to determine the density of IPMC sample using Archimedes principle. The results were quite different than expected. The possible reasons can be manual error and a different material fabrication process than reported in literature. By using a composite density approximation equation, the density was estimated and used wherever necessary.

Future work based on this thesis is presented in section-5. Lastly, the result from this thesis report can be used in Lumped Parameter model combined with PDMS thickness investigation to produce an efficient diaphragm micropump for Organ on chip application.

References

- [1] Franzen, N., van Harten, W. H., Retèl, V. P., Loskill, P., van den Eijnden-van Raaij, J., IJzerman, M. (2019). Impact of organ-on-a-chip technology on pharmaceutical RD costs. *Drug discovery today*, 24(9), 1720–1724. <https://doi.org/10.1016/j.drudis.2019.06.003>
- [2] U.S. Food and Drug Administration. 2020. The Drug Development Process. [online] Available at: <https://www.fda.gov/patients/learn-about-drug-and-device-approvals/drug-development-process>; [Accessed 21 September 2020].
- [3] Zhang, B., Korolj, A., Lai, B. and Radisic, M., 2018. Advances in organ-on-a-chip engineering. *Nature Reviews Materials*, 3(8), pp.257-278.
- [4] S. Bhatia and D. Ingber, "Microfluidic organs-on-chips", *Nature Biotechnology*, vol. 32, no. 8, pp. 760-772, 2014. Available: 10.1038/nbt.2989 [Accessed 5 October 2020].
- [5] J. P. Wikswo et al., "Engineering Challenges for Instrumenting and Controlling Integrated Organ-on-Chip Systems," in *IEEE Transactions on Biomedical Engineering*, vol. 60, no. 3, pp. 682-690, March 2013, doi: 10.1109/TBME.2013.2244891.
- [6] Mohith, S., Karanth, P. and Kulkarni, S., 2019. Recent trends in mechanical micropumps and their applications: A review. *Mechatronics*, 60, pp.34-55.
- [7] Q. Cui, C. Liu and X. Zha, "Study on a piezoelectric micropump for the controlled drug delivery system", *Microfluidics and Nanofluidics*, vol. 3, no. 4, pp. 377-390, 2006. Available: 10.1007/s10404-006-0137-0 [Accessed 5 October 2020].
- [8] C. Yamahata, C. Lotto, E. Al-Assaf and M. Gijs, "A PMMA valveless micropump using electromagnetic actuation", *Microfluidics and Nanofluidics*, vol. 1, no. 3, pp. 197-207, 2004. Available: 10.1007/s10404-004-0007-6 [Accessed 5 October 2020].
- [9] E. Kivrak, K. Yurt, A. Kaplan, I. Alkan and G. Altun, "Effects of electromagnetic fields exposure on the antioxidant defense system", *Journal*

- of Microscopy and Ultrastructure, vol. 5, no. 4, p. 167, 2017. Available: 10.1016/j.jmau.2017.07.003 [Accessed 5 October 2020].
- [10] T. T. Nguyen, V. K. Nguyen, Y. Yoo, and N. S. Goo, "A Novel Polymeric Micropump based on a Multilayered Ionic Polymer-Metal Composite," IECON 2006 - 32nd Annual Conference on IEEE Industrial Electronics, 2006.
- [11] "How Do Air Pumps Work?", Sciencing, 2020. [Online]. Available: <https://sciencing.com/how-do-air-pumps-work-13403095.html>. [Accessed: 05- Oct- 2020].
- [12] F. Van de Pol, H. Van Lintel, M. Elwenspoek and J. Fluitman, "A thermopneumatic micropump based on micro-engineering techniques", Sensors and Actuators A: Physical, vol. 21, no. 1-3, pp. 198-202, 1990. Available: 10.1016/0924-4247(90)85038-6 [Accessed 5 October 2020].
- [13] A. (Prochaska), Y. Nemirovsky and U. Dinnar, "A membrane micropump electrostatically actuated across the working fluid", Journal of Micromechanics and Microengineering, vol. 15, no. 12, pp. 2309-2316, 2005. Available: 10.1088/0960-1317/15/12/013 [Accessed 5 October 2020].
- [14] En.wikipedia.org. 2020. Piezoelectricity. [online] Available at: <https://en.wikipedia.org/wiki/Piezoelectricity> [Accessed 21 September 2020].
- [15] Huang, J., Zou, L., Tian, P., Zhang, Q., Wang, Y. and Zhang, J., 2019. A Valveless Piezoelectric Micropump Based on Projection Micro Litho Stereo Exposure Technology. IEEE Access, 7, pp.77340-77347.
- [16] Junwu, K., Zhigang, Y., Taijiang, P., Guangming, C. and Boda, W., 2005. Design and test of a high-performance piezoelectric micropump for drug delivery. Sensors and Actuators A: Physical, 121(1), pp.156-161.
- [17] A. Chandrasekaran and M. Packirisamy, "Geometrical tuning of microdiffuser/nozzle for valveless micropumps," Journal of Micromechanics and Microengineering, vol. 21, no. 4, p. 045035, 2011.
- [18] K. Keizer, "Determination whether a large scale Tesla valve could be applicable as a fish passage", Delft University of Technology, Department of Civil Engineering, 2628CN Delft, PO-Box 5048, The Netherlands, 2016

- [19] E. Stemme and G. Stemme, “A valveless diffuser/nozzle-based fluid pump,” *Sensors and Actuators A: Physical*, vol. 39, no. 2, pp. 159–167, 1993.
- [20] “Figure 2f from: Irimia R, Gottschling M (2016) Taxonomic revision of *Rochefortia* Sw. (Ehretiaceae, Boraginales). *Biodiversity Data Journal* 4: e7720. <https://doi.org/10.3897/BDJ.4.e7720>.”
- [21] A. Olsson , “Valve-less diffuser micropumps ,” dissertation, 1998.
- [22] M. Nafea, M. S. M. Ali, T. Rehman, and K. Mehranzamir, “Geometrical Analysis of Diffuser-Nozzle Elements for Valveless Micropumps,” 2019 IEEE International Conference on Smart Instrumentation, Measurement and Application (ICSIMA), 2019.
- [23] R. Kumar, P. SenthamaraiKannan, S. Saravanakumar, A. Khan, K. Ganesh, and S. V. Ananth, “Electroactive polymer composites and applications,” *Polymer Nanocomposite-Based Smart Materials*, pp. 149–156, 2020.
- [24] G. H. Kwon, G. S. Jeong, J. Y. Park, J. H. Moon, and S.-H. Lee, “A low-energy-consumption electroactive valveless hydrogel micropump for long-term biomedical applications,” *Lab on a Chip*, vol. 11, no. 17, p. 2910, 2011.
- [25] Y. Wang, C. Zhao, J. Wang, Z. Zhu, D. Zhu, and M. Luo, “Design and Fabrication of an IPMC Actuated Micro-Pump With Inner Petal-Shaped Diaphragm,” 2018 3rd International Conference on Advanced Robotics and Mechatronics (ICARM), 2018.
- [26] Ionic polymer–metal composites.(2020).Retrieved 21 September 2020, from https://en.wikipedia.org/wiki/Ionic_polymer%E2%80%93metal_composites
- [27] Z. Chen, T. I. Um, and H. Bart-Smith, “A novel fabrication of ionic polymer–metal composite membrane actuator capable of 3-dimensional kinematic motions,” *Sensors and Actuators A: Physical*, vol. 168, no. 1, pp. 131–139, 2011.
- [28] M. Shahinpoor, Y. Bar-Cohen, J. Simpson and J. Smith, ”Ionic polymer-metal composites (IPMCs) as biomimetic sensors, actuators and artificial

- muscles - a review”, *Smart Materials and Structures*, vol. 7, no. 6, pp. R15-R30, 1998. Available: [10.1088/0964-1726/7/6/001](https://doi.org/10.1088/0964-1726/7/6/001).
- [29] Annabestani, M. (2019, April 9). Ionic Electro active Polymer-Based Soft Actuators and Their. . . ArXiv.Org. <https://arxiv.org/abs/1904.07149>
- [30] P. Motreuil-Ragot, A. Hunt, D. Kasi, B. Brajon, A. V. D. Maagdenberg, V. Orlova, M. Mastrangeli, and P. M. Sarro, “Enabling actuation and sensing in organs-on-chip using electroactive polymers,” 2020 3rd IEEE International Conference on Soft Robotics (RoboSoft), 2020.
- [31] Valenzuela, E., Gamboa, S. A., Sebastian, P. J., Moreira, J., Serna, S. (2009, February 1). Proton Charge Transport in Nafion Nanochannels. ResearchGate. https://www.researchgate.net/publication/244990520_Proton_Charge_Transport_in_Nafion_Nanochannels
- [32] Polymer Electrolyte Membranes for Microbial Fuel Cells: Part A. Nafion-Based Membranes. (2018, January 1). ScienceDirect. <https://www.sciencedirect.com/science/article/pii/B978044464017800004X>
- [33] Shahinpoor, M., Bar-Cohen, Y., Simpson, J. O., Smith, J. (1998). Ionic polymer-metal composites (IPMCs) as biomimetic sensors, actuators and artificial muscles-a review. *Smart materials and structures*, 7(6), R15.
- [34] Human Organs-on-Chips. (n.d.). Wyss.Harvard.Edu. <https://wyss.harvard.edu/technology/human-organs-on-chips/><https://wyss.harvard.edu/technology/human-organs-on-chips/>
- [35] Low, L. A. (2021, October 13). Adoption of organ-on-chip platforms by the pharmaceutical industry. *Nature Reviews Drug Discovery*. https://www.nature.com/articles/s41573-020-0079-3?error=cookies_not_supported&code=7745b857-22a5-4cd0-bb94-6590a238c575
- [36] cellix, ireland. (2021). Organ-on-Chip Applications. Wearecellix. Retrieved November 16, 2021, from <https://www.wearecellix.com/organ-on-chip>

- [37] Electromagnetic Pump for Organs-on-Chips, and Valve and Pump Designs for Organs-on-Chips — MIT Technology Licensing Office. (2019). Technology Licensing Office, MIT. <https://tlo.mit.edu/technologies/electromagnetic-pump-organs-chips-and-valve-and-pump-designs-organs-chips>
- [38] Fong, J. (2015b, February 3). Wireless implantable chip with integrated nitinol-based pump for radio-controlled local drug delivery. Lab on a Chip (RSC Publishing). <https://pubs.rsc.org/en/content/articlelanding/2015/lc/c4lc01290a>
- [39] Trumper., D. L. (2018, August 8). Electromagnetic pump and hardware development for organs-on-chips. Dspace,MIT. <https://dspace.mit.edu/handle/1721.1/117299>
- [40] Wikipedia contributors. (2021a, September 20). Micropump. Wikipedia. <https://en.wikipedia.org/wiki/Micropump>
- [41] Mauritz, K. A., Moore, R. B. (2004). State of Understanding of Nafion. ChemInform, 35(50). <https://doi.org/10.1002/chin.200450273>
- [42] Porfiri, M., Sharghi, H., Zhang, P. (2018). Modeling back-relaxation in ionic polymer metal composites: The role of steric effects and composite layers. Journal of Applied Physics, 123(1), 014901. <https://doi.org/10.1063/1.5004573>
- [43] Fleming, M. J., Kim, K. J., Leang, K. K. (2012). Mitigating IPMC back relaxation through feedforward and feedback control of patterned electrodes. Smart materials and structures, 21(8), 085002.
- [44] Forouzandeh, F., Arevalo, A., Alfadhel, A., Borkholder, D. A. (2021). A review of peristaltic micropumps. Sensors and Actuators A: Physical, 326, 112602. <https://doi.org/10.1016/j.sna.2021.112602>
- [45] Laser, Daniel J., and Juan G. Santiago. "A review of micropumps." Journal of micromechanics and microengineering 14.6 (2004): R35.
- [46] Fang, Yang, and Xiaobo Tan. "A novel diaphragm micropump actuated by conjugated polymer petals: Fabrication, modeling, and experimental results." Sensors and Actuators A: Physical 158.1 (2010): 121-131.

- [47] Simpson, J., Lumia, R., Martinez, M. (2013). Force and deflection modeling of IPMC fingers. 2013 10th IEEE INTERNATIONAL CONFERENCE ON NETWORKING, SENSING AND CONTROL (ICNSC). Published. <https://doi.org/10.1109/icnsc.2013.6548725>
- [48] Hao, M. (2019). A Compact Review of IPMC as Soft Actuator and Sensor: Current Trends, Challenges, and Potential Solutions From Our Recent Work. *Frontiers*. <https://www.frontiersin.org/articles/10.3389/frobt.2019.00129/full>
- [49] Modeling of IPMC Cantilever's Displacements and Blocking Forces. (2015, January 1). ScienceDirect. <https://www.sciencedirect.com/science/article/abs/pii/S1672652914601086>
- [50] Nemat-Nasser, S. (2002). Micromechanics of actuation of ionic polymer-metal composites. *Journal of Applied Physics*, 92(5), 2899–2915. <https://doi.org/10.1063/1.1495888>
- [51] Kim, Tae-Hyun, et al. "Influence of the Nafion agglomerate morphology on the water-uptake behavior and fuel cell performance in the proton exchange membrane fuel cells." *Applied Surface Science* 481 (2019): 777-784.
- [52] Annabestani, M., Sayad, M. H., Esmaeili-Dokht, P., Gorji, R., Fardmanesh, M. (2020). Eliminating Back Relaxation in Large-Deformable IPMC Artificial Muscles: A Noise-Assistive Pattern-Free Electrode Approach. 2020 27th National and 5th International Iranian Conference on Biomedical Engineering (ICBME). Published. <https://doi.org/10.1109/icbme51989.2020.9319432>
- [53] Physics Tutorial: Interference and Beats. (n.d.). Physicsclassroom.Com. Retrieved 2021, from <https://www.physicsclassroom.com/class/sound/Lesson-3/Interference-and-Beats>
- [54] Moebis, W. (2016, August 3). 17.6 Beats University Physics Volume 1. Pressbooks. <https://opentextbc.ca/universityphysicsv1openstax/chapter/17-6-beats/>

- [55] Wikipedia contributors. (2021c, November 18). Electrolysis of water. Wikipedia. https://en.wikipedia.org/wiki/Electrolysis_of_water
- [56] Mondal, M. (2021, August 16). IPMC Based Flexible Platform: A Boon to the Alternative Energy Solution. IntechOpen. <https://www.intechopen.com/online-first/78105>
- [57] Rao, S. S. (2007). Vibration of Continuous Systems. Wiley.
- [58] Wikipedia contributors. (2021c, November 17). Fast Fourier transform. Wikipedia. https://en.wikipedia.org/wiki/Fast_Fourier_transform
- [59] Real Python. (2021, June 26). Fourier Transforms With `scipy.fft`: Python Signal Processing. Realpython.Com. <https://realpython.com/python-scipy-fft/>
- [60] Applying Fourier Transform In Python Using `Numpy.fft`. (n.d.). Pythonic.Com. https://pythonic.com/visualization/signals/fouriertransform_fft
- [61] FFT in Python — Python Numerical Methods. (n.d.). Pythonnumericalmethods.Berkeley.Edu. <https://pythonnumericalmethods.berkeley.edu/notebooks/chapter24.04-FFT-in-Python.html>
- [62] Nunez-Iglesias, J. (n.d.). Elegant SciPy. O’Reilly Online Learning. <https://www.oreilly.com/library/view/elegant-scipy/9781491922927/ch04.html>
- [63] Fourier Transforms (`scipy.fft`) — SciPy v1.7.1 Manual. (n.d.). Scipy.Org. <https://docs.scipy.org/doc/scipy/reference/tutorial/fft.html>
- [64] Wikipedia contributors. (2021a, April 9). Nyquist frequency. Wikipedia. https://en.wikipedia.org/wiki/Nyquist_frequency
- [65] Human organ chips enable rapid drug repurposing for COVID-19. (2021, May 12). Wyss Institute. <https://wyss.harvard.edu/news/human-organ-chips-enable-rapid-drug-repurposing-for-covid-19/>
- [66] Yamahata, Christophe, et al. "Pumping of mammalian cells with a nozzle-diffuser micropump." Lab on a Chip 5.10 (2005): 1083-1088.

- [67] Bhandari, Binayak, Gil-Yong Lee, and Sung-Hoon Ahn. "A review on IPMC material as actuators and sensors: fabrications, characteristics and applications." *International journal of precision engineering and manufacturing* 13.1 (2012): 141-163.
- [68] Shahinpoor, M. (2015). *Ionic Polymer Metal Composites (IPMCs): Smart Multi-Functional Materials and Artificial Muscles, Volume 1 (Smart Materials Series, 17) (1st ed.)*. Royal Society of Chemistry.
- [69] Nemat-Nasser, Siavouche, and Shahram Zamani. "Experimental study of Nafion-and Flemion-based ionic polymer metal composites (IPMCs) with ethylene glycol as solvent." *Smart Structures and Materials 2003: Electroactive Polymer Actuators and Devices (EAPAD)*. Vol. 5051. International Society for Optics and Photonics, 2003.
- [70] Zhu, Z. C., Chen, H. L., Li, B., Wang, Y. Q. (2010). Characteristics and Elastic Modulus Evaluation of Pd-Nafion Ionic Polymer-Metal Composites. *Advanced Materials Research*, 97–101, 1590–1594. <https://doi.org/10.4028/www.scientific.net/amr.97-101.1590>
- [71] True Density — Gas Pycnometry and Helium Pycnometry — Merlin PC. (n.d.-b). Merlin-Pc. <https://www.merlin-pc.com/services/density-testing/true-density-and-helium-pycnometry>:
- [72] Wikipedia contributors. (2021c, September 7). Load cell. Wikipedia. https://en.wikipedia.org/wiki/Load_cell :
- [73] Why is it Important to Calibrate your Load Cell? Force Sensor Transducer Calibration Curve. (n.d.-a). FUTEK Advanced Sensor Technology. <https://www.futek.com/load-cell-calibration-services>
- [74] Toepke, M. W., Beebe, D. J. (2006). PDMS absorption of small molecules and consequences in microfluidic applications. *Lab on a Chip*, 6(12), 1484. <https://doi.org/10.1039/b612140c>
- [75] Micro- and nanopatterning of biomaterial surfaces. (2018, January 1). ScienceDirect. <https://www.sciencedirect.com/science/article/pii/B9780081022054000039>

- [76] Nguyen, Thanh Tung, et al. "Design, fabrication, and experimental characterization of a flap valve IPMC micropump with a flexibly supported diaphragm." *Sensors and Actuators A: Physical* 141.2 (2008): 640-648.
- [77] Nam, Doan Ngoc Chi, and Kyoung Kwan Ahn. "Design of an IPMC diaphragm for micropump application." *Sensors and Actuators A: Physical* 187 (2012): 174-182.
- [78] Mishra, Richa, Tapas K. Maiti, and Tarun K. Bhattacharyya. "A novel design and characterisation of Nafion 115 membrane for micropump based transdermal drug delivery." *Proc. MicroTAS*. 2018.
- [79] Lee, Sangki, and Kwang J. Kim. "Design of IPMC actuator-driven valveless micropump and its flow rate estimation at low Reynolds numbers." *Smart materials and structures* 15.4 (2006): 1103.
- [80] Hsu, William Y., and Timothy D. Gierke. "Ion transport and clustering in Nafion perfluorinated membranes." *Journal of Membrane Science* 13.3 (1983): 307-326.
- [81] Li, Jiang Yu, and Sia Nemat-Nasser. "Micromechanical analysis of ionic clustering in Nafion perfluorinated membrane." *Mechanics of materials* 32.5 (2000): 303-314.
- [82] Hao, Muyu, et al. "A compact review of IPMC as soft actuator and sensor: current trends, challenges, and potential solutions from our recent work." *Frontiers in Robotics and AI* 6 (2019): 129.
- [83] Modeling of IPMC Cantilever's Displacements and Blocking Forces. (2015b, January 1). ScienceDirect. <https://www.sciencedirect.com/science/article/abs/pii/S1672652914601086>

Appendix - I

The Python code used post process the acquired data, find the peaks and calculate the amplitude of the signal can be found below. This code also includes the bandpass filter using *scipy.signal.butter* from the *scipy* package for future reference, if required.

```
from matplotlib import pyplot
from pylab import genfromtxt
import matplotlib.pyplot as plt
import scipy
from scipy.signal import find_peaks
from statistics import mean , stdev
import numpy as np
from columnar import columnar

# Bnad pass filter function
def bandpassfilter(signal):

    # sampling rate (in Hz): No. of samples per second
    fs = 10
    # start and stop frequencies for bandpass or bandstop
    # → filter
    #lowcut = 1
    highcut = 2.5

    nyq = 0.5 * fs
    #low = lowcut/nyq
    high = highcut/nyq

    order = 2
```

```

# Apply butterworth low pass filter
b,a = scipy.signal.butter(order, [high], 'highpass', analog
    ↪ = False )
y = scipy.signal.filtfilt(b,a, signal, axis=0)

return(y)

# Importing the txt file
mat0 = genfromtxt("2v_2.txt")

time = mat0[:,0]/1000
force = mat0[:,4]

plt.plot(force, label = "2_V")
pyplot.ylabel("Force_(mN)")
pyplot.xlabel("time_(sec)_/_10")
plt.legend(loc = "best")

# Find peaks for unfiltered
peak, _ = find_peaks(force, height= 0 , threshold = (0, .04) ,
    ↪ distance= 1 , prominence= 0)
plt.plot(peak, force[peak], "x", color = 'r')

# Not Multiply by 2 to get the value of full amplitude
ly1 = force[peak]

# mean_unfiltered = mean(ly1)
# std_unfiltered = stdev(ly1)
# print ("unfiltered mean: ", mean_unfiltered, ";" , "st. dev.
    ↪ unfiltered: " , ':', std_unfiltered)

```

```

pyplot.grid()
pyplot.show()

#-----

    # Plot with filter
filtered_signal = bandpassfilter(force)
# pyplot.plot(time, filtered_signal)
# pyplot.ylabel("F(mN)")
# pyplot.xlabel("t(sec)")
# pyplot.grid()
# # pyplot.show()

    # Find peak
peak, _ = find_peaks(filtered_signal, height= 0 , threshold =
    ↪ (0.0, 1), distance= 1 , prominence= 0)
# plt.plot(filtered_signal)

# plt.plot(peak, filtered_signal[peak], "x", color = 'r')
# pyplot.ylabel("F(mN)")
# pyplot.xlabel("t(sec) / 10")
# pyplot.grid()
# pyplot.show()

# # Multiply by 2 to get the value of full amplitude
# ly = filtered_signal[peak] * 4

# mean_filtered = mean(ly)
# std_filtered = stdev(ly)
# print ("filtered mean: ", mean_filtered, ";" , "st. dev.
    ↪ filtered: " , ':', std_filtered)

```

```

#-----

# Threshold value (for height of peaks and valleys)
thresh = 0.000

# Find indices of peaks
peak_idx, _ = find_peaks(filtered_signal, height=thresh)

# Find indices of valleys (from inverting the signal)
valley_idx, _ = find_peaks(-filtered_signal, height=thresh)

# Plot signal
# plt.plot(time, filtered_signal)

# # Plot peaks (red) and valleys (blue)
# plt.plot(time[peak_idx], filtered_signal[peak_idx], 'r.')
# plt.plot(time[valley_idx], filtered_signal[valley_idx], 'b
    ↪ .')

# plt.grid()
# plt.show()

# find peak and valley values
peak_value = filtered_signal[peak_idx]
valley_value = filtered_signal[valley_idx]

# # check the number of peaks and valleys
# print ("No. of peaks: ", len(peak_value), "No. of valleys:
    ↪ " , len(valley_value))

# # print ("peak : ", peak_value)

```

```

# # print("valley: ",valley_value)

# # Add 0 to either list to have same dimensions of the array
#   ↪ in order to add lists
# x = [0] * 0
# a = np.append(peak_value, x)

# # then check the length afain
# print ("No. of peaks: ",len(peak_value), "No. of valleys: "
#   ↪ ,len(a))
# amplitude=[]
# # add the peak and valley values to obtain amplitude of the
#   ↪ wave
# #amplitude = np.add(peak_value, (a))
# for i in range (0,207):
# amplitude.append(peak_value[i]-valley_value[i])

# # print (amplitude)

# # find mean of the amplitude
# amplitude_mean = mean(amplitude)
# print("mean amplitude:" , amplitude_mean)

# # find standard deviation of the amplitude
# amplitude_std = stdev(amplitude)
# print ("std amplitude:" , amplitude_std)

#-----

# To find the absolute value of the amplitude

x = 500 # window start time
y = 150 # window end time

```

```

plt.plot(force[x:x + y], label = "2V, 5Hz")
pyplot.ylabel("Force (mN)")
pyplot.xlabel("time (sec)/10")
pyplot.grid()
plt.legend(loc="best")

# Find peaks for unfiltered
peak_pos, _ = find_peaks(force[x : x + y], height= None,
    ↪ threshold = None , distance= None , prominence= None)
peak_neg, _ = find_peaks(-force[x : x + y], height= None ,
    ↪ threshold = None , distance= None , prominence= None)

plt.plot(peak_pos, force[x + peak_pos], "x", color = 'r')
plt.plot(peak_neg, force[x + peak_neg], "x", color = 'k')

print ("peak:", len(peak_pos))
print("valley:", len(peak_neg))

amplitude=[]

for i in range (0,71):
    amplitude.append(np.abs(force[x + peak_pos[i]]-force[x +
    ↪ peak_neg[i]]))

amp = [round(num, 3) for num in amplitude]

print ("Amplitude values: " , amp)

```

Python code that is used for FFT analysis is given below (two different versions are present for verification) :

```
"""
Steps for Fourier Transform:
  1. Construst a time signal ( Call the txt file in my case
     ↪ )
  2. Use fft from numpy
  3. PLOT
"""

from matplotlib import pyplot
from pylab import genfromtxt
import matplotlib.pyplot as plt
from scipy.fftpack import fftfreq, fft
from scipy.signal import find_peaks
from statistics import mean , stdev
import numpy as np
from math import log10

# Importing the txt file
mat0 = genfromtxt("4v_3.txt")

time = mat0[:,0]/1000
force = mat0[:,3]

plt.plot(time, force)
pyplot.ylabel("Force_(mN)")
pyplot.xlabel("Time_(sec)")
plt.show()

npts=len(time)
```

```

FFT = abs(fft(force))
freqs = fftfreq(npts, time[1]-time[0])

plt.plot(freqs,FFT)
plt.xlim(0,6)
plt.ylim(0,11)
plt.grid()
plt.xlabel("frequency")
plt.ylabel("amplitude")
plt.xlim(4.5,5.1)
plt.show()

# -----

# Frequency domain representation

fourierTransform = np.fft.fft(force)/len(force) # Normalize
    ↪ amplitude

fourierTransform = fourierTransform[range(int(len(force)/2))]
    ↪ # Exclude sampling frequency

# How many time points are needed i.e., Sampling Frequency

samplingFrequency = 10;

tpCount = len(force)

values = np.arange(int(tpCount/2))

timePeriod = tpCount/samplingFrequency

frequencies = values/timePeriod

```

```
plt.plot(frequencies, abs(fourierTransform))
plt.xlabel("frequency")
plt.ylabel("amplitude")
plt.xlim(4.7,5)
plt.grid()

plt.show()
```

Appendix - II

COMSOL simulations were performed before advancing to the experimental part of the project. This was done so as to achieve an expected tip force and displacement value range that the IPMC of the required dimensions can exert on the PDMS. The simulations also help us predict the mechanical movement of the system. Initially, tip force was obtained from the literature to check the displacement of the simulated IPMC + PDMS membrane. The input force value ranged from 2 - 5 mN. [48][49][50]

The dimensions and the shape of the preliminary simulated geometry is given in the figure - 72. Initial dimensions selected for the system are as follows:

IPMC: $L = 8$ mm, $W = 2$ mm , $h = 0.2$ mm and
PDMS: $R = 5$ mm, $t = 0.1$ mm.

The system was simulated as follows:

- Model Wizard is selected and the space dimensions in which the model was developed is 3D.
- A single physics interface of *Solid mechanics* was used for simplicity. The study added to is *stationary* because it is possible to compute mechanical bending deformation using it.
- Then, geometry of the system was developed (as seen in figure - 64) using the previously defined parameters (L , W , h , R and t).
- Materials to each geometry were specified. PDMS was added to the cylindrical section and a new material was added since IPMC is not a part of COMSOL material library. The material parameters required to add a new material are: *Young's modulus, Poisson ratio and density*. The values allotted to these parameters are as follows and were derived from the literature: $E = 650$ MPa, $\nu = 0.487$ and $\rho = 2500$ Kg/m³
- Then, fixed constrains were selected in the geometry. These are the parts which will be clamped and fixed in the actual experiment. They

are highlighted in blue.

- Fine mesh was selected for this model.
- Lastly, Stationary Solid mechanics study was performed and deformation of the whole system in transverse direction was obtained. The result is shown in figure - 65.

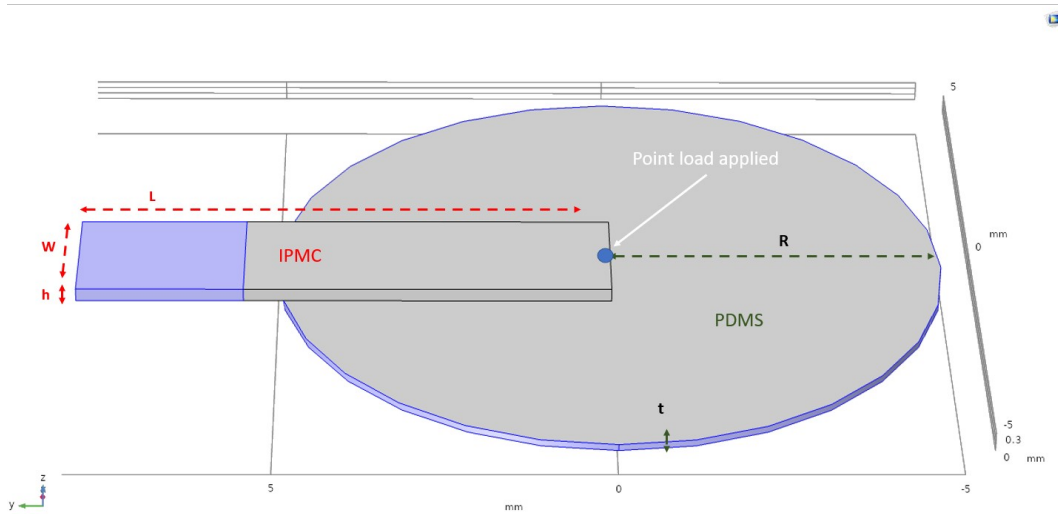


Figure 72: COMSOL model geometry.

The preliminary simulations gives a displacement of 0.12 mm when a point load of 2 mN is applied, figure -73.

After performing tip-force experiments and determining the density of our sample, the input parameters were changed as follows:
 $L = 7 \text{ mm}$, Point force = 0.138 mm and density = 5500 Kg/m^3 .

The output displacement resulted in $8.46 \times 10^{-3} \text{ mm}$.

Later, a parametric sweep of different with different thickness of PDMS was also performed. Table below represents the result:

PDMS thickness (mm)	Displacement (10^{-3} mm)
3	1.73
3.5	2.54
4	3.57
4.5	4.84
5	6.22

A few assumptions were made while performing this analysis, like ionic mobility, hydration level, influence of voltage on the sample and environmental effects were not taken into account. It can be a good start to learn about the mechanics of the system, however the experimental results will vary greatly if a simple simulation is performed.

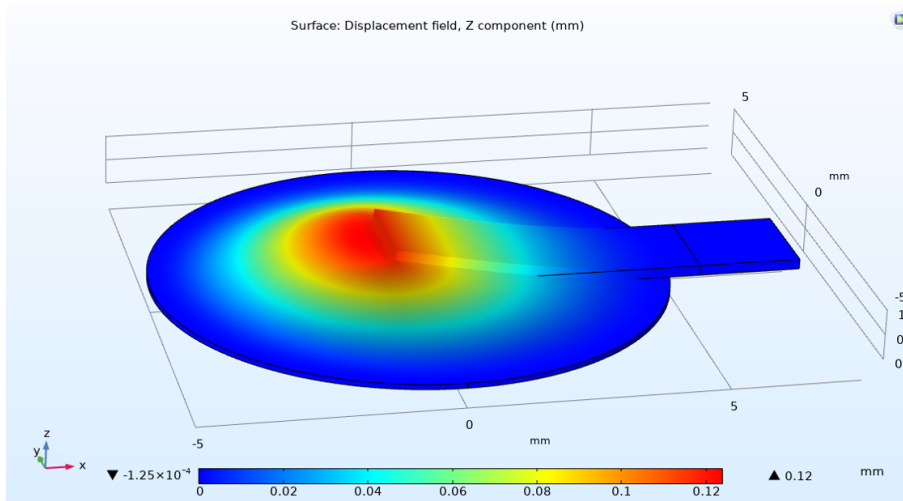
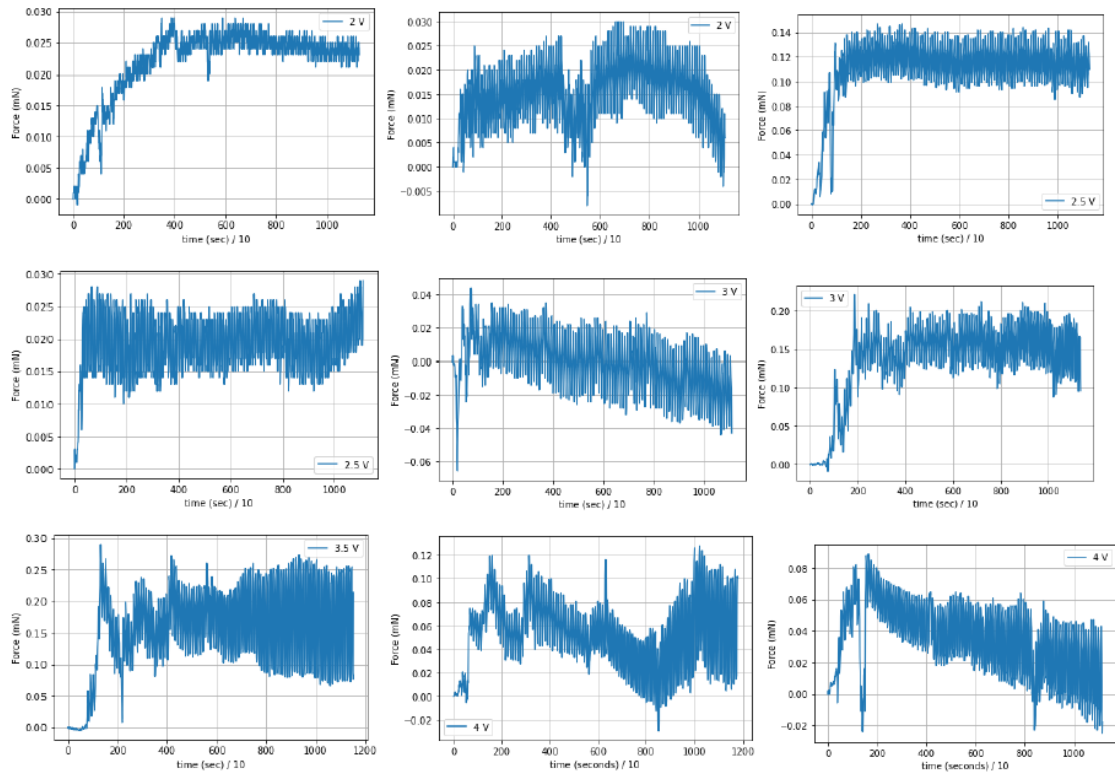


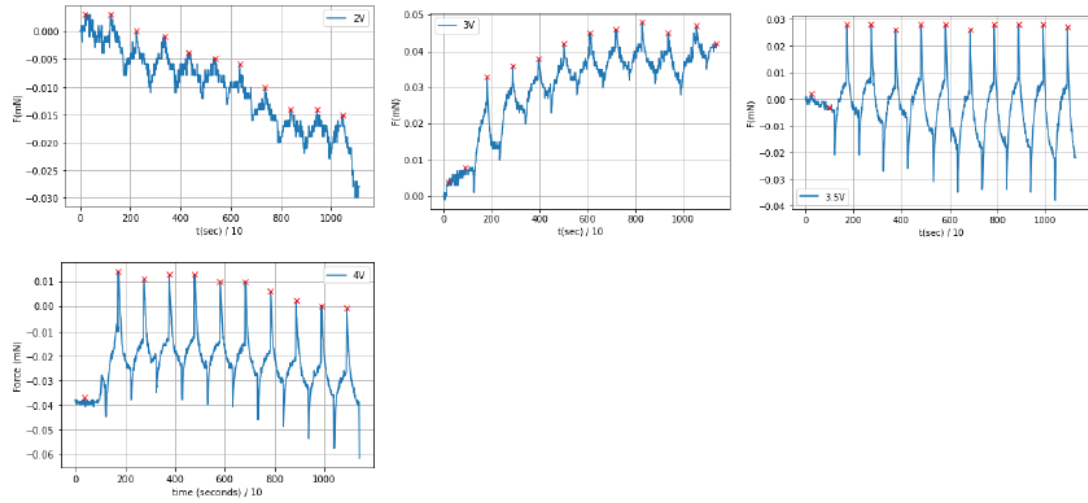
Figure 73: Preliminary COMSOL deformation result.

Appendix - III

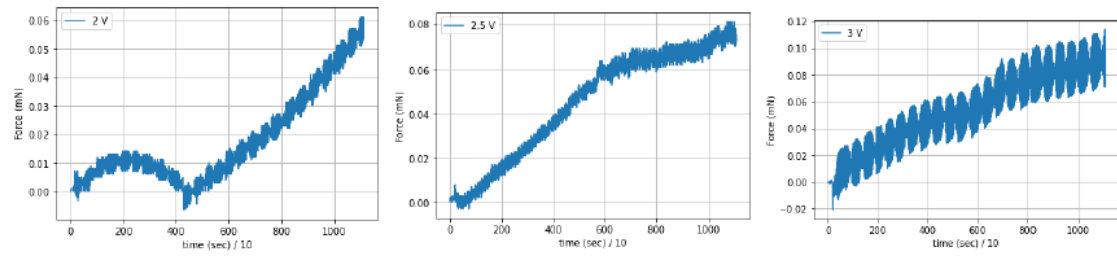
Force plots for 7mm IPMC: 1 Hz

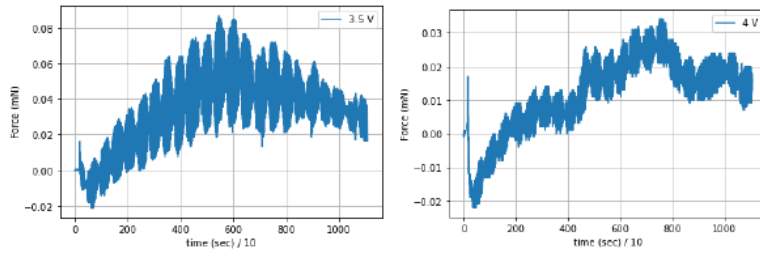


Force plots for 7mm IPMC: 0.1 Hz

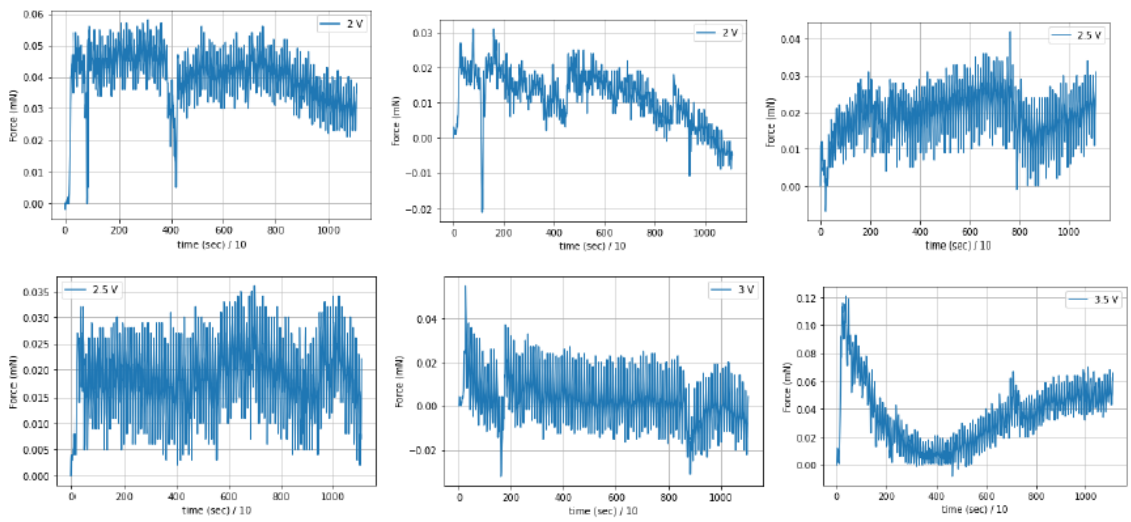


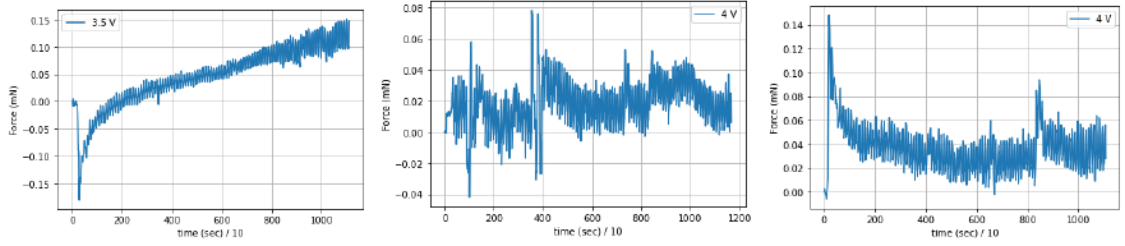
Force plots for 7mm IPMC: 5 Hz



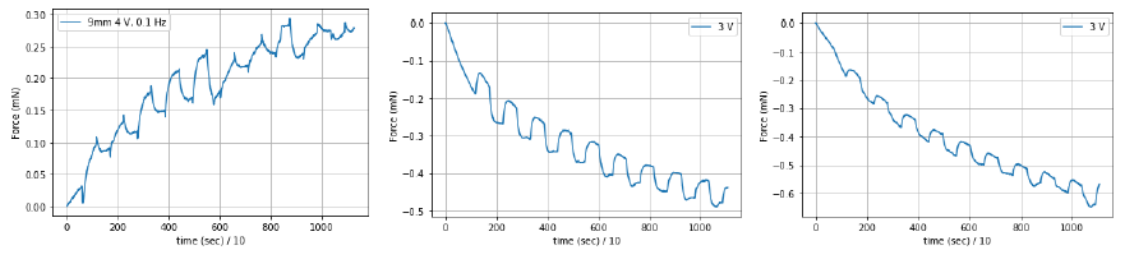


Force plots for 9 mm IPMC: 1 Hz

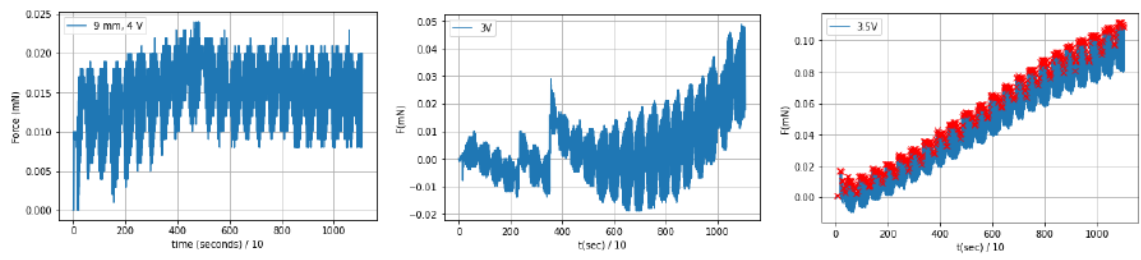


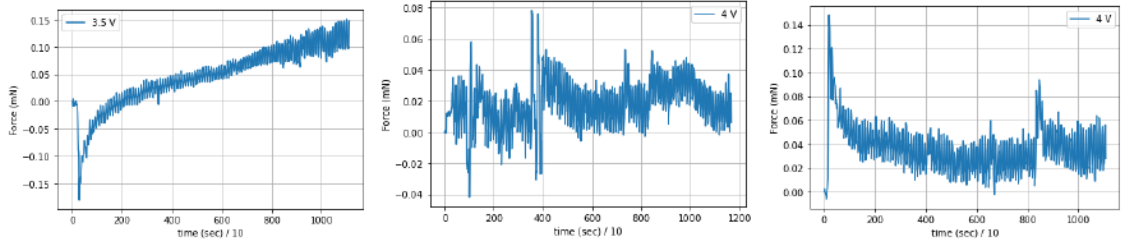


Force plots for 9 mm IPMC: 0.1 Hz

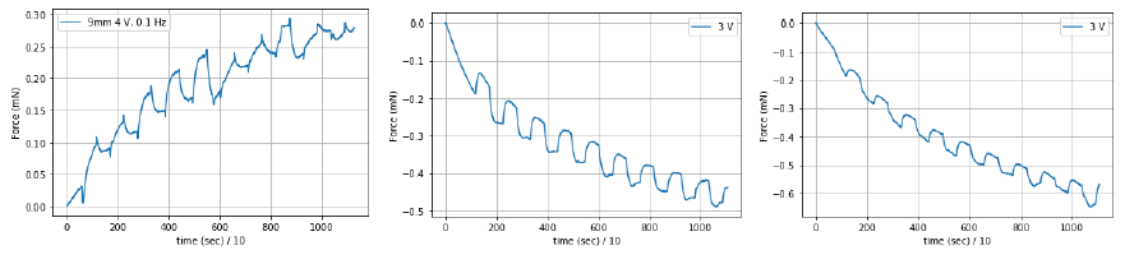


Force plots for 9 mm IPMC: 5 Hz

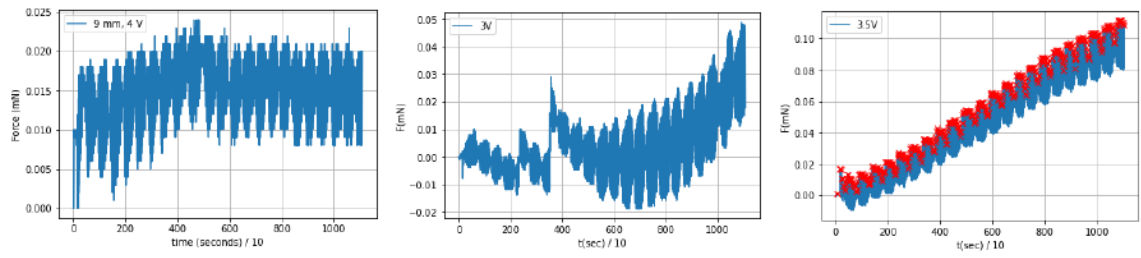




Force plots for 9 mm IPMC: 0.1 Hz

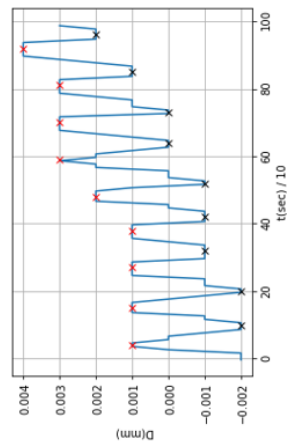
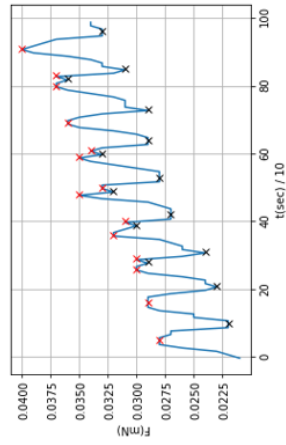


Force plots for 9 mm IPMC: 5 Hz

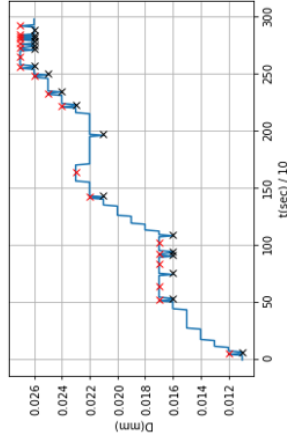
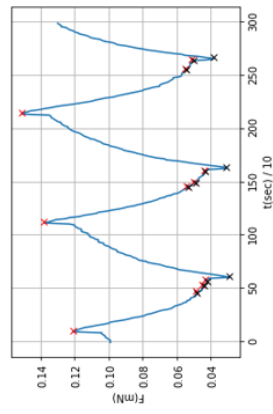


7MM

1 Hz



0.1 Hz



5 Hz

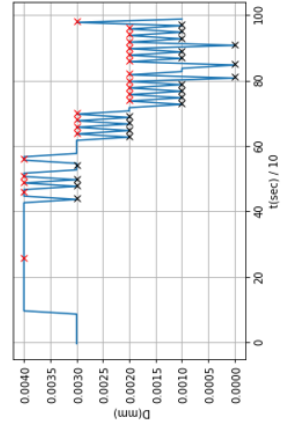
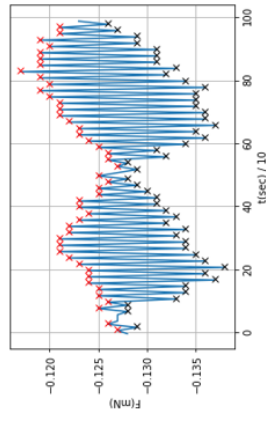


Figure 74: Tip force and displacement correlation, 7 mm IPMC. Top row: Force signal, Bottom row: Displacement signal.

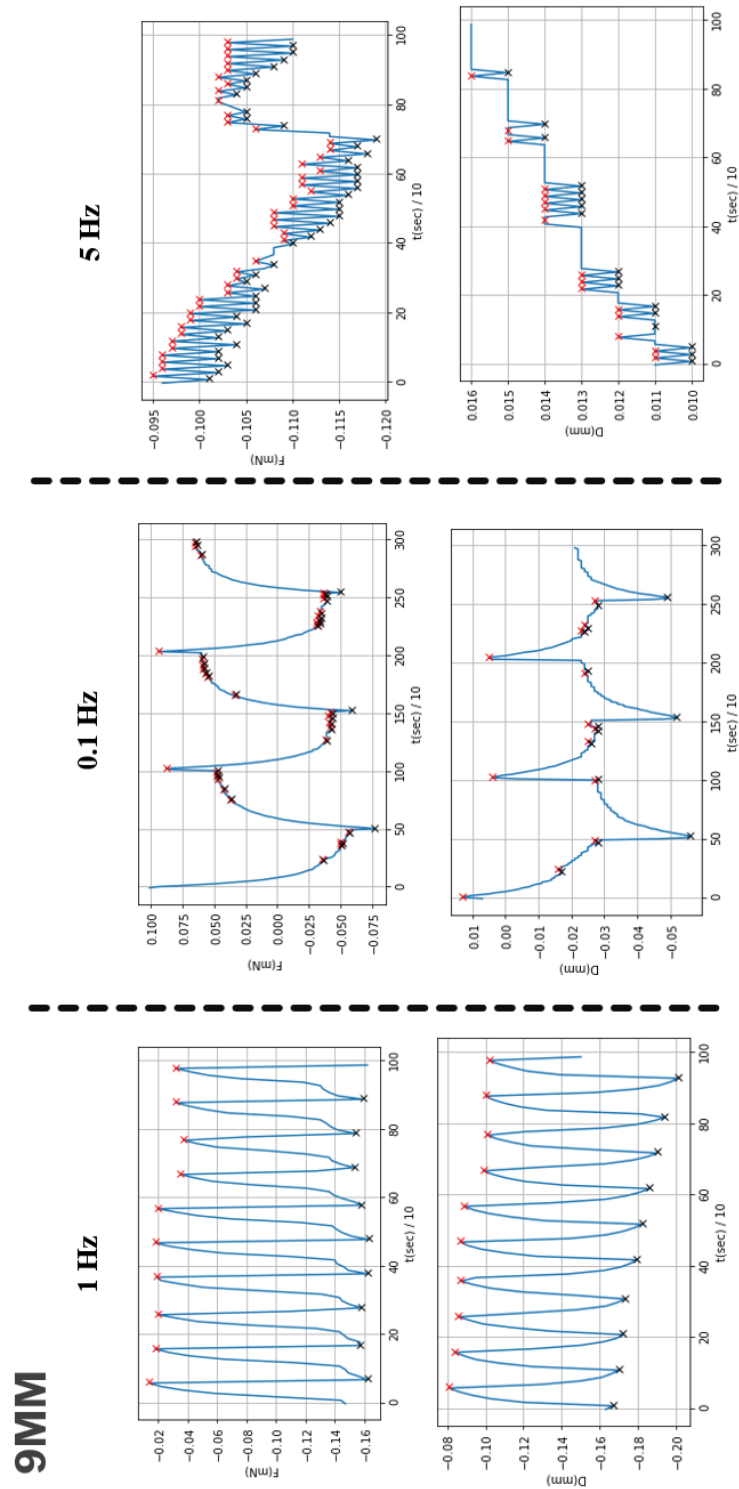


Figure 75: Tip force and displacement correlation, 9 mm IPMC. Top row: Force signal, Bottom row: Displacement signal.

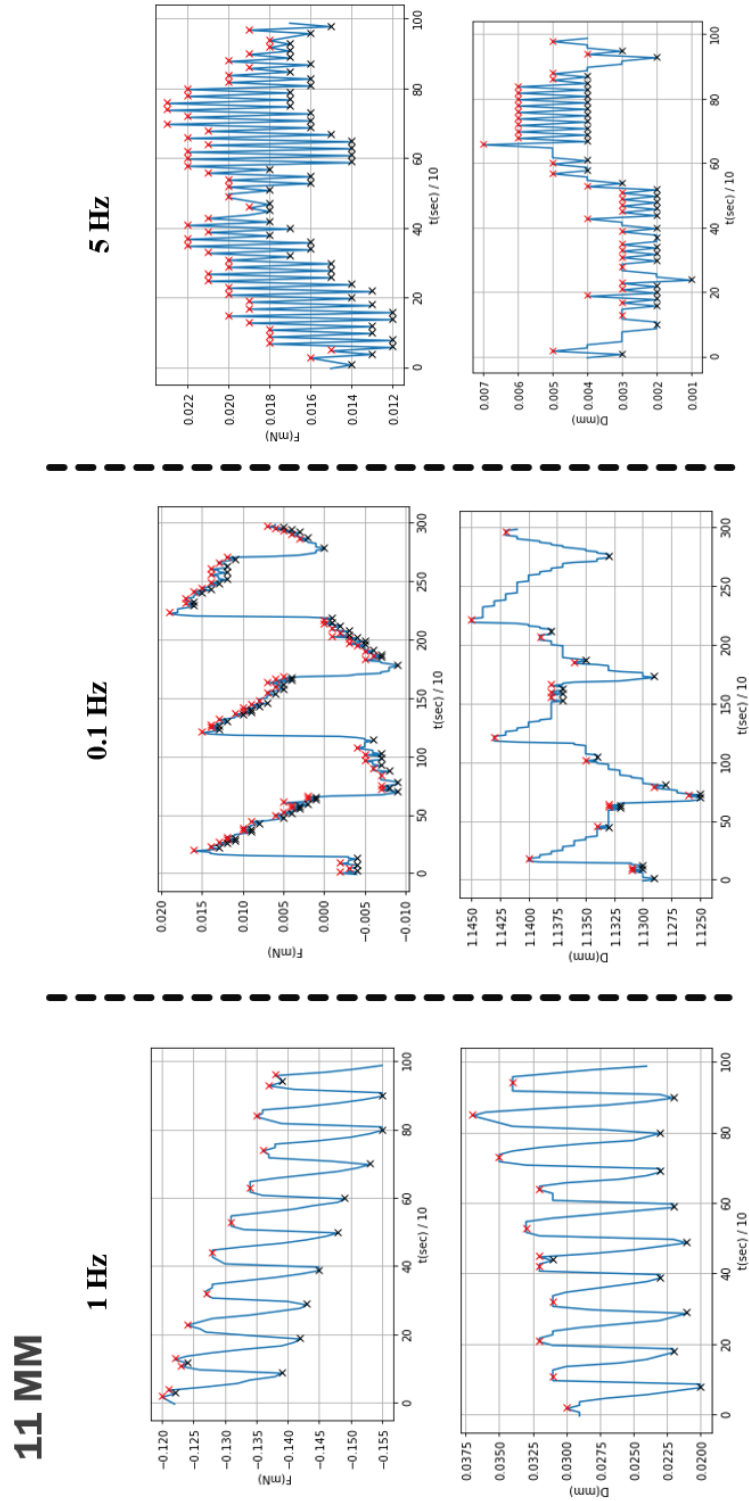


Figure 76: Tip force and displacement correlation, 11 mm IPMC. Top row: Force signal, Bottom row: Displacement signal.